TU Delft

DCpportunities

Design of a Gallium Nitride DC-DC MPPT Converter for Bipolar DC Microgrids

Master Thesis Report

Emilio Requejo Ruiz

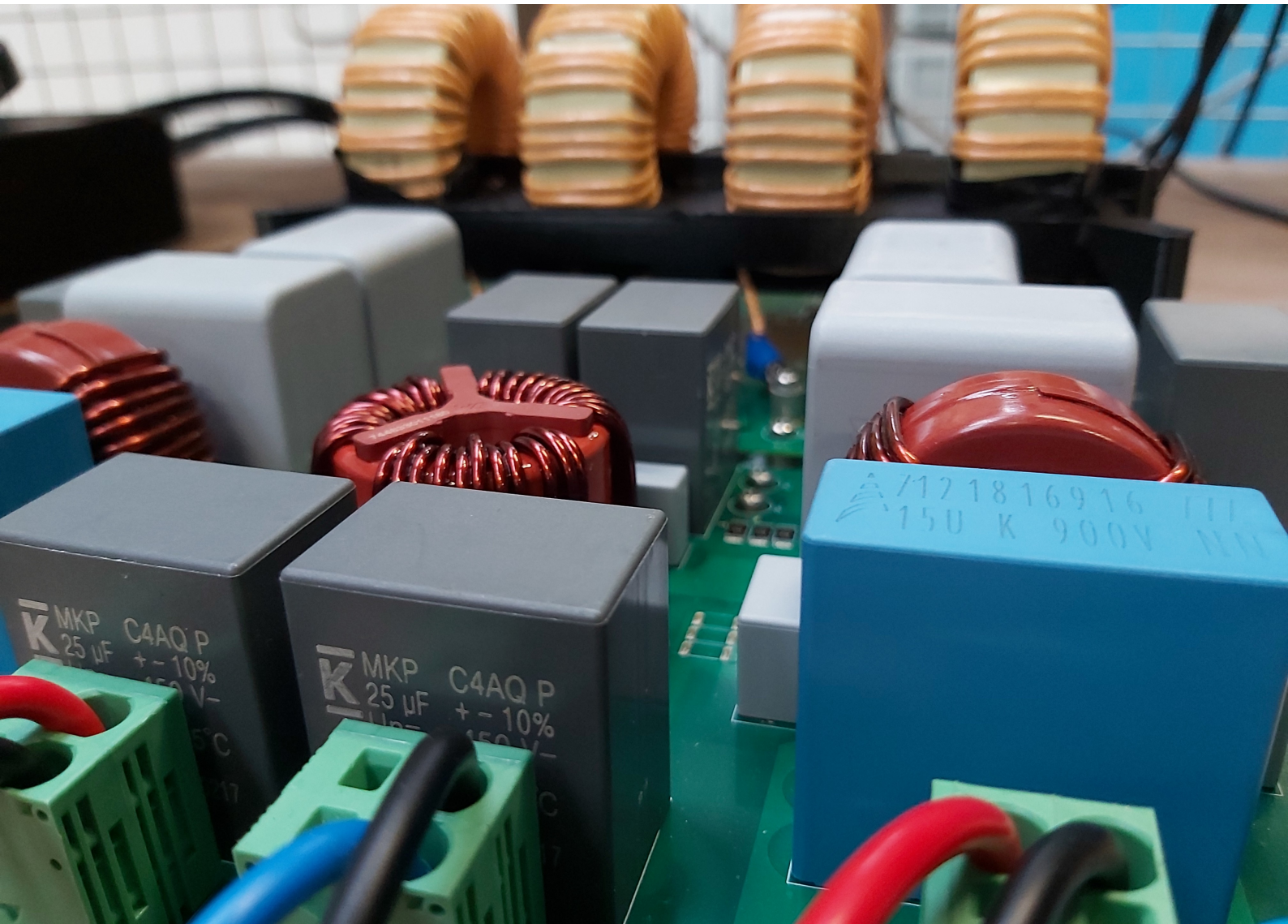

Design of a Gallium Nitride DC-DC MPPT Converter for Bipolar DC Microgrids

by

Emilio Requejo Ruiz

Student number: 5616255

A thesis presented for the degree of

Master of Science

Sustainable Energy Technology

at the Delft University of Technology,
faculty of Electrical Engineering, Mathematics & Computer Science,

to be defended publicly on the 25th of August, 2023 at 13:00.

Thesis committee:
Prof. Dr. Arno Smets, TU Delft
Dr. Patrizio Manganiello, TU Delft
Dr. Gautham Ram Chandra Mouli, TU Delft
Dr. Laurens Mackay, DC Opportunities R&D
Gerasimos Maroulis, DC Opportunities R&D

Acknowledgements

This thesis project marks the end of my time as a Master student at TU Delft. These exceptional past two years have been filled with many challenges that have pushed me to grow as a person in more ways that I could have imagined when I first set foot on Delft. However, I have not faced these challenges alone, and I dedicate my work to everyone that has supported me throughout this journey, both academically and personally.

First, I would like to extend my gratitude to Gerasimos Maroulis, not only for his guidance throughout the project, but also for being a true example of hard work and dedication. I also thank Dr. Laurens Mackay, for allowing me the opportunity to carry out this work at DC Opportunities, along with wonderful colleagues.

My thanks go as well to my supervisor at university, Dr. Patrizio Manganiello. I have always felt especially motivated to continue my work after our meetings, and I have his feedback and genuine interest in the project to thank for that. I would also like to thank Prof. Dr. Arno Smets and Dr. Gautham Ram Chandra Mouli for accepting to be part of my thesis committee, despite their busy schedules.

The constant encouragement from my family has been essential, and I am truly grateful to them for their support. Of course I also want to thank all the amazing friends that have stood by me, the ones in Delft, as well as those in Asturias. I thank them for being so close despite the distance that may separate us.

Lastly, no words can ever express how grateful I feel to Irina, my partner in every sense of the word. I thank her for her unwavering support, day after day, second by second.

Abstract

The use of DC microgrids in combination with photovoltaic (PV) energy generation sources results in higher efficiencies by avoiding AC to DC conversion. Moreover, bipolar DC grids allow for more system flexibility and increased reliability at the cost of an additional conductor when compared to unipolar DC. However, maximum power point tracking (MPPT) converters are still required in order to optimize the power delivered to the microgrid by PV systems. The development of more efficient and cost-effective DC-DC MPPT converters will be proven vital considering the expected growth in solar PV installation as a consequence of the relentlessly increasing global energy demand.

The objective of this thesis is to design a DC-DC MPPT converter for bipolar DC microgrids based on gallium nitride (GaN) high-electron-mobility transistors (HEMTs). GaN transistors are wide-bandgap semiconductor devices that can operate at very high switching frequencies due to their superior electron mobility compared to other semiconductor materials used in electronic switching. Increasing the operational frequency of an electronic converter allows for smaller passive components, which in turn has the potential to result in system size and cost reductions. A complete electrical and thermal analysis of the performance of these components is simulated and presented in this report, and the implications of employing these devices for the selected application are evaluated. The design overview of the DC-DC MPPT converter using these GaN HEMTs is also showcased in this work, as well as the results obtained from testing the assembled DC-DC MPPT converter for bipolar DC microgrids. The main conclusions of this work aim to clarify the advantages of GaN devices in MPPT applications, as well as demonstrate a design solution to the integration of MPPT converters to DC microgrids. The project was developed in collaboration with the company DC Opportunities, and the designed converter was assembled and tested in their laboratory.

Keywords: Photovoltaic, MPPT, DC Microgrid, Gallium Nitride, DC Converters.

Contents

List of Abbreviations

AC	Alternating Current
ADC	Analogue-to-Digital Converter
APS	Announced Pledges Scenario
CCM	Continuous Conduction Mode
CCUS	Carbon Capture Utilisation and Storage
CdTe	Cadmium Telluride
CIGS	Copper Indium Gallium Selenide
CO_2	Carbon Dioxide
DC	Direct Current
DCM	Discontinuous Conduction Mode
EMC	Electromagnetic Compatibility
EMI	Electromagnetic Interference
EV	Electric Vehicle
FET	Field-Effect Transistor
FOM	Figure of Merit
FR-4	Flame Retardant 4
GaN	Gallium Nitride
HEMT	High-Electron-Mobility Transistor
HV	High Voltage
IEA	International Energy Agency
LV	Low Voltage
LED	Light Emitting Diode
MOSFET	Metal-Oxide-Semiconductor Field-Effect Transistor
MPPT	Maximum Power Point Tracking
NZE	Net Zero Emissions
P&O	Perturb and Observe
PCB	Printed Circuit Board
PLECS	Piecewise Linear Electrical Circuit Simulation
PV	Photovoltaic
PWM	Pulse-Width Modulation
RC	Resistor-Capacitor
R&D	Research and Development
Si	Silicon
SiC	Silicon Carbide
SMD	Surface-Mount Device
STC	Standard Test Conditions
STEPS	Stated Policies Scenario
USART	Universal Synchronous-Asynchronous Receiver-Transmitter

List of Figures

List of Tables

Chapter 1

Introduction

This chapter illustrates the motivation behind the chosen research topic, followed by an enumeration of the objectives that are to be achieved throughout the work, as well as the research questions that will serve as a catalyst to reaching these goals. Lastly, a summarized outline of the thesis is provided.

1.1 Motivation

Electricity has become a precious commodity that is deeply rooted in our way of life. The fact that modern societies substantially rely on electricity for progress and development is unquestionable. Consequently, as economic development keeps growing, so too does global demand for more energy. Nonetheless, a substantial percentage of the energy generation sources installed on a global scale are based on non-renewable resources that contribute considerably towards climate change through CO_2 emissions. Multiple countries have already implemented policies and pledged to attain certain goals in order to tackle climate change and slow down the rise in global average temperature and its catastrophic consequences.

The IEA (International Energy Agency) has released a report compiling a global energy outlook of the year 2022 [1]. In it, the current energy consumption trends are described, and the forthcoming global energy context is forecast according to three different scenarios. First, the Stated Policies Scenario (STEPS), which takes into account only the already active policies and energy measurements that have been put in place. Secondly, the Announced Pledges Scenario (APS), which assumes that governments will meet their already announced climate-related commitments, and that they will do so on time. Lastly, the Net Zero Emissions (NZE) by 2050 Scenario, which presumes that the target of lowering global emissions to a net zero will be reached by 2050, and in doing so, the average global rise in temperature will be kept below 1.5 °C above pre-industrial levels. Figure 1.1 shows the global energy generation per fuel and total CO_2 emissions for 2021, with the expected values for 2030 and 2050, according to the three described scenarios. It is expected that, in the upcoming decades, renewable energy generation will increase considerably, even in the most conservative scenario. This, in combination with a reduction in reliance on polluting fuels, will cause a global decrease in CO_2 emission levels.

Renewable energy sources are therefore expected to exhibit a substantial upsurge of installed capacity. Out of these energy sources, solar PV stands out as one of the main drivers behind this change. Figure 1.2 displays global electricity generation in thousands of TWh, showcasing a breakdown of the total amount produced by source, for the years 2010, 2021 and the predicted amounts for 2030 and 2050 according to the three previously stated scenarios. In the STEPS, the most conservative scenario, it is expected that solar PV will be the largest contributing source to electricity generation by 2050, followed by wind. Thus, it can be said that the current policies implemented by various governments are enough to indicate that solar PV and wind energy are set to expand considerably in the coming decades.

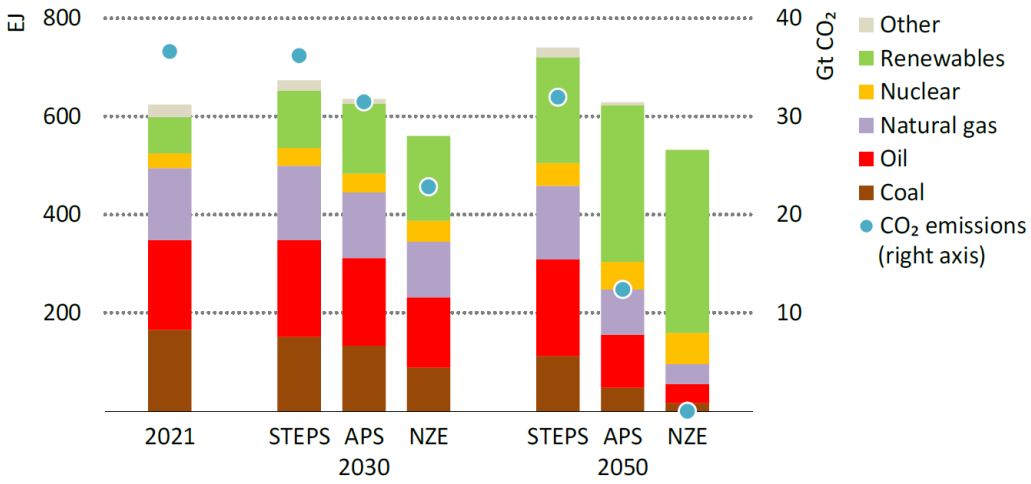

Figure 1.1: Global energy generation forecast per source and expected CO_2 emissions per year for the three described scenarios [1].

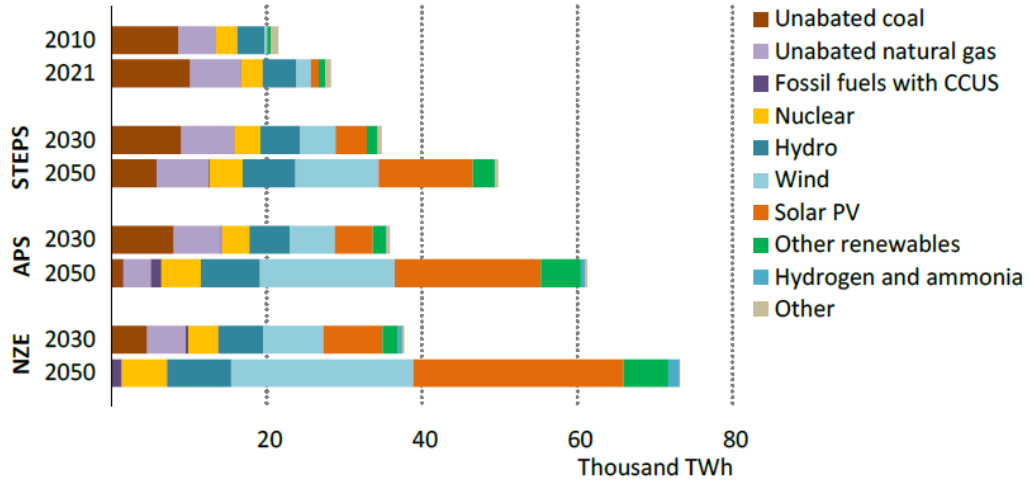

Figure 1.2: Global electricity generation forecast per source for the three described scenarios [1].

Solar PV will be a prevalent technology for renewable energy generation due to the fact that it is easily scalable. This means that photovoltaic technology can be used for small applications, and the same PV setup can be expanded for more power-demanding installations in a practical manner. Moreover, PV panels are easy to place in a variety of unobtrusive locations and positions. This makes PV systems largely adaptable to an extensive range of customers and applications. Additionally, another driving force behind PV growth lies in its long-term costs. The operational costs of photovoltaic energy are exceptionally low, even when compared to other renewable energy generation sources. Photovoltaic systems are able to keep operational costs at a minimum due to the fact that solar panels require meagre maintenance. For all these reasons, photovoltaic technologies are expected to grow at an increased pace when compared to other renewable energy sources.

On a higher level, photovoltaic technology serves as an energy generation resource for energy systems, whether they are isolated or connected to an external electricity grid. Microgrids are modern distributed energy systems reduced in scale. These are comprised of a localized and controllable group of disseminated energy sources and loads that can function independently or in conjunction with a centralized electricity grid. When incorporated into microgrids, PV systems supply local energy demand and any excess or deficit in energy is dealt with by the control of the microgrid. Therefore, the microgrid functions

as a single entity with respect to the electrical grid when interfacing with the larger-scale centralized grid.

PV systems can be integrated in microgrids whether they are based on AC or DC. Nonetheless, the maximum potential of PV systems can only be exploited through the use of DC-based microgrids, since the output of a PV system is by default in DC. Transforming this energy into AC for use within an AC-based microgrid implies the use of auxiliary power converters, which in turn results in additional power losses. However, these losses are avoidable through the use of DC-based microgrids. DC power grids interface naturally with PV, resulting in less energy conversion steps and, consequentially, in higher efficiencies. Furthermore, battery storage systems and electric vehicles commonly require DC energy too, further increasing the benefits of DC microgrids versus the conventional AC grid. The expected advancement and expansion of these technologies naturally signifies that DC microgrids will see considerable growth too.

Replacing already-existing AC microgrids in order to take advantage of the capabilities of DC microgrids is usually too costly to prove profitable. The upfront costs and cumbersome procedure necessary to replace the existing AC infrastructure typically outweighs the efficiency benefits. Despite this fact, the drawbacks of AC tip the scales in favor of DC when it comes to new constructions. Currently, new microgrid infrastructure is commonly installed in rural areas where there is otherwise no convenient access to electricity. These locations are generally situated substantially far from urban nuclei, and so the prohibitive costs of expanding the transmission lines from the centralized grid ensues that it is economically more viable to install isolated DC microgrids to cover electricity demand. Remote rural areas without access to electricity are proportionally more numerous in developing countries.

As a consequence, developing countries increase their electricity demand at a faster rate than the global average. It is expected that this amplification in energy consumption will accelerate from 2023, with China, India, and other countries in southeast Asia at the lead. These regions are anticipated to present the highest electricity demand annual growth rates in the world [2]. Figure 1.3 presents the change in electricity demand per year for various regions. The previously mentioned developing regions are expected to increase their demand considerably compared to other advanced economies. Moreover, it can be said with certainty that overall electricity consumption will continue to increase over the coming years for advanced and developing economies alike, albeit at different rates.

In light of all of this, it can be concluded that developing countries will contribute greatly to the installation of DC microgrids and PV systems. These technologies will therefore see unprecedented growth due to all of these factors. And so, the development of more efficient and cost-effective power electronics focused around these technologies will have a highly profitable impact. Research surrounding these topics will also contribute to outweighing the negative aspects of these technologies versus conventional polluting sources, such as the variability and unpredictable nature of solar PV generation.

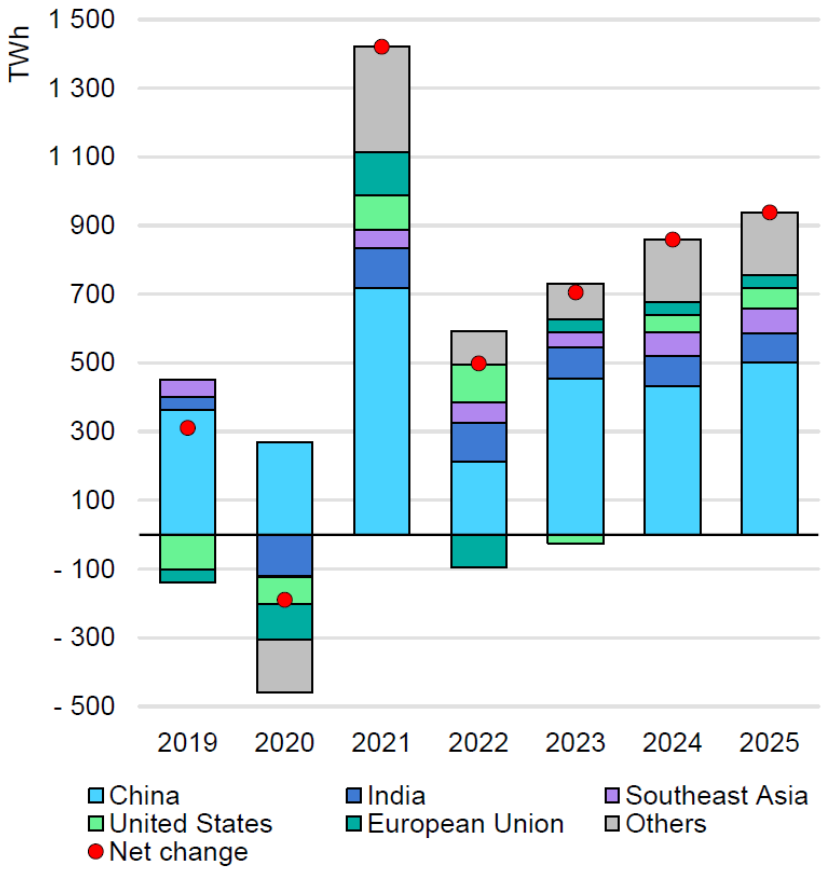

Figure 1.3: Change in electricity demand forecast for different key regions [2].

1.2 Objectives

Among the components needed to guarantee the optimal functioning of a PV system in connection to a grid, the MPPT converter stands out as one of the most critical. An MPPT converter serves as the interface between the PV system and the electrical grid. Its main task is to implement a control algorithm in order to maximize the power drawn from the PV panels, ensuring that the converter applies the necessary load in order to remain at the point of operation that provides the highest output power. When employing AC grids, the MPPT conversion process is followed by an inverter, whereas in DC grids, a DC-DC converter that incorporates the MPPT method is sufficient.

DC-DC MPPT converters still have the potential to improve in numerous ways. Three of the most relevant parameters that could be enhanced are efficiency, power density, and cost. First, an increase in efficiency ensures that as much power generated by the PV system as possible is transferred to the output grid. Secondly, increasing the power density of the converter enables reductions in size, which facilitates their installation in a wider spectrum of applications and reduces expenses related to available volume. Lastly, a reduction in converter cost would naturally make for a more affordable product.

The aim of this project is to design a DC-DC MPPT converter for bipolar DC microgrids, where PV is implemented as a main source of renewable energy, considering that the vast majority of MPPT converters found in industry are DC-AC inverters. With the aim of improving on the three aforementioned parameters of efficiency, size and cost, the switching operation of this MPPT converter will be based on gallium nitride HEMTs. These transistors can potentially operate at very high switching frequencies, which could allow for higher power densities and lower costs through the use of smaller passive components. Valuable insight can be gained through designing, building and testing an MPPT converter that distinguishes itself from conventional MPPT converters in these ways. Therefore, the main objective of the thesis is to ascertain how a DC-DC MPPT converter design can be made suitable to bipolar grids, evaluate how the use of GaN switches influence this design, and verify the operation and performance of the MPPT converter, as well as study how performance is affected by different conditions. These ambitions are achieved through the manufacturing of a DC-DC MPPT converter based on GaN-switching for bipolar DC grids.

1.3 Research Questions

In order to accomplish the objectives set for this thesis, a number of research questions have been formulated. These research questions serve as a guideline to successfully execute the project. By providing sensible answers to these questions, the goals of the thesis can be considered fulfilled. These are the following:

1. How can a DC-DC MPPT converter based on gallium nitride switching be designed in a way that is suitable for bipolar DC grids?

An MPPT inverter serves as a way to implement a PV energy generating source to an AC grid, but how can a PV system be integrated to a bipolar DC microgrid? The purpose of this question is to reach a specific design for the GaN-based MPPT converter that allows DC-DC connection of PV sources in bipolar grids, while allowing GaN switching for the benefits it provides. The proposed design must be validated through manufacturing and testing of the converter, in order to ensure that a valid conclusion is reached.

2. How do gallium nitride switches compare to other alternative solutions?

There are various other technologies that directly compete with GaN when it comes to power electronic switching. By answering this question, it is intended to reach a conclusion on the benefits and limitations that GaN switching presents relative to comparable alternatives. This analysis is to be carried out focusing on applications such as the designed MPPT converter, reflecting on the different aspects in which the use of GaN switching influences the final product design.

3. What are the factors that affect the operation of this converter, and how does the operation range impact efficiency?

The voltage and current provided by PV systems over a given time period is variable in nature, since the output of a PV module is weather-dependent. Additionally, other external factors could cause variations in converter performance. This research question seeks to provide insight as to what these parameters could be, while also revealing under which conditions can the efficiency of the proposed MPPT converter design be maximized.

1.4 Thesis Outline

The thesis report is divided into six chapters that describe the research done and work process carried out in order to achieve the project goals. The order, structure and brief summary of the topics presented per chapter is as follows:

Chapter 1: Introduction

The motivation behind this work is described, focusing on the importance of PV systems and DC microgrids, the desired objectives and research interest.

Chapter 2: Literature Review

An overview of the prior art regarding the research topic is provided, showcasing the current state of industrial PV, MPPT converters, GaN switching and DC microgrids based on scientific publications.

Chapter 3: Design and Analysis of the MPPT Converter

A theoretical analysis on the topology selected for the designed MPPT converter, specification values and performance based on simulations is presented. This is followed by an in-depth design overview of the various elements that comprise the converter. Afterwards, the control logic used is specified, and the chapter ends with considerations on a suitable PV system for this converter.

Chapter 4: Testing and Results Analysis

The manufactured MPPT converter based on GaN switching is tested under different conditions, and its correct operation across the specified operational range is validated through the results displayed and discussed in this chapter.

Chapter 5: Performance and System-Level Implications of GaN vs. SiC FETs

A comparison between using GaN switching as compared to SiC is shown. This comparison is based on a performance analysis, supported by simulations, and a system-level study. This is followed by a summary on the benefits of selecting GaN switching for the designed MPPT converter.

Chapter 6: Conclusion

The outcome of the project is discussed, taking into consideration the insight gained from the test results, the advantages of using GaN switching and the recommendations and future work for improvement in upcoming designs.

Chapter 2

Literature Review

This chapter presents the information compiled during the literature review process. It begins with an analysis of the existing industrial PV technologies. Consequently, a rundown on the MPPT power conversion process is presented. This is followed by an overview of gallium nitride as a semiconductor material for power electronic switching. Lastly, the advantages of DC microgrids as power distribution systems are evaluated, as well as the benefits of employing a bipolar DC configuration in contrast to the classic unipolar configuration.

2.1 Photovoltaic Technology in an Industrial Context

During the last decade, the global presence of photovoltaic energy has increased exponentially, presenting faster growth than any other power generating source. In 2021, more solar energy capacity was deployed globally than all other renewable technologies combined [3]. In Europe, it is foreseeable that the PV market will continue its growth tendencies with the European Union as a main agent behind this change. This is due to the fact that various countries are pushing for legislation towards reaching carbon neutrality by 2050 in compliance with the European Green Deal adopted in 2020. One of the main reasons behind this increase in PV installed capacity is the steep cost reduction that PV technology has experimented over the past years. Additionally, the capacity of PV to be scalable makes it a very flexible technology with a wide range of applications: from small isolated energy systems, to large-scale grid-connected PV systems.

The different available PV technologies can be classified according to their technical characteristics into three different generations. First-generation solar cells consist of wafer-based mono-crystalline and poly-crystalline silicon cells. The difference between these two technologies lies in the fact that mono-crystalline silicon cells are comprised of a single uniform silicon crystal structure, while poly-crystalline silicon solar cells are made up of multiple small silicon crystals bound together. Generally, mono-crystalline silicon presents higher efficiencies and longer lifetime compared to other PV cells, but their production costs are often high and energy-intensive. In comparison, poly-crystalline silicon is a cheaper and less efficient alternative. Second-generation PV cells are most commonly comprised of thin-film materials. These thin-films are made from very thin layers of semiconductors such as such as cadmium telluride (CdTe) or copper indium gallium selenide (CIGS). They have lower production costs than first-generation solar cells, but mass producing these modules tends to be unprofitable due to the low availability of the raw resources necessary to build them. These materials are also toxic, and so more precautions must be taken when it comes to disposing of them at the end of their lifetime. Additionally, these solar cells present slightly smaller efficiencies than first-generation cells [4]. Third-generation cells use emerging materials and technologies, such as organic crystals or quantum dots, with the aim to further reduce the costs of PV while increasing efficiency. Third-generation PV cells are currently in development and not commercially available.

PV modules, composed of multiple interconnected PV cells, need to be affordable and have high efficiencies, long lifespans and no supply constraints in order to develop and continue growing in the market. Currently, the most common PV modules are made of first-generation PV cells, as these modules are the ones that best comply with the previous requirements. Silicon wafer-based PV accounted for more than 95 per cent of the total 2021 production [5], [6]. Crystalline silicon modules have efficiencies ranging from 16 to 23.6 per cent. Due to the efficient and large-scale supply chain that exists for the silicon industry that is not present for other materials, first-generation PV cells tend to be the most favourable option for PV modules in the industry sector.

2.2 Solar MPPT Power Conversion

The growth in installation rate of photovoltaic systems is mainly hindered due to the direct reliance on sun radiation and other meteorological conditions inherent to PV systems. The unpredictable nature of the weather results in high variability of energy production across the day. The constant change in environmental conditions is one of the reasons why PV systems need an electronic converter for control that maintains the system at the point of optimal operation regardless on these external circumstances. These type of devices are called Maximum Power Point Tracking (MPPT) converters.

MPPT converters serve as the point of connection between a PV system and the grid or distribution system. These converters ensure that PV systems are always producing the most amount of power possible given the circumstances at any point in time, while also implementing fault detection mechanisms and other general control features. MPPT converters are most commonly seen as DC-DC converters that link a PV system to an inverter to be used for AC grids. The MPPT converter is then designed to minimize losses and maximize the output power fed to the inverter. Figure 2.1 illustrates the typical configuration of a PV system connected to an AC grid. A DC-DC boost converter performs MPPT algorithm, adjusting its duty cycle based on the current and voltage generated by the PV array. Afterwards, another power conversion step follows through the use of the inverter, that converts the power generated into AC that can be fed to the grid.

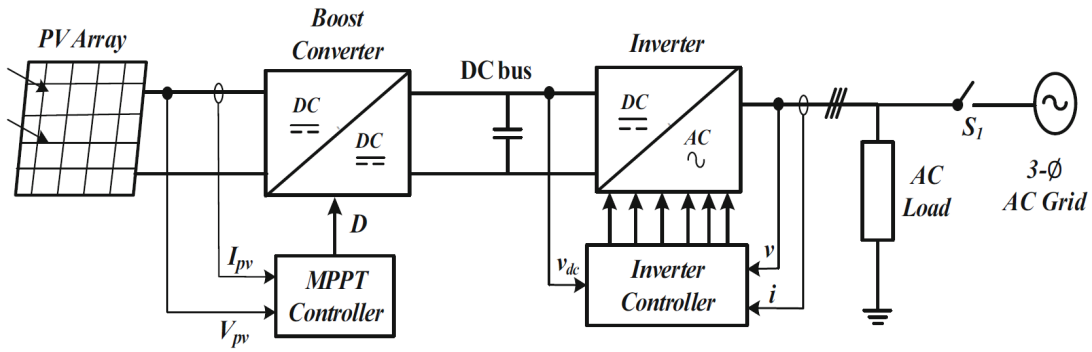

Figure 2.1: Electrical diagram of a standard PV system power process [7].

A boost circuit configuration is comprised of a transistor, a diode and an inductor that serves an energy storage component. Additionally, two capacitors are commonly added in order to filter the input and output signals, decreasing voltage ripple. Such a topology is shown in Figure 2.2, that presents the circuit diagram of DC-DC boost converter for MPPT applications. Typically, the main function of a boost converter is to regulate the output voltage generated based on the input voltage provided. This operation is governed by the transistor. The duty cycle of the transistor varies based on input voltage and output voltage. This process is possible due to the inductor, since current flows through it during the on-state, storing energy in the form of a magnetic field. This energy is released during the off-state, and so the inductor behaves as a voltage source in series with the input voltage. Through fast intermittent switching, the energy stored in the inductor coil will never be fully depleted, and so the voltage across the output will remain at a higher level than the one present at the input [8]. When functioning as an MPPT converter as in Figure 2.2, the output voltage is established by an external system component,

such as a DC grid, and the aim of the boost converter is then to adjust its duty cycle to maintain the voltage and current delivered by the PV array at the optimal power point.

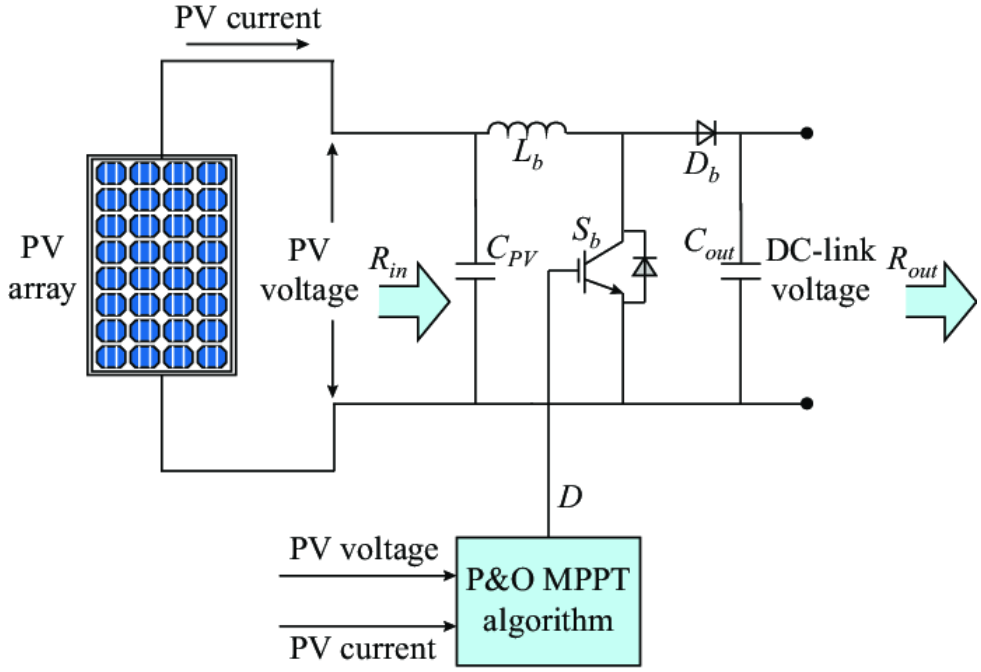

Figure 2.2: Circuit diagram of a DC-DC boost MPPT converter [9].

As previously stated, the voltage and current that is provided by a PV array continuously changes throughout the day as a function of sun radiation and other meteorological conditions, and so the operational conditions that result in the maximum power point also change. Directly transferring the power delivered by the PV array as a multiplication of the voltage and current naturally provided at any given time is inefficient and sub-optimal. Therefore, it is desirable to adjust the average inductor current value by changing the duty cycle, so that it results in the highest power flow output. Since the maximum power point of the PV array varies with time, so will the optimal duty cycle of the boost converter. Thus, an MPPT algorithm is used in order to regulate the duty cycle of the boost converter accordingly.

PV systems are composed of multiple strings of PV modules, each comprised of various series-connected PV modules. An MPPT converter can be connected to a PV system in three different common configurations. One converter can be used for an entire PV system with all strings connected in parallel in a centralized architecture, a converter can be connected to each PV string, or one converter per each individual PV module can be used. The benefit of using an MPPT converter for each of the PV modules is that the optimal maximum power point is reached for each module individually, as the control of each converter focuses on each module. However, this configuration is usually avoided due to the expensive cost of employing a single converter per module, save for small-scale applications where PV modules are likely to be subject to conditions that individually alter the power output of each PV module, such as partial shading or differences in orientation. On the other hand, using only one converter for the entire PV system is cheap but sacrifices MPPT control quality, since a generalized control is more susceptible to the impact of partial shading and string mismatch effects. The most common approach is to distribute MPPT converters at a string level, with each converter connected to a string of PV modules.

2.3 Gallium Nitride in the Semiconductor Industry

For decades, silicon has been the prevalent semiconductor material for power FETs, to be used for various power electronics applications. Over the recent years, silicon has approached its theoretical performance limits, in parameters such as switching speed and thermal performance [10], [11]. As a

result, research and development on new materials that can replace and surpass the power electronic devices based on silicon has intensified. Among these materials, gallium nitride (GaN) has arisen as a promising alternative to silicon. Historically, GaN has been used primarily in the production of LEDs and radio frequency components. However, in the recent years it has been spreading to power conversion applications due to the advantages of using GaN integrated circuits over conventional silicon-based devices. Currently, the vast majority of commercially available GaN FETs are lateral GaN HEMTs, a denomination used to convey the high electron mobility values inherent to GaN transistors. The low power losses presented by GaN-based FETs when employed in high power applications have stimulated the use of these semiconductor devices, specially in the automotive industry. At a smaller scale, the high power density of GaN devices also allow for size reduction in many consumer electronics.

The following Table 2.1 presents five relevant properties of the three semiconductor materials that are most commonly used in the manufacture of electronic switching devices. These materials are silicon (Si), silicon carbide (SiC) and gallium nitride (GaN).

Table 2.1: Relevant properties of the three most prevalent semiconductor materials for electronic switching [12], [13].

Characteristic	Units	Si	SiC	GaN
Bandgap	eV	1.12	3.23	3.39
Electron Mobility	cm^2/Vs	1350	900	1500
Peak Electron Velocity	$\times 10^7$ cm/s	1.0	2.0	2.5
Critical Electric Field	MV/cm	0.3	3.0	3.3
Thermal Conductivity	W/cm·K	1.5	3.4	1.3

GaN is a wide-bandgap semiconductor material. It has a bandgap of 3.39 eV, larger in comparison to that of silicon, which presents a bandgap of 1.12 eV [14]. The bandgap of a material determines the electric field that it can withstand. Therefore, GaN semiconductor devices are ideal for applications that require transistors with high breakdown voltages, due to presenting a higher critical electrical field than silicon transistors. Employing wide-bandgap semiconductors allows devices to work at increased voltages and temperatures, augmenting the power density that these transistors can sustain. Additionally, a high saturation or peak electron velocity allows for faster switching frequencies.

The electric properties of SiC are similar to those of GaN. However, there are numerous differences that make a each material more suitable for different applications. One of these differences can be found in the electron mobility of the semiconductors. GaN presents a higher electron mobility than SiC, which makes GaN better suited for high-frequency applications. The electric mobility of SiC is greatly limited by critical issues in hetero-junction formation [15]. On the other hand, SiC presents higher thermal conductivity, which makes this material more suitable for very high power operations, where high voltage operation and very fast heat dissipation can prove more important over higher switching frequencies and the advantages derived from it [16]. Converter size reduction due to smaller passive components and faster responses to sudden changes in load current can be highlighted among the various advantages to using higher frequencies of operation. The reduction of converter size and, therefore, power density increase when using GaN was empirically proven in [17], where two iterations of an EV charger design are built, using GaN HEMTs for one and SiC MOSFETs for the other. The conclusion of this publication is that the GaN-based EV charger has a higher power density and lower cost while maintaining a similar efficiency to the SiC-based design.

Figure 2.3 displays a comparison between these two wide-bandgap semiconductors according to different applications, where nominal power levels and operational voltages dictate whether GaN or SiC is more suitable.

It can be seen from Figure 2.3 that, as stated in the previous paragraph, GaN devices are dominant for a wide range of operational voltages and power. However, the superior thermal conductivity of SiC proves to be more advantageous at very high powers.

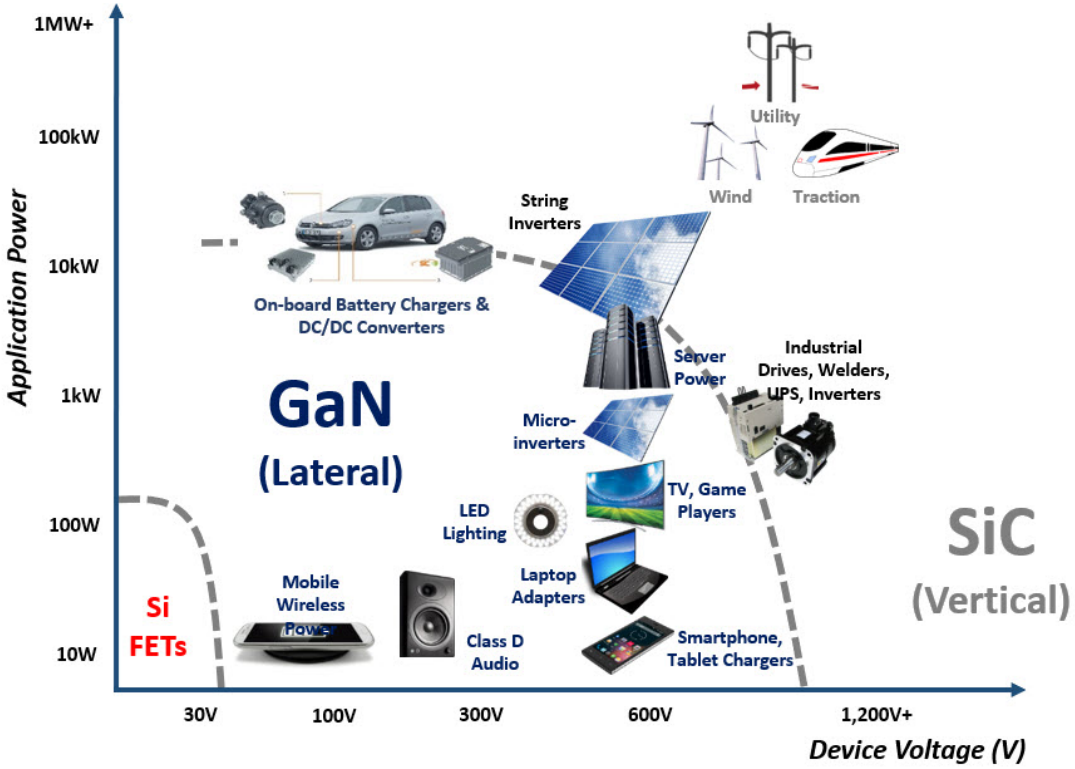

Figure 2.3: Wide-bandgap semiconductors comparison for different power switching applications as a function of operational voltage and power [18].

GaN devices also present shorter current paths compared to regular semiconductors devices, lowering the on-resistance of the devices for the same breakdown voltage rating. This further increases the efficiency of GaN-based power converters. Therefore, GaN transistors can be said to present a better figure-of-merit (FOM) when compared to their silicon and silicon carbide counterparts. Figure-of-merit is a mathematical expression commonly used to compare transistor performance. In its simplest and most widespread form, it is defined as the product of the on-resistance ($R_{DS_{on}}$) multiplied by the gate charge (Q_G) required to turn the FET on. As this figure is smaller in GaN in comparison with other semiconductor materials, it translates to lower conduction losses due to smaller on-resistances and faster switching speeds as well as enhanced performance in high frequency applications due to the smaller gate charge when using GaN transistors. Additionally, GaN FETs do not have a body diode built into the device, so there is no reverse recovery charge, further reducing the switching losses at high frequencies. The relationship between the specific on-resistance and the theoretical maximum breakdown voltage for the same three semiconductor materials considered in Table 2.1, (silicon, silicon carbide and gallium nitride), is shown in Figure 2.4. It can be seen that for a given specific on-resistance, GaN semiconductors present a higher theoretical breakdown voltage than the other two main semiconductor materials.

Based on the information provided in this section, it can be argued that GaN is superior to other comparable technologies in power switching applications that require high frequencies of operation or high breakdown voltages. For extremely high-power applications, the thermal conductivity of the semiconductor device takes priority over other aspects, like efficiency or operational frequency. Therefore, GaN devices reach their performance limits under such conditions, in which thermal dissipation is critical.

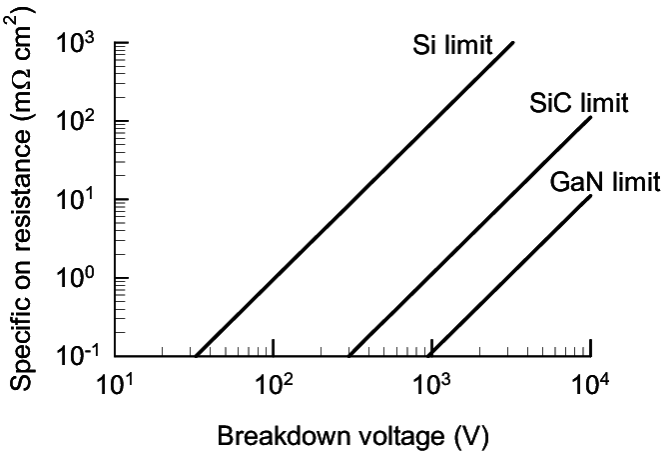

Figure 2.4: Specific on-resistance versus theoretical breakdown voltage for three semiconductor materials [19].

2.4 DC Microgrids

The use of distributed generation as an alternative to centralized power plants results in numerous environmental and economic benefits. Employing local energy sources leads to a reduction of line losses, minimizing energy wasted during transmission. Grid resilience is also improved with decentralized generation systems. However, the integration of distributed generation into the main electric grid presents challenges that must be overcome when it comes to control and flexibility. A solution to these issues is found in the use of microgrids. Microgrids are independent energy systems that incorporate distributed energy resources in a local area and are able to function in connection with an energy grid (grid-connected mode) or independently from it (islanded mode). These microgrids control and manage the various resources within their network, employing the generation sources available within in order to supply loads based on demand constraints, and applying selective curtailment when necessary. Microgrids can base their transmission in buses of AC, DC or a hybrid of both by using two separate buses. Figure 2.5 shows a typical system arrangement for DC microgrids. DC grids are becoming more relevant as more sources and loads connected to the low voltage grid use DC.

2.4.1 Advantages and Challenges of DC Microgrids

AC grids are more commonly widespread, due to the merits that AC transmission historically had over DC. The main benefit of AC grids over the years has been that it is possible to change the voltage level of the grid by using an AC transformer, while DC grids lacked the means to do the same efficiently. However, with the development of efficient DC-DC converters, the main advantage that AC distribution had in the past is no longer a limitation for DC.

Since many common electrical loads in households and other buildings require DC energy, making use of an AC grid requires the use of power converters to feed the prevalent DC loads. In addition to these loads, energy storage systems and various renewable energy sources, such as PV and fuel cells, operate in DC inherently and can naturally interface with a DC grid. In AC distribution systems, this leads to lower efficiencies due to conversion losses. Efficiency increases with DC distribution since the integration of PV and energy storage systems is simplified with less power conversion steps. The transmission efficiency of the lines in a DC microgrid is also higher when compared to AC due to the absence of reactive power in a DC line. Additionally, controlling an AC microgrid is comparatively complex due to various troublesome factors, such as harmonics and frequency control, that are not present in DC microgrids. With DC microgrids, only the voltage supplied to the loads needs to be regulated, and power outputs do not need to be synchronized [21], [22].

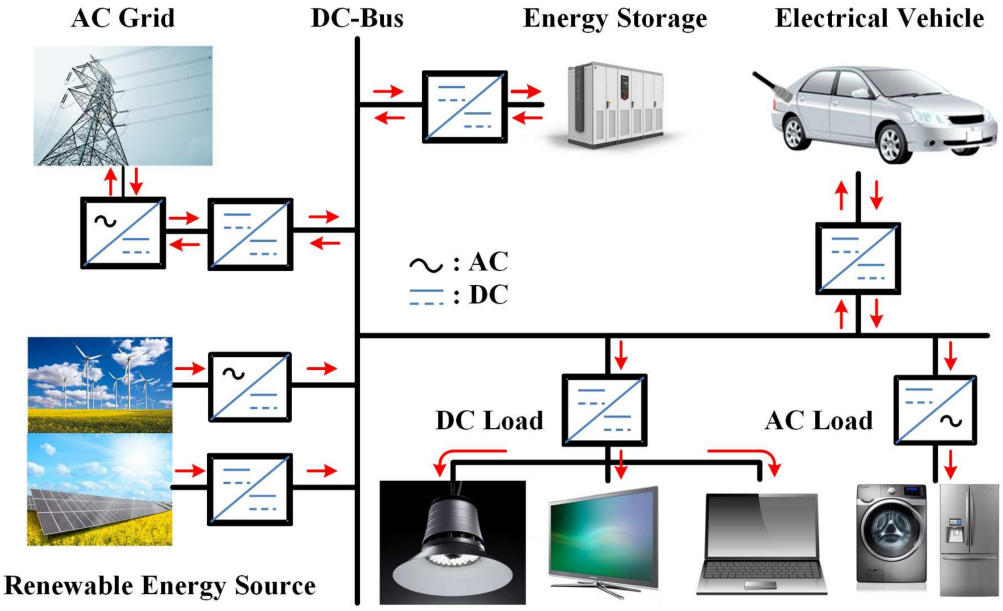

Figure 2.5: Standard system layout for a DC microgrid [20].

The main challenge for the development of DC microgrids is that most distributions systems currently existing are AC due to the advantages this configuration had over DC in the past. Additionally, the transition from AC to DC systems is very costly on a large scale. The installation of new DC microgrids is therefore hindered by the lack of DC electric appliances, since manufacturers are encouraged to design their products for AC compatibility in order to easily connect them to the predominant AC grids. However, the foreseeable further increase of installed capacity of PV technology and the development of electric vehicles will increase demand for DC microgrids [23].

2.4.2 The Bipolar DC Microgrid

Electric power in a DC system can be transferred using two wires (unipolar) or a three wire configuration (bipolar) [24]. A DC bus in a unipolar configuration has only one voltage level. Loads, sources and other devices are connected to the bus via a wire on the positive pole and another wire on the negative pole. The unipolar configuration is simple, but it requires more DC-DC power converters in order to connect loads to the bus at different voltage levels. On the other hand, a bipolar DC configuration counts with various advantages over unipolar systems. A bipolar DC system incorporates a neutral conductor in addition to the positive and negative conductor found in unipolar configurations. Therefore, there are three different voltage levels available in bipolar systems depending on the poles to which a load is connected: $+V_{dc}$, $-V_{dc}$ and $2V_{dc}$. Figure 2.6 shows an example of how voltage values can be arranged in a standard bipolar DC grid.

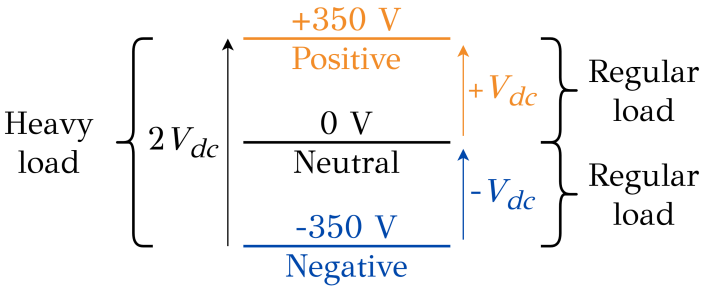

Figure 2.6: Example of voltage levels and possible load connections in a bipolar DC grid.

Having various voltage levels allows for more power-demanding loads to be connected at the highest voltage level while regular loads are connected between the positive-to-neutral pole or the negative-to-neutral pole. Hence, bipolar DC configurations offer double power capacity while only adding one conductor [25]. Making use of a bipolar DC grid also increases reliability, since in the case of a fault in one of the conductors the other two can still supply power.

The main drawback of a bipolar grid versus a unipolar one is that a voltage control system is necessary in order to keep both poles at the same balanced voltage. This voltage unbalance can be provoked due to the connection of uneven loads in different poles. Simultaneously, this unbalance reduces power quality and increases the strain on semiconductor devices.

Chapter 3

Design and Analysis of the MPPT Converter

This chapter showcases the analysis and design process of the manufactured MPPT converter based on GaN switches for bipolar DC grids. First, the converter is evaluated from a theoretical point of view and the selected topology is described. Then, the converter specifications are listed and and the results obtained from electrical, thermal and efficiency-focused simulations are discussed. Following this, an in-depth overview on the design, layout and selected components is delineated for the various elements that comprise the MPPT converter. Afterwards, the control logic employed is indicated. Lastly, various aspects regarding suitable PV system configurations for the particular application are evaluated.

3.1 Theoretical Analysis

The chosen topology for the designed DC-DC bipolar MPPT converter is a dual-input variation on the MPPT boost converter. The overall layout of the MPPT converter can be seen in Figure 3.1. Two different PV arrays, PV_1 and PV_2, deliver the input power for the converter, with a voltage equal to V_{in1} and V_{in2}, respectively.

As shown in Figure 3.1, the circuit can be interpreted as the combination of two interconnected boost converters, each delivering the converted power to a unipolar DC output. By connecting the negative line of the top circuit and the positive line of the bottom one, and referencing this connection to ground, the two originally independent circuits coalesce into a dual-input converter that is compatible with a DC bipolar microgrid. Therefore, the unipolar output of the top circuit assumes the form of the positive output pole of the bipolar DC grid, with a voltage equal to V_{out+}. Likewise, the output of the bottom circuit is remodeled into the negative pole of the bipolar grid, V_{out-}.

A pair of GaN FETs (Q_1, Q_2), or more specifically GaN HEMTs, are placed in the top and bottom side of the circuit. These transistors control the MPPT operation independently for the corresponding sub-circuit. The switches carry out this operation in accordance to their duty cycle (d_1, d_2) over a full time cycle. These HEMTs, in combination with two diodes (D_1, D_2) and two inductors (L_1, L_2), are placed in a boost converter configuration, analogous to the one described in section 2.2, that steps up the voltage received at the PV input to deliver power to the bipolar DC grid. A pair of capacitors per sub-circuit are used to filter the inputs (C_{in1}, C_{in2}) and outputs (C_{out1}, C_{out2}), decreasing voltage ripple and noise.

In order to simplify the analysis of this converter, only one of the boost converters that comprise it will be analyzed: the top sub-circuit. All equations and conclusions derived for one sub-circuit are applicable to the other. Moreover, all components will be considered ideal. Subsequently, the circuit will be analyzed for CCM operation, when the current flowing through the inductors remains continuous and does not reach zero during on or off time.

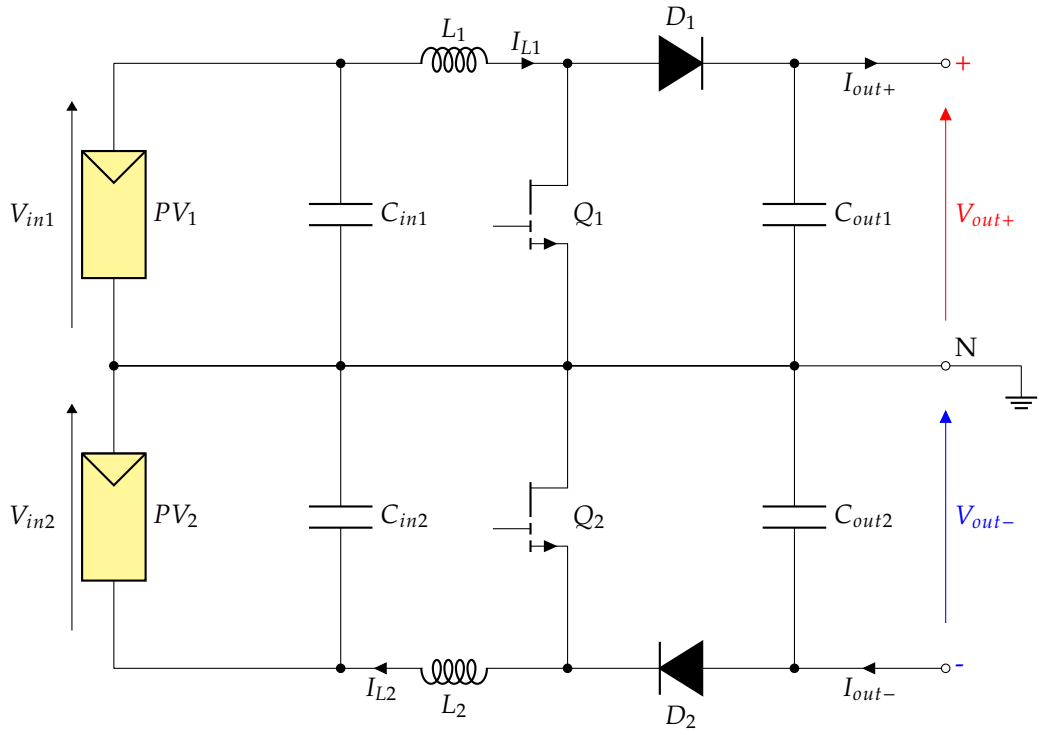

Figure 3.1: Circuit topology of the designed MPPT converter.

The behaviour of the boost converter over a time period T_1 can be divided in two phases depending on the state of the HEMT. On the one hand, there is the on-state, which lasts for $d_1 \cdot T_1$ seconds, and is the time where the transistor is activated, hence conducting current. On the other hand, off-state is the fraction of time where the HEMT is deactivated and behaves as an open circuit. This operation has a time span of $(1 - d_1) \cdot T_1$, and so the sum of the duration of both phases completes a cycle of T_1 seconds, under a switching frequency of $f_1 = \frac{1}{T_1}$.

During on-operation of the GaN HEMT, the voltage across the input, V_{in1}, is applied to the inductor L_1. This causes a variation of current flow through the inductor, I_{L1}. This variation is the current ripple during on-state, $\Delta I_{L1_{on}}$. Equation 3.1 denotes this value by considering the definition of inductance as the ratio between induced voltage and rate of current change. As a result of this on-state operation, the inductor stores energy in its magnetic field through the current provided by the PV input.

$$\Delta I_{L1_{on}} = \frac{1}{L_1} \cdot \int_0^{d_1 \cdot T_1} V_{in1} \cdot dt = \frac{V_{in1} \cdot d_1 \cdot T_1}{L_1} \tag{3.1}$$

During off-state, current flows through the diode towards the load connected to the output of the converter, and the energy stored in the inductor is released. Therefore, the inductor behaves as a voltage source in series with the PV input, leading to a stepped-up output voltage. The voltage across the inductor is therefore equal to the difference between the input and output voltage $(V_{in1} - V_{out+})$. The inductor current ripple during off-state, $\Delta I_{L1_{off}}$, can be calculated through an expression analogous to the one shown for the on-operation. This expression is showcased through Equation 3.2.

$$\Delta I_{L1_{off}} = \frac{1}{L_1} \cdot \int_{d_1 \cdot T_1}^{T_1} (V_{in1} - V_{out+}) \cdot dt = \frac{(V_{in1} - V_{out+}) \cdot (1 - d_1) \cdot T_1}{L_1} \tag{3.2}$$

Under steady state conditions, the sum of the variation in current in both states must be zero in order to

comply with the volt-second balance principle, given that the energy stored in the inductor must be equal to the energy released after a complete cycle. Thus, the net change in inductor current must be zero. Taking this into account, the previous equations can be combined in the way depicted by Equation 3.3.

$$\Delta I_{L1_{on}} + \Delta I_{L1_{off}} = \frac{V_{in1} \cdot d_1 \cdot T_1}{L_1} + \frac{(V_{in1} - V_{out+}) \cdot (1 - d_1) \cdot T_1}{L_1} = 0 \tag{3.3}$$

Rearranging Equation 3.3, it is possible to obtain an expression that defines the duty cycle of the HEMT as a function of input and output voltage, as shown in Equation 3.4. Taking into account the symmetry between the top and bottom parts of the converter, an equivalent expression can be derived for the second sub-circuit, presented as Equation 3.5.

$$d_1 = 1 - \frac{V_{in1}}{V_{out+}} \tag{3.4}$$

$$d_2 = 1 - \frac{V_{in2}}{V_{out-}} \tag{3.5}$$

Additionally, the average current through the output capacitance in steady state must be zero in order to maintain the capacitor charge balance principle. This concept states that the net charge stored in the capacitor must equal the charge released throughout a full cycle. Therefore, the average output current I_{out+} is equal to the current that flows through the diode D_1. During turn-on of the HEMT, no current flows through this diode. However, during off-state, the current that flows through the diode is the same as the average inductor current, which in turn is equal to the average input current, since all of these components are connected in series at turn-off. Thus, the average output current is equal to the average inductor current during turn-off operation, which yields the following Equation 3.6. The same logic applies to the bottom circuit, hence Equation 3.7 is obtained.

$$I_{out+} = I_{L1} \cdot (1 - d_1) \tag{3.6}$$

$$I_{out-} = I_{L2} \cdot (1 - d_2) \tag{3.7}$$

3.1.1 Interleaved Configuration

One of the shortcomings of electronic power conversion for high-power applications is that power loss has to be carefully managed so as not to overheat any of the components present in the system, especially the power semiconductor devices. For that reason, paralleling identical components that are susceptible to overheating is common practice in the industry, so as to split the current that flows through these devices. This leads to reduced conduction losses, since conduction loss has a quadratic dependence on current. This practice also allows for the use of components that are rated for lower currents.

Nevertheless, for some converter topologies a variation of this concept know as interleaving proves more beneficial. An interleaved circuit is defined as the composition of multiple identical power electronic phases operating in parallel. Applying interleaving to a circuit effectively yields the same benefits as standard device paralleling, but with extra value. For the selected converter topology, interleaving has the added advantage of reducing the output voltage ripple, since the ripple is divided among both phases of the circuit. This also leads to size reductions of the output capacitors, given that less capacitance is now required to filter the same voltage ripple. These ripple-related benefits are achieved by offsetting the switching operation between each of the interleaved phases by a $\frac{360^\circ}{n_i}$ phase shift, where n_i is equal to the number of interleaved phases. Figure 3.2 displays a two-phased interleaved configuration for the designed MPPT converter, where a second interleaved phase is added to both independent sides of the

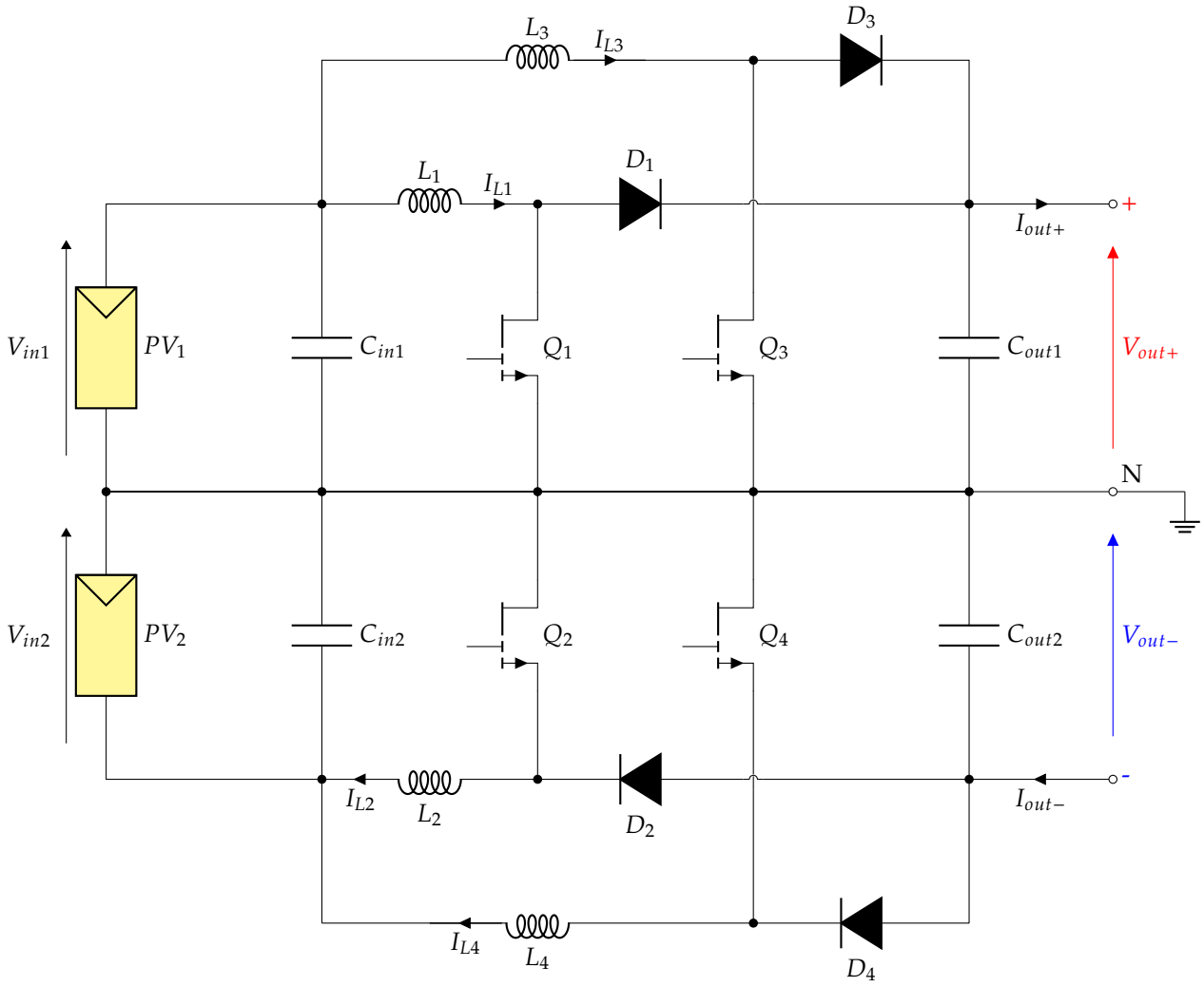

Figure 3.2: Interleaved configuration of the selected MPPT converter topology.

circuit. Thus, the second phases present a phase shift of 180° in their transistor switching signals with respect to the original phase.

As illustrated by Figure 3.2, each side of the circuit previously presented in Figure 3.1 now contains two identically connected power electronic phases. As previously explained, the two parallel phases in each side will have the same duty cycle with a phase shift of 180° (i.e. Q_1 and Q_3 both have a duty cycle of d_1). All mathematical expressions shown in section 3.1 are still applicable to the interleaved configuration, with the exception of Equation 3.6 and Equation 3.7. Since the inductor current is now equal to half of its original value, the interleaved expressions for the average output currents are Equation 3.8 and Equation 3.9.

$$I_{out+} = (I_{L1} + I_{L3}) \cdot (1 - d_1) \tag{3.8}$$

$$I_{out-} = (I_{L2} + I_{L4}) \cdot (1 - d_2) \tag{3.9}$$

3.2 Specifications

The designed MPPT converter for bipolar DC grids was developed with a specific application in mind. This project was carried out in collaboration with DC Opportunities R&D. The company aims to use GaN-based DC-DC MPPT converters for an electric vehicle (EV) parking lot application that integrates a PV system within a bipolar DC microgrid, in order to feed the EV charging stations and other loads. Thus, a system such as this can benefit from the advantages of using DC microgrids and function independently from an external grid due to the addition of PV as a generating source. The power rating at which the converter is designed to operate has been adjusted to be suitable for an application such as the one described. Considering this, the definitive MPPT converter specifications are presented in Table 3.1.

Table 3.1: MPPT converter specifications.

Parameter (per input/pole)	Value
Maximum output power	3.8 kW
Input voltage range	100 V to 380 V
Maximum input current	10 A
Nominal output voltage	±350 V
Output voltage range	±320 V to ±380 V
Duty cycle range	0 to 73.7%
Switching frequency	125 kHz

A typical nominal value for the voltage per pole of a bipolar DC grid is 350 V. Therefore, the converter is designed to operate with output voltages of 350 V per pole, for a total of 700 V from the positive to negative line. There is a certain acceptable deviation of grid voltage per pole, which can range from 320 V as a minimum to 380 V as a maximum, in order to accommodate load fluctuations. This is of special relevance when setting the allowable input range of the MPPT converter, since output and input voltages are closely related as earlier proven through Equation 3.4 and Equation 3.5.

The input voltage range of the designed MPPT converter is set to be from 100 V to 380 V. The maximum value of 380 V at the input is set based on the maximum voltage at the output of a pole, since when 380 V are present at an input, the same 380 V can be delivered at its corresponding output by keeping the GaN FETs at a duty cycle of 0% (completely off). The minimum input voltage of 100 V was decided after performing thermal simulations. Low input voltages lead to high duty cycles, which when combined with high currents can lead to overheating of the GaN HEMTs. Therefore, the minimum voltage is set to 100 V, so as to prevent the converter from operating under unsafe conditions. This is explored in detail in subsection 3.3.2. In addition, the wide operational voltage range specified allows for the MPPT converter to function under partial shading conditions, given that input voltage will decrease when the PV array is partially shaded even if a large current is still being generated due to high irradiance over the rest of the array. The duty cycle of the GaN switches ranges from 0 to 73.7%. These values are a direct result of employing Equation 3.4 and Equation 3.5, where a a maximum input voltage leads to a duty cycle of 0% and a minimum input voltage at maximum output voltage leads to an optimal duty cycle equal to 73.7%.

The maximum input current of 10 A per input is set at a high value that allows for the desired output power levels, while being low enough so that the thermal performance of the converter remains within safe limits at all duty cycles. Given these parameters, the maximum output power that can be delivered by the converter is 3.8 kW per pole, for a total of 7.6 kW when considering both poles.

Lastly, the switching frequency is set in accordance to the inductor current ripple values and switching losses calculated from simulations during the early stages of the design. This is further elaborated upon in section 3.3. As a concise explanation, this switching frequency is set as high as possible so as to allow for smaller passive components and lower converter cost, but it is limited by the fact that switching losses and inductor core losses increase at higher frequencies of operation, hence frequency can not be exceedingly high. Thanks to the use of GaN and the low switching losses that they present when

compared to other alternatives in the industry, the selected frequency of operation is set at a higher value than it would be feasible with other transistor technologies in this application.

3.3 Simulations and Performance Analysis

The main goal behind performing simulations is to gain more insight on how this converter topology behaves from both an electrical and thermal point of view. The performance of the designed converter can be evaluated through the use of simulations, and important specification parameters such as input and output voltage, current, duty cycle and overall efficiency can be verified. The simulations were carried out using PLECS, a modelling and simulation software for power electronic systems developed by Plexim. The circuits presented in both Figure 3.1 and Figure 3.2 were replicated in PLECS. The following Figure 3.3 displays the interleaved circuit configuration recreated in PLECS.

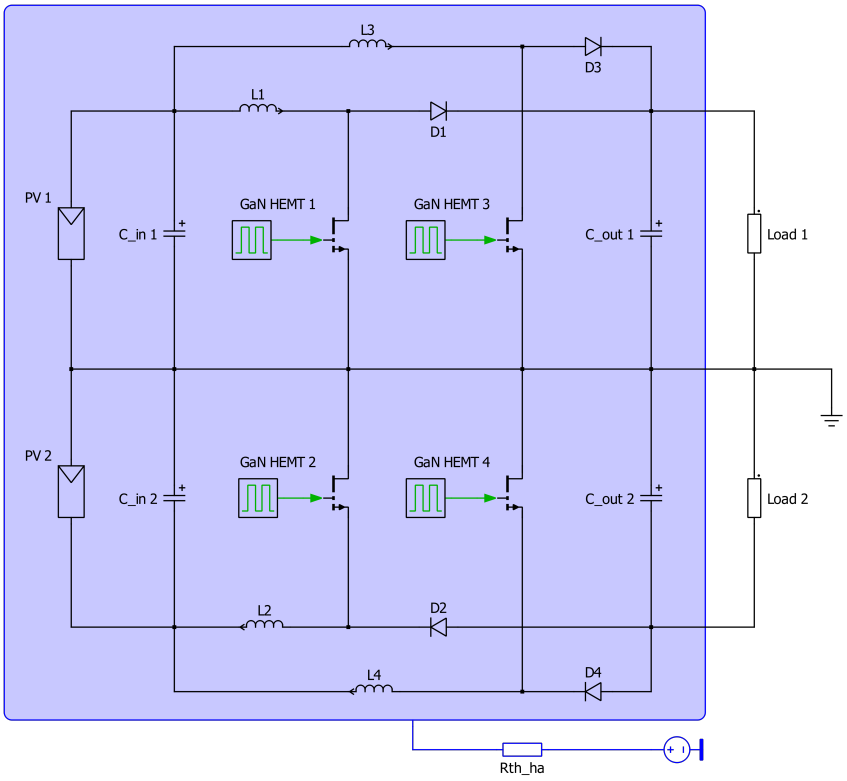

Figure 3.3: PLECS model based on the MPPT interleaved configuration.

These simulations proved to be fundamental when it comes to decision making during the component selection process, especially for the semiconductor components. Employing simulations simplifies this selection process by providing accurate calculations of current and voltage levels across various points in the system under multiple operating conditions. According to the observed currents and voltages throughout the range of operation, the components can be sized for rated currents and voltages that are above the measured operating values. Additionally, PLECS can calculate temperature rises originating from conduction and switching losses from the power electronics used in the circuit. Based on this, it can be seen whether a certain component is more efficient than others, and whether multiple power semiconductors should be paralleled in order to keep the individual temperature rise within acceptable levels.

An accurate thermal model of the selected GaN HEMTs was acquired from the GaN Systems website [26]. When modelling the thermal description of other GaN switches in the market not developed by GaN Systems, a thermal model was created based on the conduction and switching loss graphs provided in the datasheet of the given device. This same procedure was also followed in order to model the thermal behaviour of several diodes.

3.3.1 Electrical Simulations

As previously stated, the electrical simulations carried out are essential for the selection process of components and other parameters. The overall procedure was an iterative one, where the simulation was developed as the design of the MPPT converter progressed, including more improvements and changes with time.

In order to depict the conversion operation of the designed MPPT converter, Figure 3.4 and Figure 3.5 display the voltage and current across a representative GaN FET and inductor pair in the interleaved MPPT circuit setup for a duration of two time periods in steady-state. For this simulation the input voltage and current delivered by the PV arrays are 320 V and 10 A, respectively. The load of the circuit is adjusted so that the grid output voltage across both poles is close to its nominal 350 V, resulting in a positive-to-negative total output voltage of 700 V. These parameters represent the highest power conditions that the converter will operate in for a nominal grid voltage.

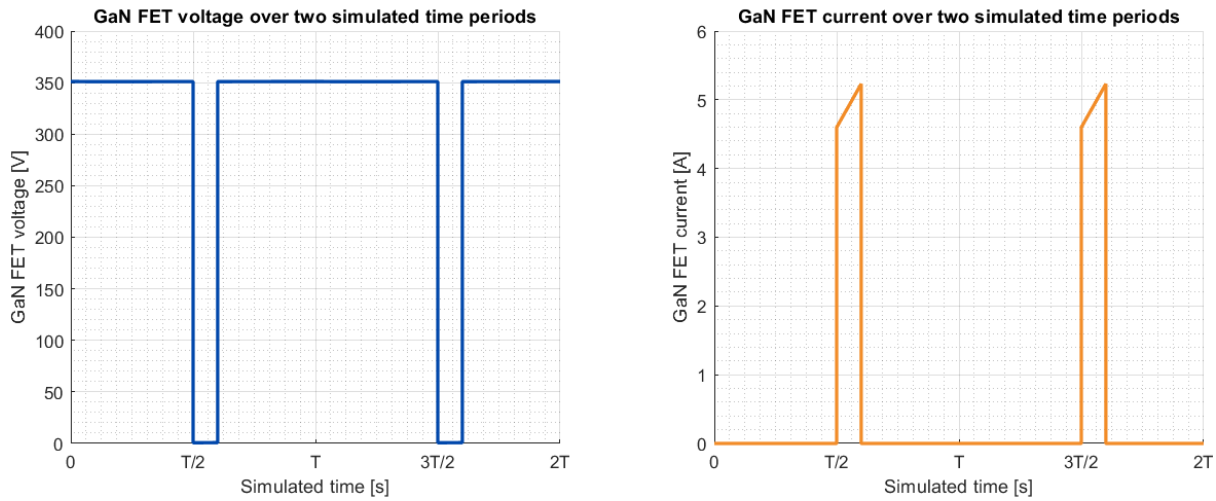

Figure 3.4: Voltage (left) and current (right) across a GaN FET over two simulated time periods in an interleaved configuration.

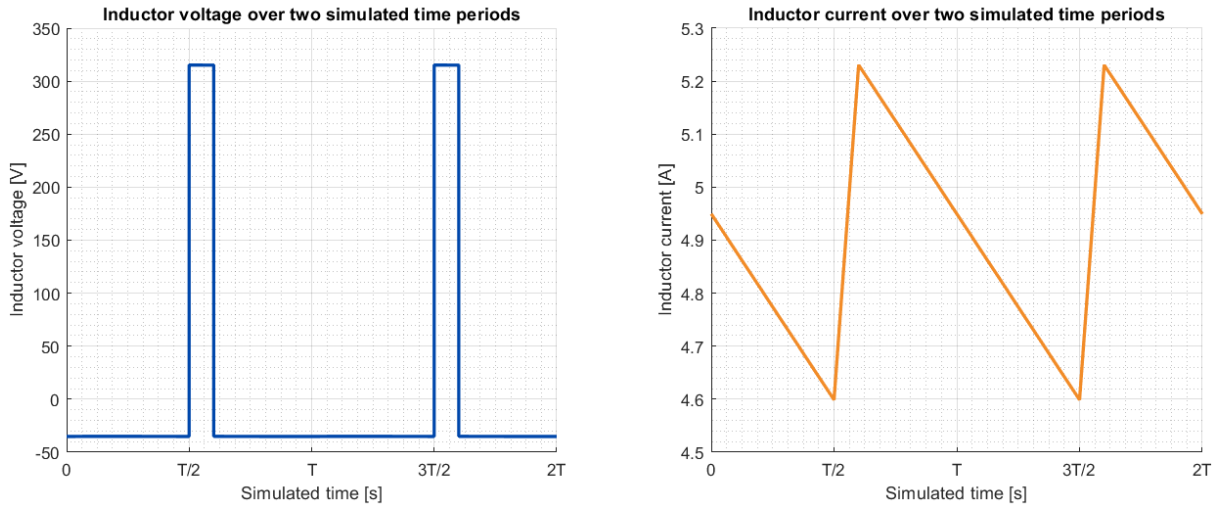

Figure 3.5: Voltage (left) and current (right) across an inductor over two simulated time periods in an interleaved configuration.

It can be seen from Figure 3.4 and Figure 3.5 that while a GaN FET is on, (and hence, it is conducting current), a positive voltage variation is presented across the inductor, which causes a rise in current

in accordance to the expressions displayed in section 3.1. The inductor current waveform is of particular interest during simulations, since multiple parameters influence its shape, and the current ripple presented by each inductor will impact the core losses that it produces.

The expected core losses of the inductors were calculated through an external tool developed by the manufacturer of the inductor cores that DC Opportunities typically uses in converter design. Hence, the inductance value of each inductor and the frequency of operation of the converter were selected with the aim of balancing the overall losses of the converter while keeping a high enough frequency to allow for smaller passive components. A more in depth analysis of the losses and efficiency overview is given in subsection 3.3.3. Ultimately, the inductance value chosen for each inductor is 400 µH, which results in an equilibrium between the aforementioned criteria. As shown in Figure 3.5, the inductor current ripple under the final simulated parameters is kept under 15%.

It must be noted that the voltage ripple across the output capacitors is negatively affected by increases in frequency. However, as presented in subsection 3.1.1, the reduction of this ripple value is one of the benefits of employing interleaved phases in converter design. As corroboration of this effect, Figure 3.6 displays the simulated output voltage signal generated at one of the poles of the system for both a standard and interleaved converter setup.

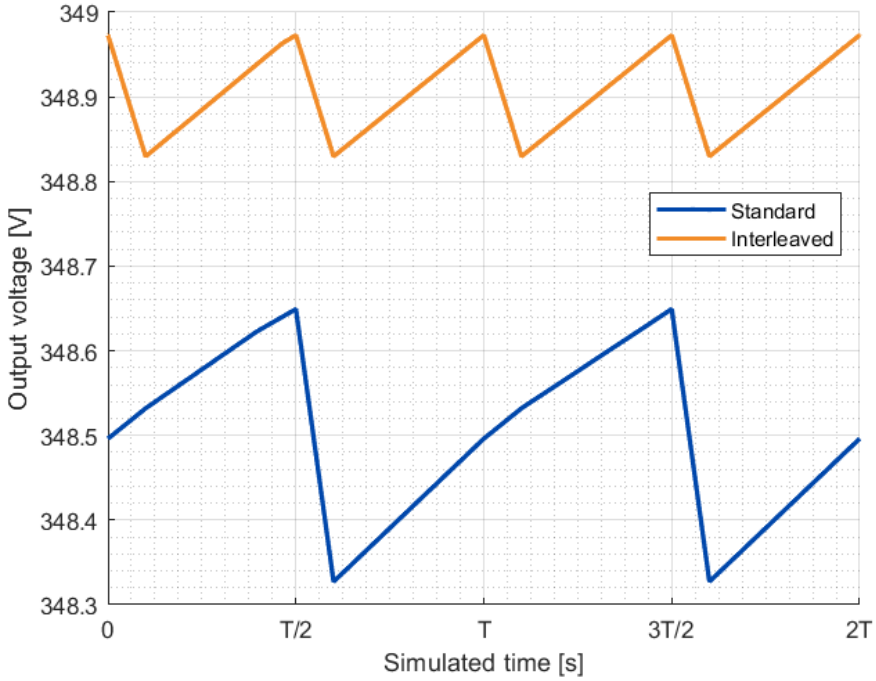

Figure 3.6: Output voltage of a single pole over two simulated time periods for a standard and interleaved configuration.

As evidenced by Figure 3.6, the output voltage ripple under the selected simulation parameters is reduced by a 44.5% through interleaving.

Overall, the electrical simulations carried out verify the correct function of the converter under different circumstances. Moreover, the data extracted from this analysis is useful in determining the rating for various components and operational parameters such as switching frequency indicated in section 3.2.

3.3.2 Thermal Considerations

Special care needs to be given to the possible issues arising from extreme temperatures in high power applications. As the output power increases, so too do the losses of various components that comprise a power converter. For this reason, electronic converters typically make use of heat-sinks in order to dissipate the heat generated through these losses.

The main agents behind increases in temperature in the designed MPPT converter are the GaN FETs and the power diodes. The fact that these devices will not experience temperatures above their breakdown value must be validated through simulations. Hence, the selected GaN FET and diode model must prove to remain within acceptable thermal limits under the entire converter operational range. Table 3.2 lists various GaN switches that could be suitable for this MPPT application. Additionally, basic electrical and cost parameters are shown.

Table 3.2: Specifications and price of various GaN switches suitable for the chosen application.

Model	Manufacturer	V_{ds} (V)	I_d (A)	$R_{ds(on)25°C}$ (mΩ)	Price (€)
GS-065-011-1-L	GaN Systems	650	11	150	2.09
GS-065-018-2-L	GaN Systems	650	18	78	4.82
GS66504B	GaN Systems	650	15	100	8.77
GS66506T	GaN Systems	650	22.5	67	10.26
LMG3410R050	Texas Instruments	600	12	50	6.80
NV6117	Navitas Semiconductor	650	12	120	3.47
NV6127	Navitas Semiconductor	650	12	125	3.47

All of these GaN switches present voltage and current ratings that satisfy the requirements of this application, as can be verified through a comparison with Figure 3.4, shown in the previous subsection. The decision to employ an interleaved configuration was taken due to initial simulations suggesting that a second string of power electronics per sub-circuit would be required in order to keep temperature values below safety margins. The typical absolute maximum temperature at which these FETs can function ranges from 125 °C to 150 °C. It must be noted that the last three FETs listed, the ones manufactured by Texas Instruments and Navitas Semiconductor, have integrated gate drivers, which would simplify the design of the MPPT converter.

Each one of these FETs could be employed for this application, theoretically. Nonetheless, the most optimal must be chosen, and it has to be concluded that the selected switch can indeed function correctly without overheating. Therefore, the thermal behaviour of these FETs are simulated for the interleaved circuit once again, given that this configuration reduces overall losses by splitting the input current into multiple phases.

The conduction and switching losses of these FETs is calculated through accurate thermal models developed either by the manufacturers of each FET, or through the characteristic energy curves present in their corresponding datasheet. These values are tested for a multiple range of balanced input voltages (same voltage across both inputs) and a constant output voltage of 350 V per pole. The input current is kept at the maximum 10 A, which returns the most intense thermal variations. Additionally, the simulation takes into account that the analyzed components are placed on top of an PCB with an FR-4 insulating substrate, given that this material is the most commonly used for PCBs, with the inclusion of an aluminium heat-sink with a thermal resistance of 0.5 K/W, since a heat-sink with this specification will be used for the final design. The ambient temperature is set to 50 °C, which is higher than the real ambient temperature under which the converter shall operate, so as to ensure that the results account for any errors in the simulation. Figure 3.7 displays the conduction and switching losses simulated per GaN FET model under the aforementioned parameters.

As shown in Figure 3.7, these FETs perform very differently under the same conditions. On one hand, the LMG3410R050 is the best in terms of conduction losses, but on the other hand, its switching losses are the highest at all voltages. Both of the switches manufactured by Navitas seem to perform comparatively worse than the FETs developed by GaN Systems in terms of both conduction and switching loss. This could be due to the fact that these FETs include an integrated gate driver, that could impact the thermal behaviour of the device. Figure 3.8 displays a graph plotting the junction temperature of each FET under the simulated conditions, so as to get a better picture of how the combination of these losses translates to thermal increase.

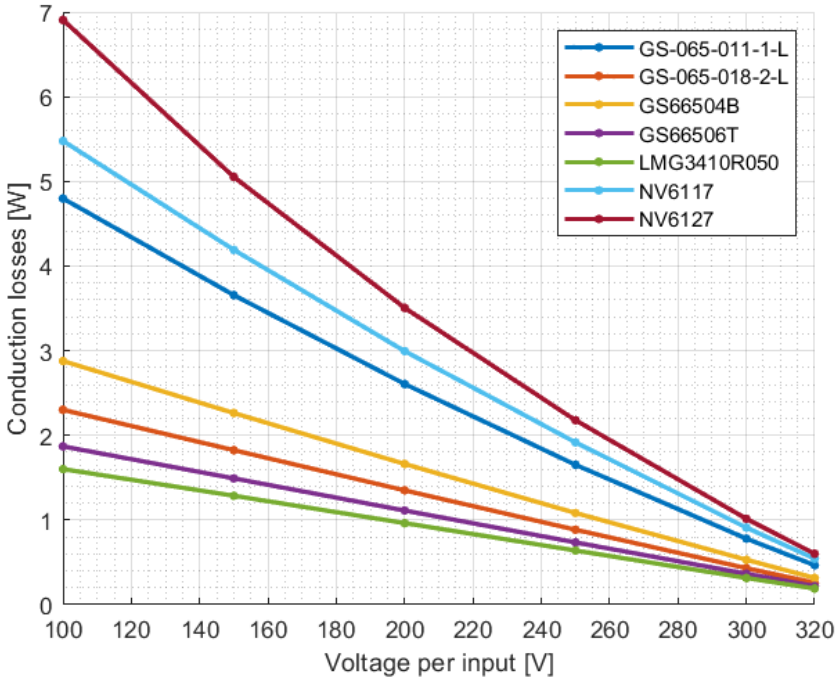

(a) Conduction losses at various input voltages per transistor model.

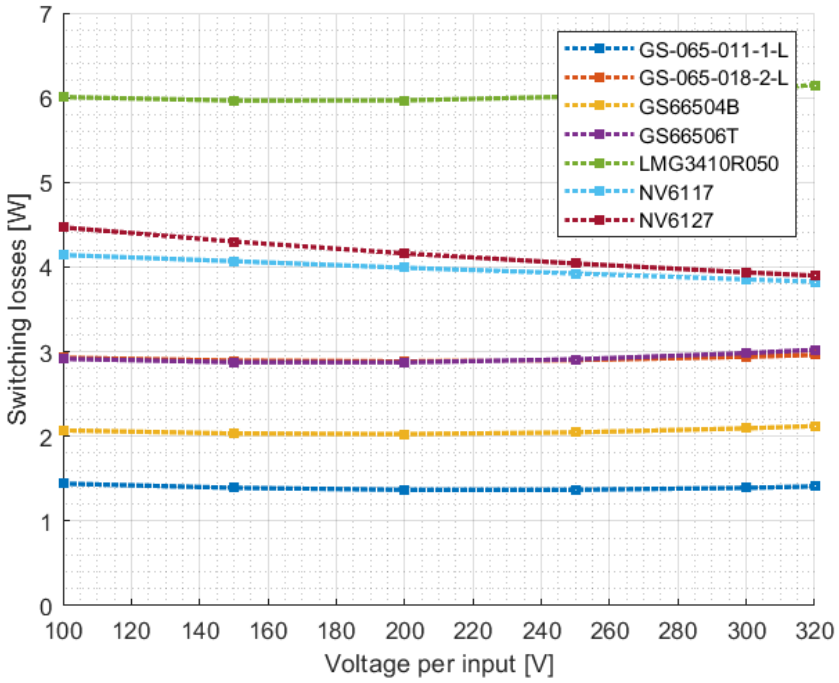

(b) Switching losses at various input voltages per transistor model.

Figure 3.7: Conduction and switching losses as a function of input voltage for each GaN FET compared.

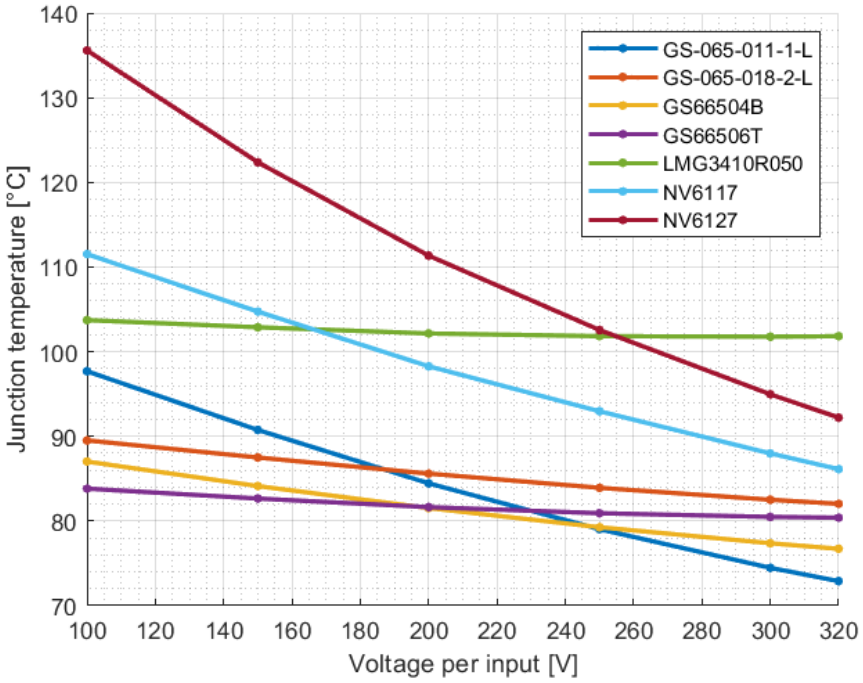

Figure 3.8: Simulated steady-state temperature as a function of voltage per input for each GaN FET compared.

As depicted in Figure 3.8, most FETs stay well below the previously mentioned typical breakdown temperatures of 125 °C to 150 °C throughout the various input voltages. The FETs manufactured by GaN Systems present the lowest steady-state temperatures over the range of operation of the designed MPPT converter. Out of these, the GS-065-011-1-L has the best thermal performance at high input voltages. Additionally, the peak simulated junction temperature of this device stays below 100 °C, and considering that the absolute maximum temperature rating of this switch is 150 °C, it can be said that it is safe to use for this application. This, in combination with its very reduced price in comparison to the other GaN FETs makes it the optimal choice for this design, since the difference in performance of the other devices by GaN Systems does not justify the steep price increases for this application. Furthermore, these thermal simulations validate the specification values displayed in section 3.2, since it can be seen that the minimum voltage selected of 100 V is within safety junction temperature limits. This is due to the fact that, as stated earlier, the GaN switch temperature at minimum input voltage and maximum current does not surpass 100 °C. A lower minimum operational voltage than 100 V could have been specified if a different GaN FET would have been chosen, however this presents multiple disadvantages: first, transistor cost would be more than doubled, since the selected switch is the cheapest compared to the other transistors that remain cooler at higher duty cycles. Secondly, operating at low voltages also means low power converted, and the conditions of current-voltage and high-current simulated would only occur under high irradiance and partial shading conditions. Hence, the benefits of lowering the minimum operating voltage are slim and do not outweigh the cost advantage of employing the selected switch.

It can also be noted that the results in temperature for a non-interleaved circuit would be considerably higher due to conduction losses scaling quadratically with current, hence the decision to employ interleaved phases is justified, especially when considering the other previously explained benefits of this topology variation.

The same simulation process was carried out for the selection of the power diodes. Following the same criteria as done for the GaN FETs, the diodes chosen are the C6D10065G by Wolfspeed, which are SiC Schottky diodes. These type of diodes present no reverse recovery losses, which contribute to the

maintenance of low temperature rises. Following the simulation procedure, these diodes were the ones that presented the lowest conduction losses, and therefore the lowest steady-state temperatures.

In light of the results presented in this section, it becomes clear that thermal management is necessary for the design of this MPPT converter. According to the simulations carried out, an aluminium heat-sink of sufficiently low thermal resistance is enough to maintain the temperature of the power semiconductor devices within safety limits, even when considering an ambient temperature as high as 50 °C. Nevertheless, in order to reduce total losses and for extra safety, accounting for the fact that the converter will be enclosed within a case, an additional thermal management measure was considered in the design of the MPPT converter. It was decided to solder the power semiconductors that belong to each interleaved phases onto multiple single-layer aluminium PCBs that are mechanically and electrically connected to the main PCB through screw terminals. These aluminium boards are physically placed below the main PCB, in direct contact with an aluminium heat-sink. Employing aluminium PCBs increases design complexity, but it greatly increases the efficiency of the converter thanks to the superior dissipation of heat that aluminium boards offer [27]. This design choice is further elaborated upon in section 3.4.

3.3.3 Simulated Efficiency Analysis

In order to estimate the performance of the designed MPPT converter prior to experimental testing, a theoretical efficiency analysis was carried out based on the simulated losses of the semiconductors as well as the core and copper losses associated with the inductor coils. Therefore, taking these losses into account, the input power provided by the PV system was compared with the output power delivered to the simulated bipolar DC grid. The data gathered was taken from a steady-state scenario, performing iterative calculations with a varying range of input and output voltages and currents, so as to get a comprehensive picture of the converter efficiency throughout multiple operating conditions.

As a first step in the data collection process, a situation of balanced input and output is assumed. This means that, for the simulation performed, both PV inputs have the same configuration and are exposed to the same irradiance, and therefore deliver the same voltage and current. Furthermore, the bipolar grid voltage for both poles is maintained at the nominal 350 V per pole. Figure 3.9 displays a representation of the efficiency data calculated of the entire converter for a range of voltage and current values per input under the previously described conditions.

As reference for the upcoming analysis, Table 3.3 showcases the calculated values for duty cycle that correspond to the input voltage levels represented in Figure 3.9 for a nominal output voltage of ± 350 V. These values are calculated through Equation 3.4 and Equation 3.5.

Table 3.3: Equivalence of various input voltages to duty cycle at nominal grid voltage.

Input voltage [V]	Duty cycle [%]
320	8.6
300	14.3
250	28.6
200	42.9
150	57.1
100	71.4

Two main conclusions are apparent in light of the data presented by Figure 3.9. First, it can be seen that the overall efficiency of the converter is heavily impacted by the voltage present at the PV input. Higher voltages result in higher efficiencies. This phenomenon is a direct result of the relationship between input voltage and duty cycle, as dictated by Equation 3.4 and Equation 3.5. As the voltage delivered by one of the PV arrays decreases, the duty cycle of the switch that is required to maintain MPPT operation increases. As a direct consequence of working at higher duty cycles, the conduction losses from the FETs quickly become dominant.

Secondly, it can be seen that efficiency presents its biggest relative decrease at very low and very high

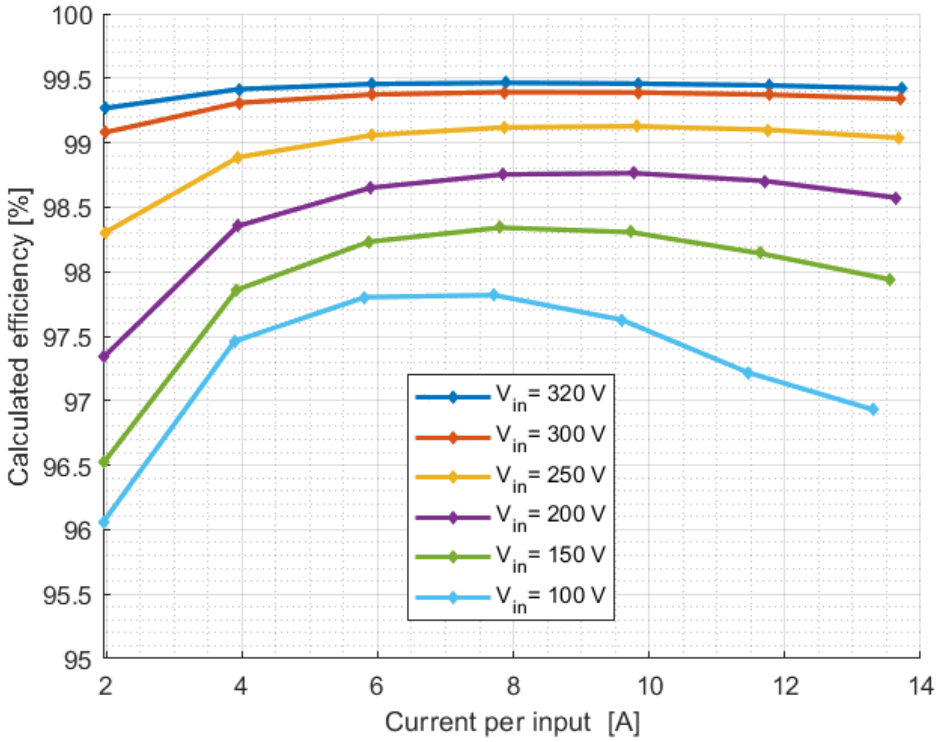

Figure 3.9: Simulated converter efficiency as a function of input current for a balanced input case.

current levels. The reason behind efficiency decreasing at high currents is easily deduced, since the higher the current provided by the PV arrays, the higher the conduction losses across the FETs and diodes, and the bigger the inductor copper losses. Hence, conduction losses are dominant at these higher currents. At very low currents however, conduction losses are really low. Therefore, the reason behind this efficiency decrease must lie elsewhere. In order to further analyze this effect, and to verify the previous conclusions, the total losses grouped by source of origin with a 350 V per output pole for different balanced input voltages is displayed in Figure 3.10.

The graphs presented in Figure 3.10 display the total losses in the system divided in groups according to the components and mechanisms that cause these losses as a function of input current for different input voltages. The previous conclusions can be easily verified through these graphs: FET conduction losses grow exponentially quicker for lower input voltages (and hence higher duty cycles), and additionally it can be seen that this growth offsets the one presented by the diode conduction losses, leading to combined higher losses at higher duty cycles as observed in Figure 3.9. When comparing Figure 3.10a and Figure 3.10d at 10 A of operating current, the FET conduction losses are 9.85 times higher for the 100 V graph than for the 320 V graph, while the diode conduction losses are only 3.28 times lower. This results in a net decrease of overall efficiency when at higher duty cycles. Inductor copper losses raise as a function of input current, and as expected they do so at an equal rate for all voltages and duty cycles, as is the case with the FET switching losses.

Nevertheless, the reason behind the lower efficiencies observed at low currents is now clear: the inductor core losses remain relatively constant for all input current levels in each graph, and so at very low currents these losses become proportionally more impactful. The core losses across the inductors are dependent on the frequency of operation and inductor current ripple. Inductor current ripple values are at their highest for duty cycles close to 50%. At 200 V of input voltage, the calculated optimal duty cycle is 42.9%. Hence, the core losses are high and prevalent compared to other loss mechanisms at very low currents. Lastly, it can be observed that the selected diodes present virtually no reverse recovery losses.

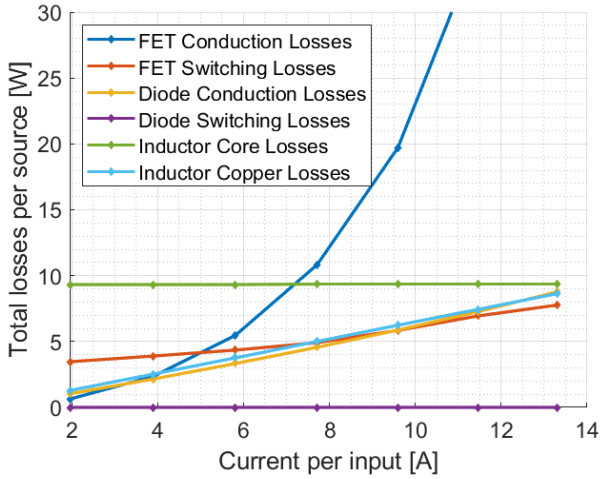

(a) Input voltage of 100 V per input.

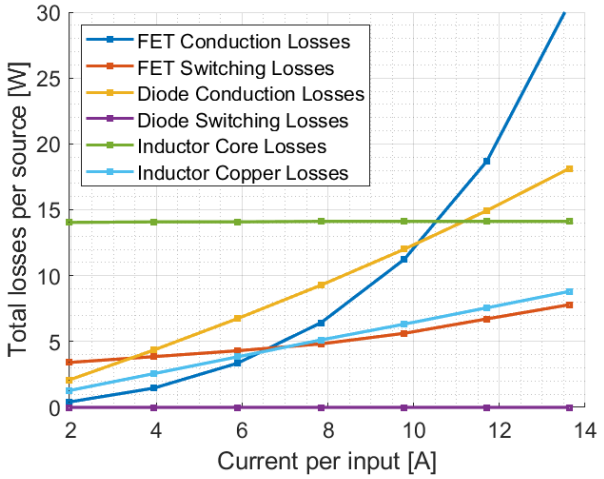

(b) Input voltage of 200 V per input.

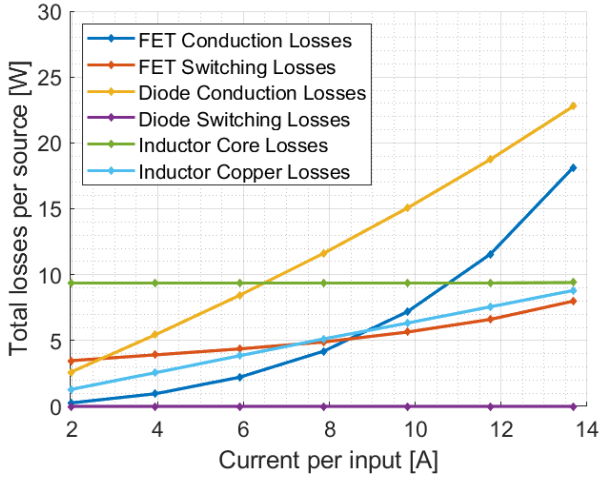

(c) Input voltage of 250 V per input.

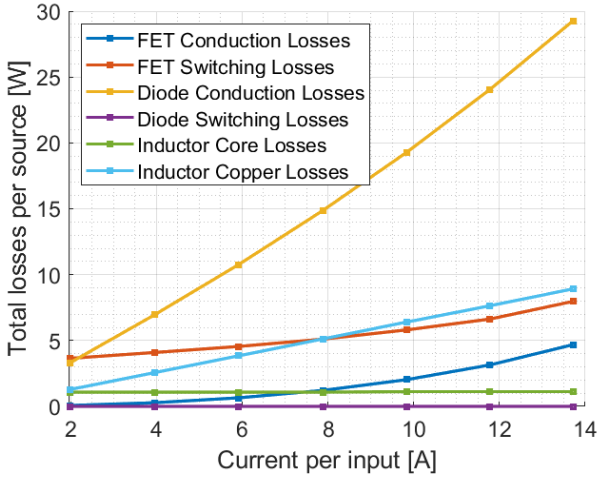

(d) Input voltage of 320 V per input.

Figure 3.10: Losses breakdown vs. input current for various balanced input voltages at 350 V per grid output pole.

The previous simulations were performed under the assumption that the bipolar grid remains balanced at a voltage value of 350 V per pole. Another iteration of the simulation process was carried out for the purpose of observing the effect that the voltage of the bipolar grid can have on the overall converter efficiency. Therefore for this iteration, a constant PV input voltage is considered, and instead the pole voltages, V_{out+} and V_{out-}, are given different values according to the minimum, nominal and maximum values acceptable for proper MPPT operation. Hence, Figure 3.11 showcases the resulting efficiency values as a function of percentage of rated output power for different grid voltage combinations. The PV voltage delivered is maintained at 320 V for both inputs.

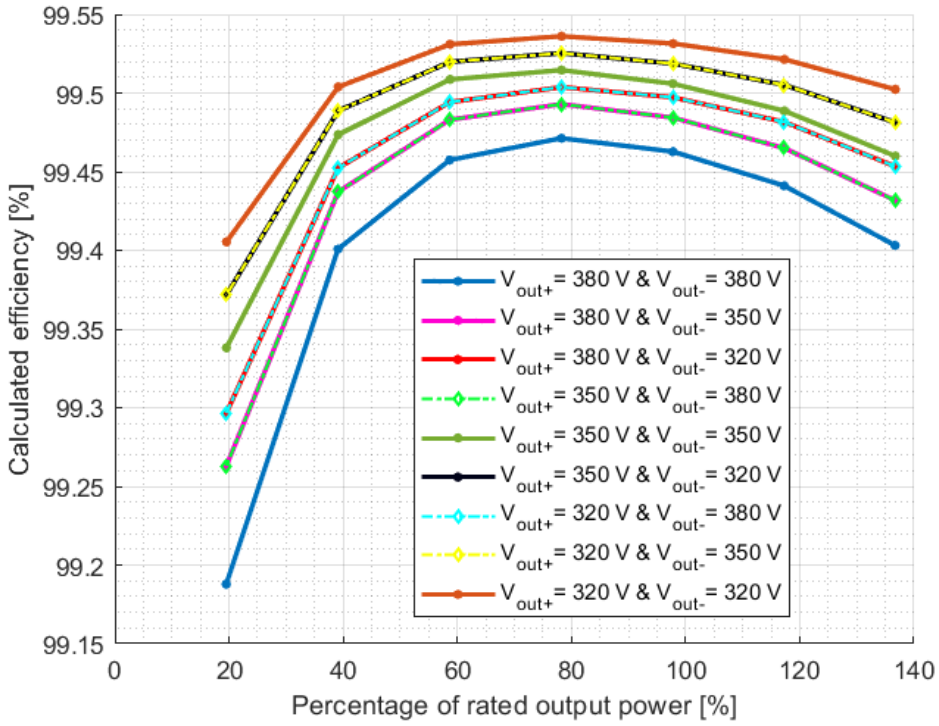

Figure 3.11: Converter efficiency as a function of rated output power percentage for different bipolar grid voltages.

After observing the graph presented in Figure 3.11, it can be noticed that pole voltage combinations that result in higher total positive-to-negative line voltages result in higher total losses. Once again, this is a direct result of duty cycle increases and the predominance of FET conduction losses under these conditions.

In addition, an interesting observation lies in the fact that different pole voltage combinations that present the same voltage levels in reverse poles (e.g. an output voltage of 320 V in the positive pole and 380 V in the negative one when compared to a voltage of 380 V in the positive pole and 320 V on the negative output) derive in equal total losses, and therefore same efficiency. This phenomenon further supports the assumption that the MPPT converter proposed can be analyzed as two independent sub-converters, since a variation in output voltage on one sub-circuit results in the same overall losses when replicated in the other sub-circuit.

Overall, the converter efficiency values obtained through these simulations yield promising results. Furthermore, the information derived from this analysis has provided valuable insight into the loss mechanisms and which issues should be tackled in order to improve performance in the future. As a summary on the data procured in this section:

- The efficiency of both of the circuits that comprise the converter can be analyzed independently.

- At high duty cycles, the growth in FET conduction losses is dominant over the reduction in diode conduction losses.
- Inductor core losses are the main source of power loss for low input currents and duty cycles close to 50% due to current ripple.

3.4 Design Overview and Component Selection

During the following section, the different elements that comprise the designed MPPT converter will be showcased. Additionally, the components selected for the design are specified. Figure 3.12 displays a simplified block overview of the layout of the converter.

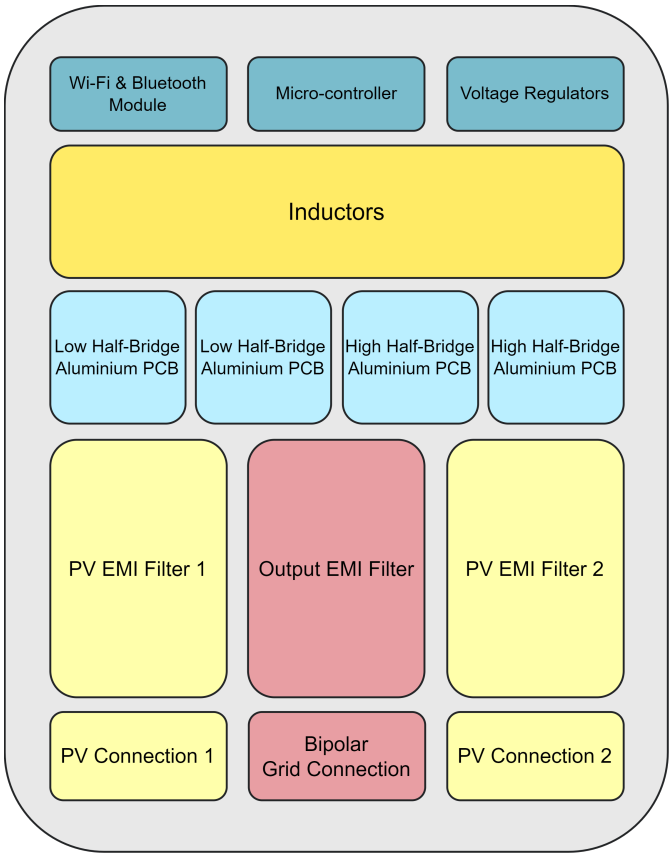

Figure 3.12: Simplified block overview of the converter layout.

The converter is composed of a main board, mostly populated by passive components, and four aluminium PCBs that house the half-bridges, a denomination given to the power electronic components that carry out the switching operation, namely the transistor and diode pairs. Each of these boards correspond to one of the two interleaved phases of each of the two sub-circuits that comprise the converter.

As mentioned in subsection 3.3.2, the aluminium boards are situated below the main board, and are connected to the main board through screw terminals and pin connectors. The reason behind this configuration is that the thermal dissipation capabilities of using single-layer aluminium PCBs is much superior to those of standard FR-4 PCBs. However, this comes at the cost of increasing design complexity. The aluminium boards are in direct contact with the aluminium heat-sink to optimize efficiency and thermal dissipation. The heat-sink counts with a thermal resistance of 0.5 K/W. Given that the GaN HEMTs and the diodes will sustain the highest temperature increases, these are the components that will be mounted on the aluminium boards. Additionally, the fact that multiple aluminium PCBs are used for the power electronics, instead of only one, increases the modularity of the overall design by allowing

these parts to be replaced and modified easily. Compatibility with future designs is also enhanced through this modular design.

Figure 3.13 showcases the half-bridge single-layer aluminium PCBs. Two different designs are employed for the two sub-circuits that comprise the converter. The left side of each board contains a gate driver circuit that operates the GaN HEMTs, while the GaN HEMT, diode and screw terminals can be found to its right. The PWM signals and required voltage signals are fed from the main board through a four-pin connector. It must be noted that the design of these half-bridges was effectuated considering the possibility of paralleling another string of power semiconductor components. This was a safety measure in case the thermal increase of these components proved dangerous during testing. Under such a scenario, an extra string of power electronics can be soldered onto these boards in order to further improve efficiency at the cost of more components. However, according to the thermal simulations performed, this is not necessary for proper converter operation, since the losses generated by these components are already well below safety limits.

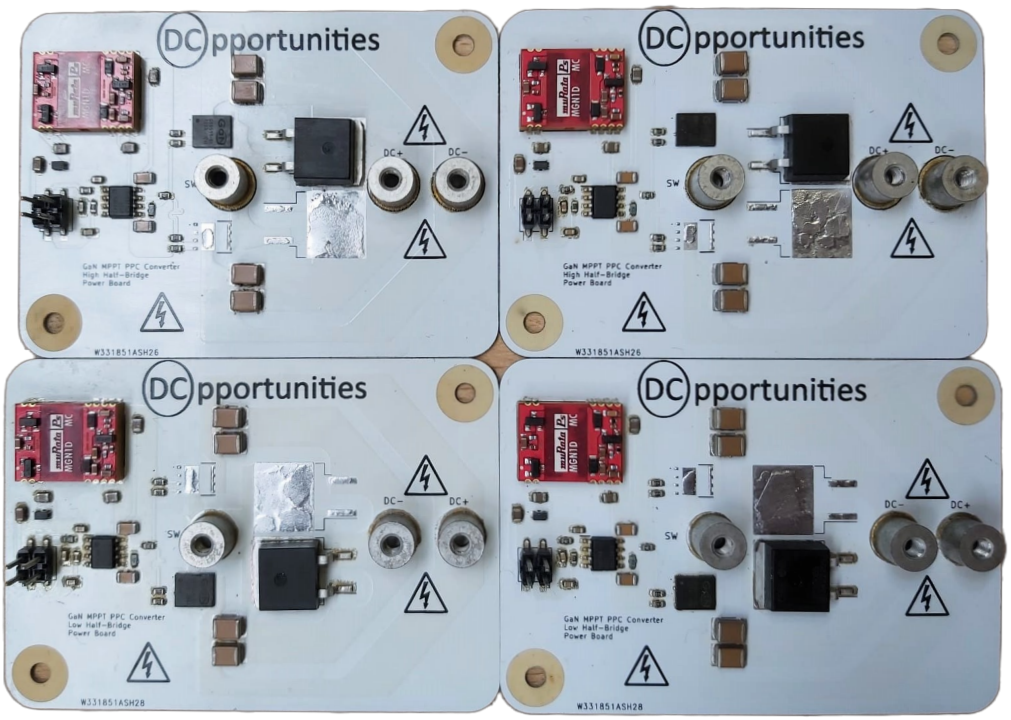

Figure 3.13: Aluminium half-bridge PCBs for power electronics.

As seen in Figure 3.12, all of the converter connections are situated in the lower part of the main board, with corresponding EMI filters for noise reduction. These EMI filters are explained in detail in subsection 3.4.1. The input power of each side is sent to a pair of inductors, one per interleaved phase, which are placed on top of a plastic mount at the top of the board. These inductors are connected through screw terminals to the aluminium PCBs, that convert the power received in order to perform MPPT operation. All of these half-bridge aluminium PCBs are connected to the output of the converter, situated in the lower centre of the main board. Since the inductors are placed on top of a plastic structure, additional micro-electronic components and voltage regulators can be placed below them without the need to increase the size of the main board. These statements can be observed in Figure 3.14, in which the fully assembled MPPT converter designed is presented. The assembled converter has a total surface area of 23 cm of width and 27 cm of length.

The following subsections elaborate on the design and specific components selected for the different elements that constitute the MPPT converter.

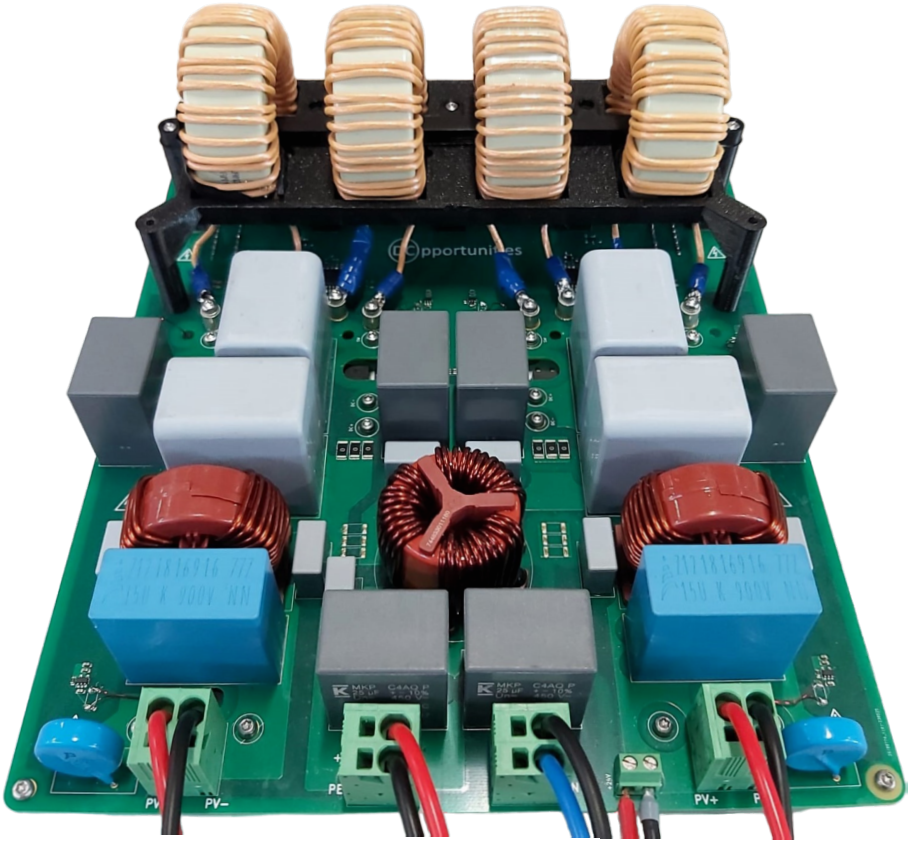

Figure 3.14: Fully assembled MPPT converter based on GaN switching for bipolar DC grids.

3.4.1 Input and Output Connections

For the PV input to PCB and output to grid connections, four PCB terminal blocks with two connections each are used. The component chosen is the 1719312, manufactured by Phoenix Contact. The current rating capabilities of these connectors are suited for nominal currents of 41 A, well above the maximum operating currents that will be present at the inputs and output of the MPPT converter. Two of these terminal blocks are used for the positive and negative connections to both PV inputs, while the other two terminals are used for the positive, neutral and negative connections to the bipolar DC grid, with an additional connection to protective earth. These four terminal blocks can be seen on the bottom of Figure 3.14, with each of them having two cables attached.

Furthermore, EMI (Electromagnetic Interference) filters have been implemented in direct connection with both inputs and output terminals. An EMI filter is a low pass filter that takes an electrical signal at its input and yields a modified signal at the output, removing or decreasing the amplitude of all frequency components of the signal that are above the filter's cut-off frequency [28]. Through the use of EMI filters, undesirable radio frequency noise can be significantly reduced. These radiated emissions must be below certain EMC (Electromagnetic Compatibility) limits set by regulatory bodies if a product is to be distributed and commercialized.

The designed EMI filters are based on third-order filters, typically referred as π (pi) filters. For the PV inputs, these filters are composed of three capacitors between the positive and negative lines (type X) to reduce noise caused by differential mode currents, and a common mode choke in combination with two capacitors connected from the positive and negative line respectively to ground (type Y), in order to decrease common mode noise. The capacitance present in these EMI filters also serves to reduce the voltage and current ripple of the signals it filters. The following Figure 3.15 shows the circuit schematic for these EMI filters.

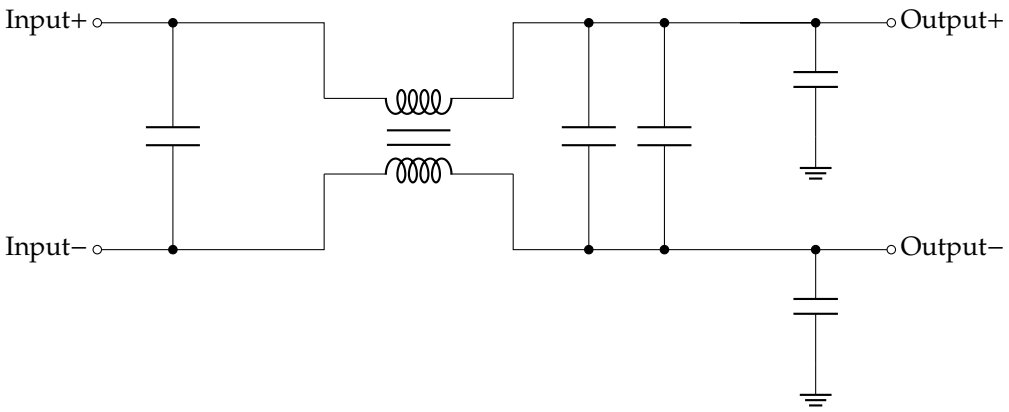

Figure 3.15: Input EMI filter circuit diagram.

The common mode choke used for these EMI filters is the 744831016164 by Wurth Elektronik. This choke counts with a maximum DC current value of 16.4 A, high enough for the expected nominal currents delivered by the PV strings. Additionally, the coil is shielded for better EMC performance. These chokes, one per input, are the red round components visible in each side of the converter in Figure 3.14. The type X capacitors are rated for 900 V, and have a capacitance of 15 uF at the PV EMI input and 20 uF for the EMI output. The part numbers of these capacitors are B32776Z9156K000 and MKP1848620094P2, respectively. On the other hand the type Y capacitors, product BFC233660333, have a capacitance value of 33 nF.

The output EMI filter presents a similar configuration, adapted to the three lines that compose the bipolar DC output. The three-phase choke used is the 744833011180 manufactured by Wurth Elektronik. This three-phase choke is the red component situated at the center of Figure 3.14. For this design, the type X capacitors, connected to each pole, are rated for 450 V. This voltage rating is sufficient, given that the voltage of a pole of the bipolar grid will range from 320 V to 380 V. These capacitors are the C4AQGBU5250P12K, which present a capacitance of 25 uF. The Y type capacitors used are the same as for the PV EMI filter.

It is relevant to mention that accurately foreseeing the amount of EMI noise through simulations is a particularly arduous task. For that reason, the design of EMI filters is often iterative, based on EMC tests performed after the initial design. As a consequence of this limitation, the EMI filters designed for this converter are a first design based on basic frequency calculations, and so, the designed filters are not optimized for the actual noise caused by the converter.

Additionally, as part of the PV input design, a MOV-20D152K varistor has been added in a parallel connection to both PV inputs. This varistor, rated for 1.5 kV, serves as a protective device in case of high voltage surges that could damage the converter.

3.4.2 Power Semiconductors

As stated earlier in this chapter, the interleaved phases of the MPPT converter are comprised of two half-bridges, which in turn are constituted of a GaN HEMT and a diode each. Both of these components are essential to the overall function of this MPPT converter, and so special care has to be taken to guarantee that the best option is chosen based on its characteristics, such as nominal ratings, efficiency and cost.

The chosen GaN FET for this application is the GS-065-011-1-L, manufactured by GaN Systems. This product is rated for voltages up to 650 V and currents up to 11 A. As verified through electrical simulations, these values are well above the maximum limits expected across the FETs, especially considering that the interleaved configuration halves the current that travels through a given transistor during the on state. Furthermore, these switches present a relatively low ($R_{DS_{on}}$) of 150 mΩ. This translates to low conduction losses, which is especially relevant for high power applications. Based on the thermal simulations performed, these FETs outperform similar GaN FETs within the same price range and

current rating, as explored in section 3.3. Additionally, this device is also contained within a very small package of only 5 mm of width, 6 mm of length and 0.85 mm of height. This impacts power density, resulting in a smaller PCB size required to place the half-bridges.

The main drawback behind the selection of this GaN HEMT when compared to other switches in the market lies in the fact that it does not incorporate an integrated gate driver. This means that a gate driver circuit needs to be designed and built in order to guarantee proper functioning of the switches.

As for the diodes, the optimal technology for this application is SiC Schottky diodes. This is because the thermal conductivity of SiC diodes is very high when compared to other diodes, and their switching behaviour is relatively impervious to temperature increases, since this technology presents virtually no reverse recovery losses [29]. These advantages make these semiconductors a very favourable choice for high power applications, in spite of the fact that SiC technology is not optimized for very low forward voltage drops, which can negatively impact efficiency through an increase in conduction losses. For these reasons, the selected diode, part number C6D10065G by Wolfspeed, is based on this technology. This diode presents a breakdown voltage of 650 V and a current rating of 10 A, similar to the ratings of the GaN HEMT. The forward voltage of this diode is 1.27 V. While this value is not among the lowest for power diodes, it is substantially lower when compared to diodes that make use of the same technology as this one.

It is also crucial that the selected FETs and diodes present bottom-side cooling, considering the selected configuration of placing the power electronics on single-layer aluminium PCBs for optimal thermal management.

3.4.3 Gate Driver Circuit

As established in the previous subsection, a gate driver needs to be integrated to the converter design in order for the HEMTs to operate correctly. Gate driver circuits can provide galvanic isolation by electrically separating different parts of the circuit and therefore being able to distinguish between different ground potentials. Galvanic isolation is often required in applications where an operator might need to interface with a specific part of the circuit. This isolation reduces the voltage levels of the side of the circuit that will need to be interfaced with to non life-threatening levels, so that the safety of the operator is guaranteed. For this particular application, no human interface is required in order to control system operation. Nonetheless, the gate drivers to be employed may still require isolation due to other conditions.

For this topology, the upper side HEMTs do not require an isolated gate driver, given that the source of the transistors is connected to the DC grid neutral line, and hence ground, and so the gate-source voltage can be referenced to this ground in order to operate the device. It will then be sufficient to apply a gate-source voltage higher than the threshold voltage in order to activate the HEMTs. However, this is not the case when it comes to the lower side HEMTs. In this case, an isolated gate driver is necessary. This is due to the fact that the sources of these HEMTs are connected to the cathode of the lower side diodes, which in turn have their anode connected to the negative pole of the bipolar grid. Therefore a gate-source voltage higher than the voltage difference between the source of the HEMT and the negative pole of the grid would have to be applied in order to turn each device on. Of course, this is not feasible in practice. And so, an isolated gate driver must be used, not because of safety concerns, but because it is required to guarantee correct functioning.

Although, as previously stated, the upper side HEMTs are not subject to the same conditions as the low side HEMTs when it comes to driving, employing isolated gate drivers can also prove useful. This is due to the fact that this isolation protects the low voltage electronics present in the driving circuit from damage caused by any possible faults on the high power side. Moreover, isolated gate drivers often provide better noise immunity at the cost of a slightly more complex design [30]. Since isolated gate drivers are nonetheless required for the lower side HEMTs, there are no concerns related to higher complexity. Therefore, the same driving configuration can be applied to all HEMTs in the system, simplifying the production process of the converter by maintaining uniformity in the design of both half-bridges. Consequently, the following Figure 3.16 shows the designed gate driver circuit applicable for all half-bridges.

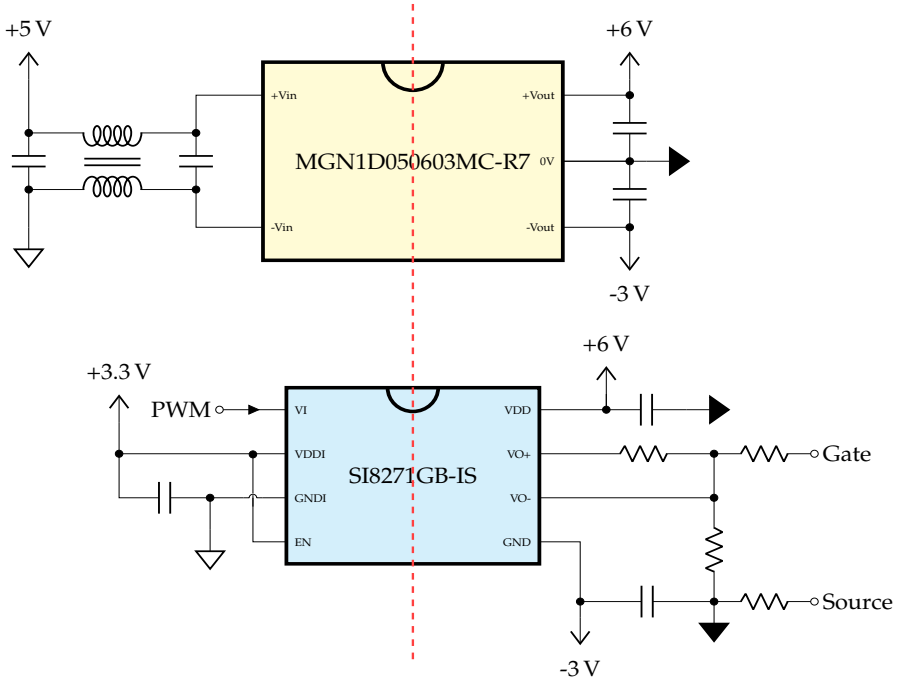

Figure 3.16: Isolated power supply and gate driver circuit designed.

The circuit was designed considering the option that paralleling two FETs could prove interesting when testing the converter to measure efficiency improvements. This is despite the fact that according to the thermal simulations performed, using interleaving and not paralleling devices was demonstrated to be viable from a thermal management standpoint. Therefore, to leave the option of paralleling these semiconductors open during testing, the isolated gate driver Si8271GB-IS was selected considering that its driving current is high enough to feed the same gate signal to two parallel switches. The isolation on the output side is created by feeding 5 V to the input of a MGN1D050603MC-R7 isolated power supply, which generates two voltage outputs of 6 V and -3 V referred to an isolated ground. These values are within the gate threshold limits of the selected HEMTs. Additionally, a small common mode choke is placed at the input side of the power supply in order to reduce noise. The part number of this filter is ACM2012-201-2P-T002.

It is to be noted that accidental activation of the FET during the turn-off period can occur due to the internal parasitic capacitance of the device not discharging fast enough. This is known as the Miller effect. In order to prevent this behaviour, the negative voltage of -3 V from the power supply is applied during turn-off across the gate and source of the device. This negative voltage ensures that the gate-to-source voltage remains well below the possible activation threshold of the device during turn-off operation [31].

Additionally, in pursuance of eliminating high-frequency noise, a low pass RC filter is implemented at the PWM input of the gate drivers. The frequency of operation of the PWM signals is 125 kHz. Therefore, an RC filter with a cut-off frequency high enough above this value will be used in order to reduce the noise of undesirable high-frequency signals. The cut-off frequency of a low pass filter is defined as the frequency at which an attenuation of 3 dB is attained, with subsequent frequencies above this value presenting a faster gain decay rate. The following Equation 3.10 shows the expression that returns the cut-off frequency F_c based on the resistance (R) and capacitance (C) values of the filter.

$$F_c = \frac{1}{2\pi \cdot R \cdot C} \tag{3.10}$$

With a resistance of 47 Ω and a capacitance of 22 pF the resultant cut-off frequency is 1.54 MHz. This cut-off frequency value was chosen with the criteria that it should be at least 10 times higher than the

frequency of the input PWM signal. This way, the cut-off frequency is high enough so that the PWM signal is not attenuated for the chosen frequency of operation.

Lastly, it is relevant to mention that gate driver circuits must be placed as close as possible to the FET that they control, to ensure fast and reliable operation by minimizing parasitic inductance. Therefore, these components are situated on top of the aluminium PCBs, despite the fact that the heat generated by the components that constitute the gate driver circuit is negligible.

3.4.4 Inductors

One of the key elements in the power conversion process are the inductors. The four inductors, one per each half-bridge, are situated in a plastic mount manufactured at the laboratory of the company. This structure is placed over the low-power SMD components, which helps in reducing the PCB area required to fit the inductors as compared to using standard SMD or through-hole components. Each inductor is composed of a magnetic core and a conducting wire that is wrapped around it. The terminals of each of these wires connect the PV input side to the corresponding half-bridge. Figure 3.17 displays one of the inductors assembled and used for the manufactured converter.

Figure 3.17: Lab-assembled inductor composed of a ferromagnetic core and a wire winded around it.

The inductor core selected for this application is the KAM250-125A, a toroidal soft ferromagnetic core made from ferrous alloy powder. This core has a relative magnetic permeability of 125 µ. The higher this value, the stronger the magnetic field generated. The number of turns by which a conducting wire is winded around its corresponding core determines the inductance value of the inductor. As established in section 3.3, the desired inductance is equal to 400 µH per inductor. The corresponding number of turns required to achieve this value directly depends on the physical properties of the selected core. A simplified expression that describes this relationship for toroidal cores is given by Equation 3.11, where N is the number of windings, L is the desired inductance value in µH, μ_r is the relative permeability of the core material, h is the core width in mm, D_o is the outer diameter of the toroid and D_i is its inner diameter.

$$N = \sqrt{\frac{L}{2 \cdot 10^{-4} \cdot \mu_r \cdot h \cdot \ln(\frac{D_o}{D_i})}} \tag{3.11}$$

Substituting the selected inductor core parameters in Equation 3.11, the minimum number of wire turns required for an inductance of 400 µH is 32. Therefore, considering the electrical simulation results carried out, wrapping the conducting wire more than 32 times around the chosen core will result in an inductor current ripple of less than 15% of rated current during maximum power operation.

3.4.5 Micro-electronics and Measurements

The MPPT converter is controlled through a micro-controller placed in the main board, physically distant from high-power components. The main tasks of the micro-controller are to send PWM signals to the half-bridges in order to activate the switches according to the programmed control algorithms, to read various relevant measurements in the form of analogue signals and to interact with a Wi-Fi and Bluetooth module meant for wireless data transmission. The micro-controller selected for this application is the STM32G474RET6, by STMicroelectronics. This micro-controller is a 64-pin device with a program memory size of 512 kB, up to 17 multi-purpose timers that can be used to generate the PWM signals, up to 42 ADC (Analogue-to-Digital Converter) channels for interpreting analogue measurements, and three USART peripherals to establish communication with the wireless module.

The Wi-Fi and Bluetooth module used for this design is the ESP32-WROOM-32E. Through a connection between this module and the micro-controller, it is possible to remotely monitor measured parameters and configure the control of the converter.

Carrying out the measurement of various parameters is not only useful to assess the performance of the converter, but some measurements are also essential for the appropriate operation of the MPPT control algorithm implemented. For this MPPT converter, measurements are taken for both PV input voltages, for the positive and negative pole output voltages, for each of the four inductor currents, and for the temperature of six thermistors, which are glued to the power semiconductors components (GaN HEMTs and diodes), since these are the devices that will experience the highest temperature increase.

In order to perform the aforementioned voltage measurements, the voltage level at a specific point needs to be reduced so as to generate a low voltage signal that can be received by the micro-controller. This is done through the use of a voltage divider circuit, as shown in Figure 3.18. The circuit employed takes a high-voltage signal as an input and converts it to a low-voltage one that varies in value in accordance to the resistors chosen. Taking into account the values of the resistors placed in the voltage divider, the micro-controller can compute the voltage value of the original high-voltage signal measured. An RC filter is used in order to reduce noise. An operational amplifier is also employed so as to serve as a buffer or voltage follower, so that the micro-controller pin that will receive this signal is isolated from the voltage divider, and so that the output current delivered is increased. Additionally, as shown in Figure 3.18, it is worth noting that the voltage divider used for negative voltage measurements is referenced to a positive voltage provided by an auxiliary supply, as opposed to being connected to ground.

The inductor current measurements are taken through the current sensor MCA1101-20-3. This device can measure currents up to ±20 A, and presents a high frequency response in order to react to the fast changes in inductor current due to the switching of the GaN HEMTs. Through the use of this component, a voltage signal that is dependent on the current measured is sent to the micro-controller, which in turn can interpret this value.

In the interest of measuring the temperature of the HEMTs and diodes in the power boards, thermistor-based temperature measurement circuits are used. A thermistor behaves as a resistor with a variable resistance based on its temperature. By placing the thermistor as one of the resistances in a voltage divider configuration, similar to the one shown in Figure 3.18, a voltage signal that varies with temperature can be generated. This allows the micro-controller to calculate the temperature of the thermistor based on the voltage signal measured. A buffer operational amplifier is also considered in this design, so as to serve the same function as described for the voltage measurements. The thermistors employed for this application are the NXFT15WF104FEAB035, which count with a negative temperature coefficient. These thermistors can be glued to the power semiconductors in the aluminium boards, while their wire leads are soldered to the main board, inserting the cables through holes in the main PCB, so that the output voltage signal can be sent to the micro-controller without the need for more pin connectors. Based on this voltage signal, the micro-controller calculates the temperature of the thermistor, resulting in an accurate measurement.

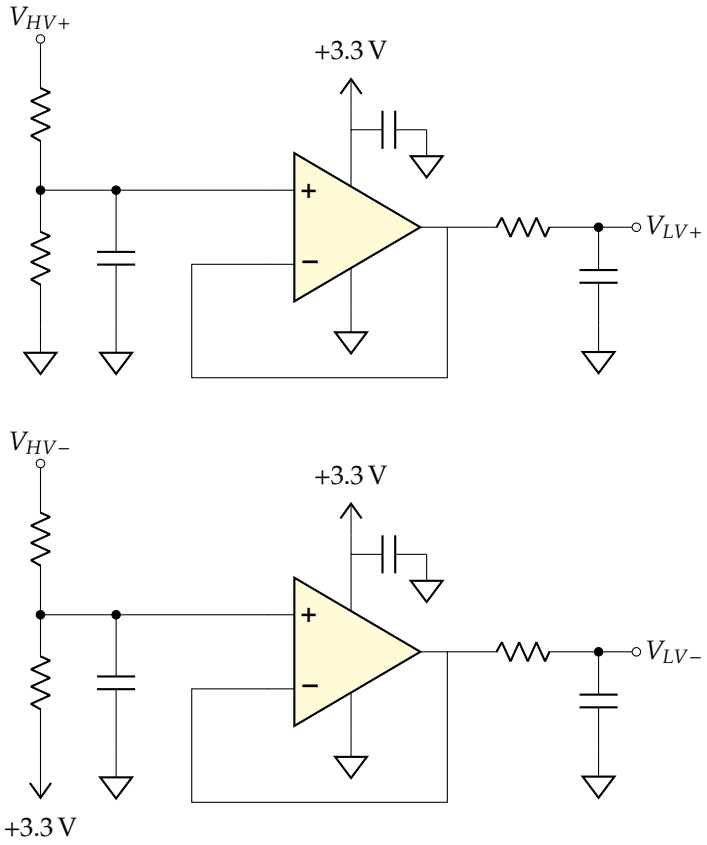

Figure 3.18: Measurement circuits for positive (top) and negative (bottom) voltages.

3.4.6 Auxiliary Supply and Voltage Regulators

Multiple circuits and components across the converter rely on various voltage signals in order to operate. This is the case for the operational amplifiers employed for measurements, the current sensors, the micro-controller unit, the Wi-Fi and Bluetooth module, as well as for the gate drivers, among other components. Hence, an external 24 V power supply is used in conjunction with a buck converter and low drop-out voltage regulators to generate 5 V and 3.3 V signals that can power up these components.

The 24 V and a ground reference channel from the auxiliary supply are connected to the MPPT converter through the two-potential PCB terminal block 1729128. The 24 V signal received is then fed through a voltage regulating circuit based on the buck converter AP64351QSP-13. This converter steps down the external 24 V to 5 V. These 5 V are required to feed the isolated power supplies for the gate driver circuits. Moreover, these 5 V generated by the buck converter can be fed to the low drop-out voltage regulator TLV1117-33CDCYR, which steps down the voltage signal yet again in order to produce an output of 3.3 V. This output voltage is employed to supply power to the remaining micro-electronic components, including the micro-controller and gate driver.

Additionally, another voltage regulator, the TL1431ACL5T, is used to generate a separate and higher precision 3.3 V voltage level originating from the 5 V one. This voltage is especially filtered and meant to be used only for analogue pin connections in the micro-controller, so as to avoid noise derived by voltage variations that may be caused by other components that require the same voltage level. This is due to the fact that analogue circuitry is more susceptible to voltage drops.

3.5 Control Logic

Configuring a control logic for the micro-controller to follow is essential in order to carry out MPPT operation. For this purpose, the control algorithm followed by the micro-controller governs the operation of each GaN HEMT independently. The micro-controller considers the voltage, current and temperature measurements received and executes an MPPT algorithm separately for both PV inputs, thus maximizing the overall power delivered at the output of the converter by adapting each operation to the conditions of a single PV input.

There a variety of established methods to implement an MPPT algorithm. These techniques differ in terms of complexity, cost, speed, and required sensed input signals, among other parameters.

The chosen MPPT method for this application is the one known as Perturb and Observe (P&O). This method evaluates the power produced by the PV array at a given instant based on voltage and current measurements. Following this, the algorithm adjusts the duty cycle in order to cause a perturbation in voltage and calculates the power delivered by the PV array once again. If an increase or decrease in voltage yields a higher power compared to the previous cycle, the algorithm will increment or decrease the voltage once more during the current cycle with the same perturbation. If instead the previous perturbation caused a lower power yield, the next voltage variation will be opposite in sign, hence the direction of the perturbation is reversed (e.g. if an increase in voltage in a given cycle results in less PV power delivered, the algorithm will lower the voltage during the following cycle) [32].

The P&O technique is very commonly employed due to its simplicity and the balance it strikes between complexity and performance [33]. However, it must be noted that this method is not the fastest in terms of dynamic response, and one of its drawbacks is that the algorithm can cling to a local maximum power point instead of to the global peak power point under partial shading conditions [34].

At high grid voltages where MPPT operation is no longer feasible, a droop control strategy is implemented. As opposed to regular MPPT control, droop control aims to regulate output voltage instead of maximizing the power delivered by the PV system. This control is implemented when output voltage approaches the maximum grid limit.

3.6 PV System Considerations

As stated in section 3.2, the DC-DC MPPT converter for bipolar DC grids described in this thesis was designed in accordance with specifications delimited by an application that will be developed by the company in which this thesis project was executed. This application consists of a small to mid-sized parking lot for electric vehicles (EVs). This parking lot will operate entirely through a bipolar DC microgrid, and the energy required to charge these EVs will be supplied through a solar PV system, hence why an MPPT converter such as the one designed is necessary. This section aims to take into consideration the characteristics that a PV system, such as the one envisioned for the EV parking lot, should present in order to guarantee optimal integration with the MPPT converter.

One of the key factors that must be considered when taking into account a PV system that would suit the application for which the MPPT converter is designed can be found in the way the connection between these two objects is made. As seen in section 2.2, an MPPT converter is typically connected to a PV system in one of three configurations: centralized, distributed at string-level or decentralized at module-level.

For this application, using the designed MPPT converter at module-level can be discarded as an optimal choice, given the input voltage levels that are required in order to deliver high power at the output. The typical input voltages of operation are too high for a single module to provide. If this issue was to be circumvented through the use of thin-film solar modules, which can deliver very high voltages relative to other technologies, a new problem would arise from an input current standpoint. Thin-film PV can deliver high voltages at the expense of low currents, which would negatively impact the power conversion capabilities of the converter.

As for the choice between centralized and string-level distribution, the optimal solution is reliant on the overall PV array layout. On the one hand, for small PV arrays, whose voltage and current output properties match those of the converter, a centralized distribution is preferred. On the other hand, when dealing with a large-scale PV system, multiple units of the designed MPPT converter are required at a string-level, in order for the PV input to conform to system specifications. Additionally, the drawbacks of employing the P&O methods as the control logic during partial shading conditions can be minimized through string-level configurations, where the MPPT algorithm for each string is non-dependent on the shading affecting other strings.

Different PV technologies can constitute a PV system that would suit the considered application. As stated in section 2.1, the most prevalent technology in the industry is mono-crystalline silicon, followed by thin-film materials. PV modules manufactured through the use of these two technologies can display substantial parametric differences. Table 3.4 showcases this by listing the parameters of two representative PV modules for each technology. The mono-crystalline silicon panel selected for this comparison is the JAM60S10-345, manufactured by JA Solar, while the thin-film module chosen is the FS-6460 by First Solar, based on cadmium telluride.

Table 3.4: Parameters at STC for two representative solar modules of different PV technologies.

Parameter	Symbol	Mono-crystalline Si	CdTe
Nominal Power	P_{max}	345 W	460 W
Module Area	A_{PV}	1.68 m^2	2.74 m^2
Rated Voltage	V_{mpp}	34.99 V	188.8 V
Rated Current	I_{mpp}	9.86 A	2.44 A
Open-circuit Voltage	V_{oc}	41.76 V	222.9 V
Short-circuit Current	I_{sc}	10.54 A	2.59 A
Average Efficiency	η	20.5%	18.6%

The optimal number of PV modules to be placed when employing the designed MPPT converter is dependent on the converter specifications. Therefore, the number of PV panels to be connected in series per input is decided as a function of the input voltage range of the converter. Similarly, the preferred number of parallel strings must fall within the specified current ratings.

Taking as reference a PV system built using PV modules based on mono-crystalline silicon, the most common technology in the industry, it can be concluded that the PV inputs of this converter will typically be connected to a single string of series-connected modules. This is due to the fact that the current rating of PV modules based on this technology tends to be high enough to match the specifications of the designed MPPT converter without the need for parallel strings, while voltage levels are matched through multiple series-connected panels. However, this is not the case for thin-film technologies such as the CdTe module presented in Table 3.4. As previously stated, these PV modules display much higher voltages and lower currents delivered per module as compared to their silicon-based counterparts. Hence, a PV system based on thin-film materials interfacing with the designed MPPT converter will be arranged with multiple PV modules in parallel and a small number connected in series. This is verified through Table 3.4, where the mono-crystalline Si PV module already presents a suitable rated current, while the current rating of the CdTe module is considerably smaller. Conversely, when the rated voltage per panel of both representative modules is compared, the exemplar thin-film module presents a substantially higher voltage than the mono-crystalline silicon one.

Given that the electrical characteristics of a PV module vary considerably for each technology, so too will the overall PV system layout. Table 3.5 lists various optimal parameters regarding PV system layout for the two exemplary PV modules selected. The characteristics displayed are calculated in accordance to the converter specifications.

From Table 3.5, it becomes apparent that employing mono-crystalline silicon technology for a PV system used alongside the designed converter proves to be a more convenient solution, since these modules allow for a more flexible layout. The CdTe panels present such high open-circuit voltages that employing

Table 3.5: System layout characteristics for the two representative solar modules per converter input for the specified application.

Parameter (per PV array)	Mono-crystalline Si	CdTe
Modules in Series	9 modules	1 module
Parallel Strings	1 string	4 strings
Total Number of Modules	9 modules	4 modules
String V_{oc} at STC	375.8 V	222.9 V
String V_{mpp} at STC	314.9 V	188.8 V
Total I_{sc} at STC	10.54 A	10.36 A
Total I_{mpp} at STC	9.86 A	9.76 A
Nominal P_{max} at STC	3.10 kW	1.84 kW
Minimum Area Required	15.12 m^2	10.96 m^2

multiple of them in series results in a surpassing of maximum input voltage constraints, but using only one module per string results in an open-circuit voltage below the optimal value of 380 V, which limits power output. Moreover, the typical short-circuit current of mono-crystalline silicon is already close to the nominal current values of the converter.

Chapter 4

Testing and Results Analysis

Following the assembly of the designed MPPT converter, several tests were carried out in order to verify reliability of operation. This chapter describes the testing equipment available during the project, the tests performed, and the results derived from them.

4.1 Test Setup

The converter was assembled and tested in the laboratory of DC Opportunities in Delft. Figure 4.1 presents an overview of the testing equipment used for high voltage testing of the MPPT operation.

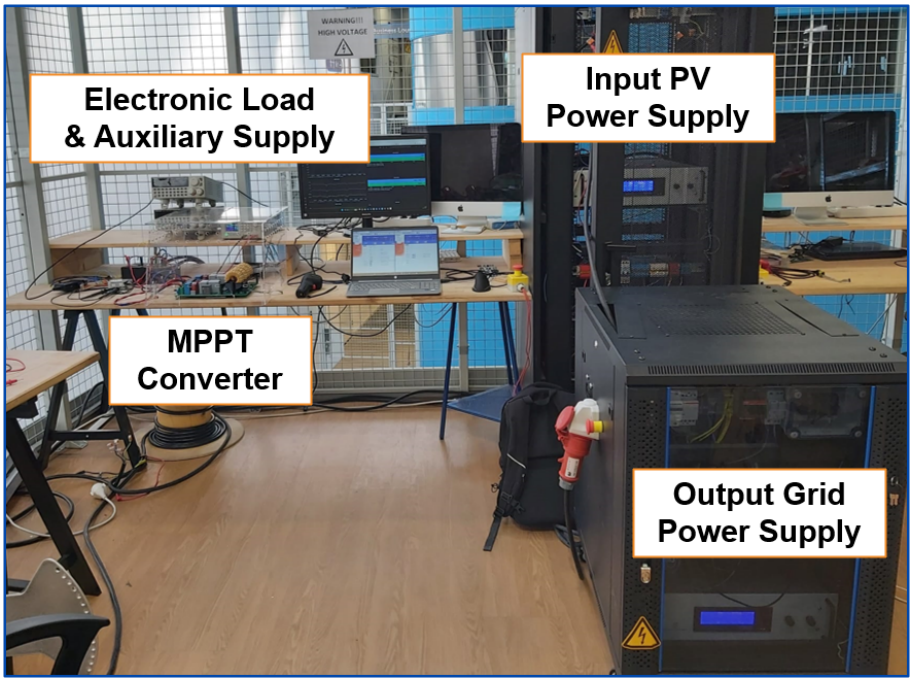

Figure 4.1: Laboratory test setup.

A 0-30 V DC power supply was used in order to supply 24 V to feed all of the micro-electronic devices present in the converter. Two different 15 kW DC bidirectional power supplies manufactured by Delta Elektronika were employed in order to feed an input PV voltage and output grid voltage to the converter. The power supply used as a PV input comes equipped with a photovoltaic system simulator function

that can accurately mimic the behaviour of a real PV system. This allows for proper testing of the MPPT operation. However, a testing limitation due to the equipment available lies in the fact that both of the sub-circuits that comprise the converter cannot be tested simultaneously under high power conditions due to an insufficient number of DC high power supplies. This is so since a total of four DC power supplies would be required in order to connect both PV inputs and their respective output poles. Nevertheless, both sub-circuits can be tested independently, since the operation of each converter side is independent from the other.

4.2 Gate Driving Test

The first steps towards ensuring the correct operation of the assembled converter concerns the testing of the SMD micro-electronic components. Once the voltage regulators, as well as the micro-controller, Wi-Fi module and multiple measurement circuits were checked for the main board, the aluminium PCBs were assessed.

The gate driver circuit of each of the half-bridges was tested as part of the evaluation of the aluminium PCBs. This was done by sending a representative PWM signal generated by the micro-controller to the input pin of the gate driver component of each board. This signal was measured both before and after passing through the gate driver circuit, in order to verify the correct operation for the driving of the GaN HEMTs. The resulting PWM waveform after the gate driver circuit is measured at the gate pin of the GaN HEMTs. The PWM signal generated by the micro-controller was set to an arbitrary duty cycle of 30%, for the selected operational frequency of 125 kHz. Figure 4.2 displays the obtained measurements of this generated signal and the output PWM delivered at the gate of the GaN HEMTs by the gate driver.

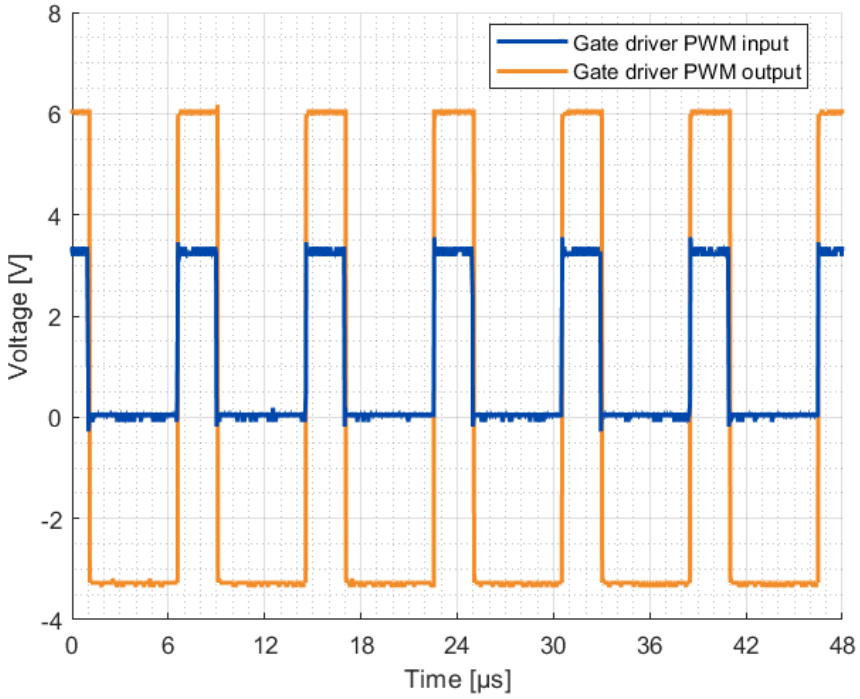

Figure 4.2: Measured PWM signals at the input and output pins of the gate driver.

From Figure 4.2, it can be seen that the PWM that is sent to the aluminium boards by the micro-controller showcases the correct frequency and duty cycle specified, and that the amplitude of this signal is of 3.3 V. This signal would be insufficient to guarantee a reliable operation of the GaN FETs if it was to be sent directly to the gate of these devices. However, this signal is received by the gate driver, and with the support of an isolated power supply, another PWM signal with the same frequency and duty

cycle but different amplitude is generated. Therefore, the PWM signal that is delivered to the gate is comparatively much more robust, as shown in Figure 4.2. This output PWM signal maintains the frequency and duty cycle of the original PWM, but the voltage of this signal ranges from 6 V to -3.3 V. These voltage levels clearly define the on and off-states for the GaN HEMTs in accordance with the gate voltage thresholds of these devices, and ensure that no accidental turn-on occurs due to the Miller effect as stated in subsection 3.4.3.

4.3 Positive Circuit Testing

Due to equipment limitations at the laboratory, the two independent sides of the converter could not be tested simultaneously. Instead, each sub-circuit was experimented with independently, connecting the two available DC high-power supplies to the corresponding input and output terminals.

In this section, the results for three tests performed on the positive sub-circuit (namely, the top sub-circuit in Figure 3.2, composed of PV_1 and connecting to the positive output pole) are presented. The first is a variable voltage test at low currents, carried out without a heat-sink, that serves as a baseline to demonstrate the MPPT operation of the converter and the difference in thermal performance between the usage and disuse of a heat-sink. The second one is a test at high voltage and high current, resulting in the maximum power output. This test is carried out with the implementation of the selected heat-sink that, in combination with the aluminium half-bridge PCBs, dissipates the heat caused by the losses derived from high current values flowing through the semiconductor devices. This test verifies the adequacy of thermal management in the converter design during maximum power conditions. Lastly, a third test at low voltage and equally high current is performed. Low voltages result in high GaN HEMT duty cycles, which in turn increases the losses and operational temperature of these devices. Hence, this final test proves acceptably low FET temperatures during thermally harsh ranges of operation for the converter.

Each of these tests is presented with data displaying measured input and output voltages, inductor currents and duty cycle as well as voltage and current set-points returned by the control algorithm implemented in the micro-controller. These results are extracted through the different measurement circuits designed. Additionally, an image captured with a thermal camera showcases the highest temperatures reached during converter operation for each test.

4.3.1 Low Current Test

The low current test aims to showcase MPPT operation at variable input voltages. For this purpose, no heat-sink is required when testing with low currents. Therefore, this test will also serve as a baseline for comparison regarding thermal management versus testing with all heat dissipation measures implemented.

The first power supply is connected to the positive-side PV input terminals and is set to mimic a PV array operation through a PV simulation function. The second power supply is connected to the positive pole grid output of the converter, and is set to maintain a grid voltage of 350 V. The control algorithm generates a voltage and current set-point depending on the measured voltage and current values, and employs these parameters to output a duty cycle value. The following Figure 4.3 displays the measured input and output voltages, as well as the voltage set-point and duty cycle of the FET control PWM signal generated by the micro-controller throughout the duration of this test. Furthermore, Figure 4.4 showcases the measured inductor currents for the positive sub-circuit, as well as the current set-point returned by the micro-controller.

As Figure 4.3 shows, the input voltage delivered by the PV simulation function is set to 100 V at MPPT and then raised to 300 V. While at 100 V, the duty cycle is kept at high values, and it falls as the input voltage rises, in accordance to the duty cycle expressions derived in Chapter 3. It can be seen that the input voltage closely follows the voltage set-point specified by the control algorithm. From Figure 4.4, it can be seen that the total PV simulator current is divided among the two interleaved phases of the positive side. This division of current is not completely equally distributed, since there are small differences in impedance in the main board for both phases. The set-point produced by the control algorithm is half of

Figure 4.3: PV simulator input, output and set-point voltage alongside duty cycle for the positive pole under nominal grid voltage and without a heat-sink.

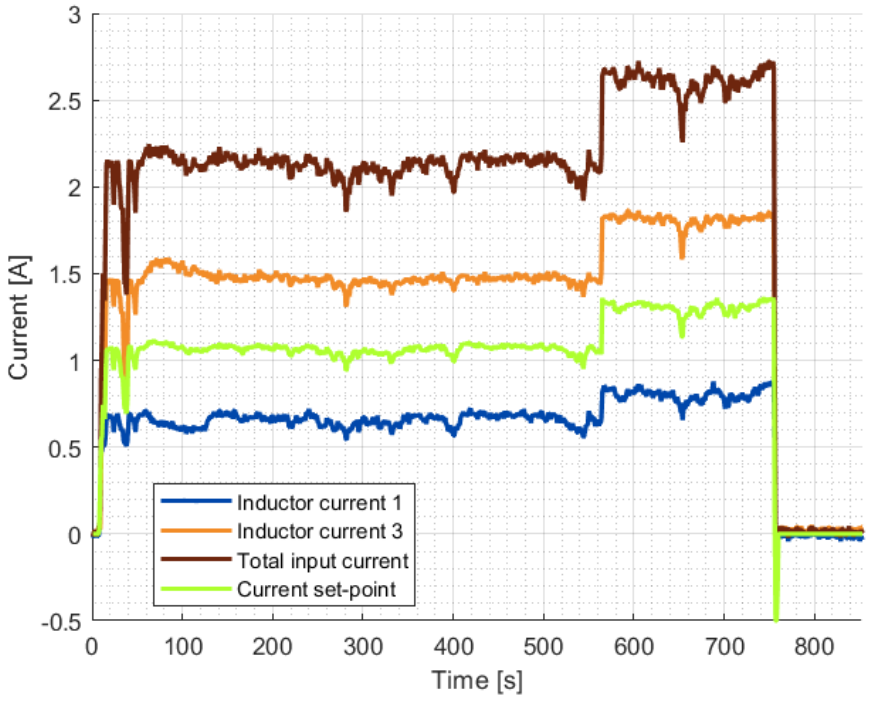

Figure 4.4: PV simulator input current, inductor currents and current set-point for the positive pole without a heat-sink.

the total input current. During this test, the MPPT current is raised from 2 A to 2.5 A in order to observe the set-point adaptation to this change.

While the MPPT operation of the positive sub-circuit is verified through these results, it is also relevant to observe the thermal performance of the converter without a heat-sink, in order to provide a valid comparison between this set-up when compared to future full power tests. Figure 4.5 displays the temperature of the GaN HEMT 1 alongside its corresponding duty cycle over the testing time. These temperature values were measured through the thermistor circuits designed. The subsequent Figure 4.6 validates these measurements by displaying a thermal image of the positive side of the converter captured during the testing.

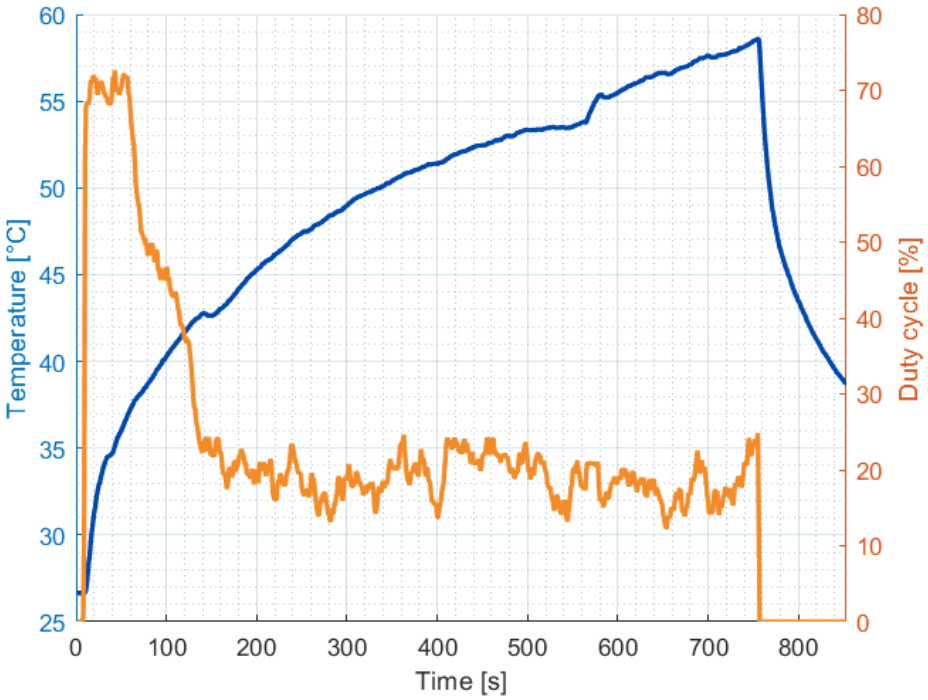

Figure 4.5: Measured temperature and duty cycle of GaN HEMT 1 without a heat-sink.

After observing Figure 4.5 and Figure 4.6, two main conclusions are apparent: first, it can be seen that, as expected, the temperature across the GaN HEMT rises substantially faster when its duty cycle is higher, and continues its growth at lower duty cycles albeit at a reduced pace. Secondly, it is evident that employing a heat-sink for thermal dissipation, in addition to the aluminium boards employed, is critical. This is so because this test was performed at current levels equal to 25% of the maximum rated current specified for the converter, and even so, the maximum temperature captured by the thermal camera is localized at one of the GaN HEMTs, and is equal to 61.8 °C. This value is safe for the switching operation, but is too high to guarantee that the GaN FET will not be damaged at maximum input current without proper thermal management. Hence, it is clear that a heat-sink is required for full power testing. Therefore, the following tests performed at high input current are carried out only with the addition of the heat-sink assembled in contact with the aluminium PCBs, as designed.

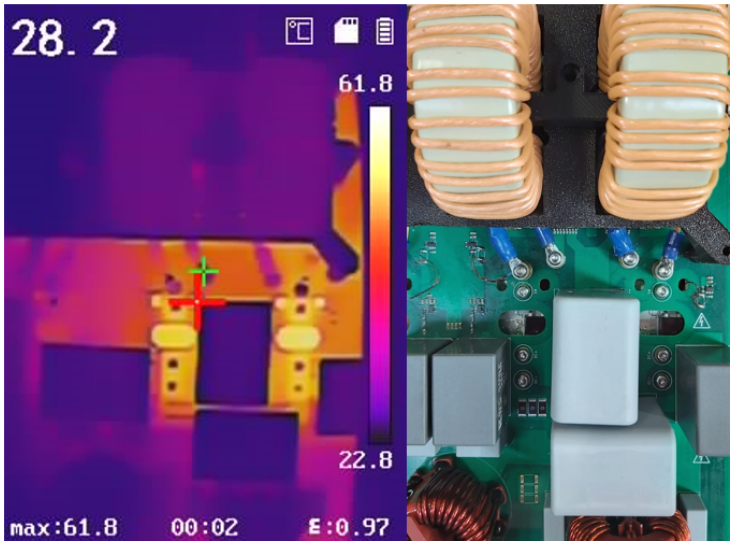

Figure 4.6: Thermal image of the converter at low current testing without a heat-sink (left) alongside the converter area pictured as reference (right).

4.3.2 High Voltage-High Current Test

The following test, performed at high voltage and high current, represents the operation of the converter at conditions close to its maximum power rating for a grid at 350 V per pole. For this test, the PV simulator function is adjusted to a MPPT voltage value of 300 V, and the current delivered by it is set to various increasing values up until 10 A. The selected aluminium heat-sink is attached to the converter. The purpose of this test is to ensure the safe high-power operation of the converter, and at the same time, prove that the thermal management measures implemented during the design are appropriate for high-power conditions. Figure 4.7 illustrates the input and output voltages measured over time during this test, as well as the resulting duty cycle of the PWM signal delivered to the gate of the GaN HEMTs. Likewise, Figure 4.8 displays the measured inductor current values for both interleaved phases, as well as the total input current and the current set-point provided by the control logic.

As evidenced by Figure 4.7 and Figure 4.8, the operation of the positive sub-circuit at high power is successfully verified. The control logic reacts appropriately when changing the current delivered by the PV simulator supply, and no issues are found at high voltage nor high currents. It can be seen that the input current is split relatively evenly among both interleaved phases, with close to half of the total current flowing per each inductor.

Furthermore, Figure 4.9 showcases a thermal image captured during testing at the highest current setting. The hottest point in the converter is localized at one of the GaN HEMTs, with a temperature equal to 63.7 °C. When compared to a similar image shown in Figure 4.6 for the low current testing, it can be seen that the captured GaN HEMT temperature values are approximately the same, even though, for the presently discussed test, the positive sub-circuit was tested at maximum rated current. This proves that the inclusion of the heat-sink, in combination with the use of aluminium PCBs, is sufficient and essential in order to keep the temperature of the GaN HEMTs well below their breakdown limit of 150 °C when under high power operation. In fact, going back to Figure 3.8, presented in subsection 3.3.2, it is observed that the simulated maximum temperature reached by a GaN HEMT of the selected model, under the same conditions as tested, is expected to be around 74 °C. This value is approximately 10 °C above the actual measured value. The simulated temperature values are higher due to the software constraints that prevented the proper simulation of the dissipation effect of the aluminium boards employed.

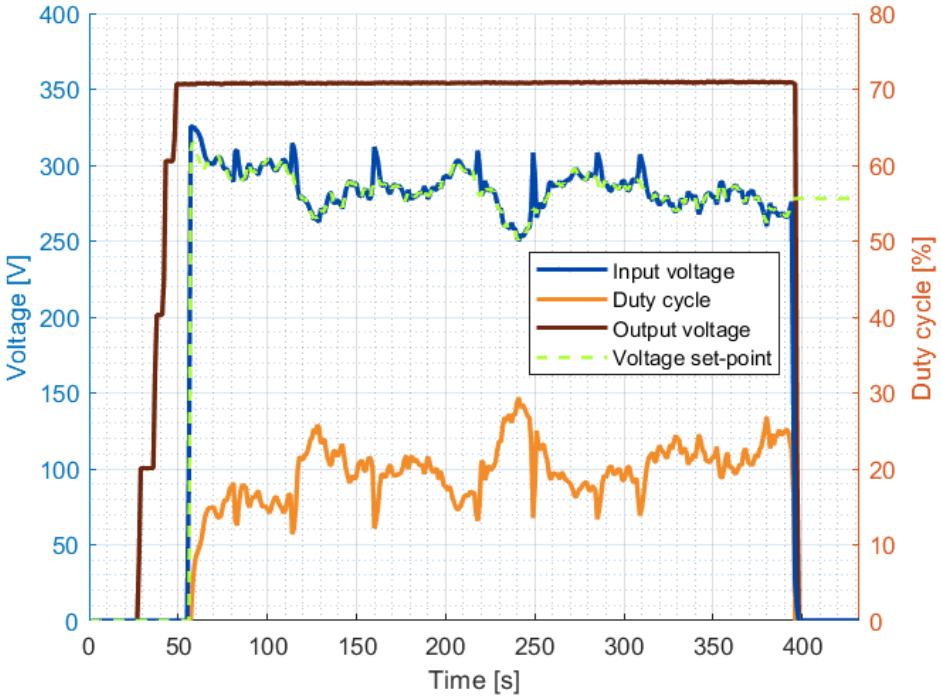

Figure 4.7: PV simulator input, output and set-point voltage alongside duty cycle for the positive pole maximum current test with a heat-sink.

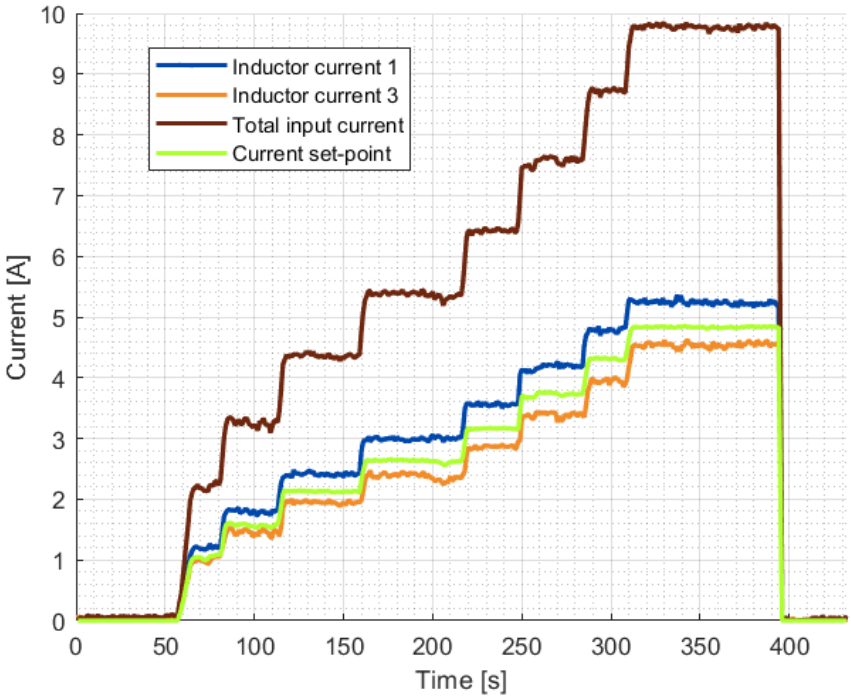

Figure 4.8: PV simulator input current, inductor currents and current set-point for the positive pole maximum current test with a heat-sink.

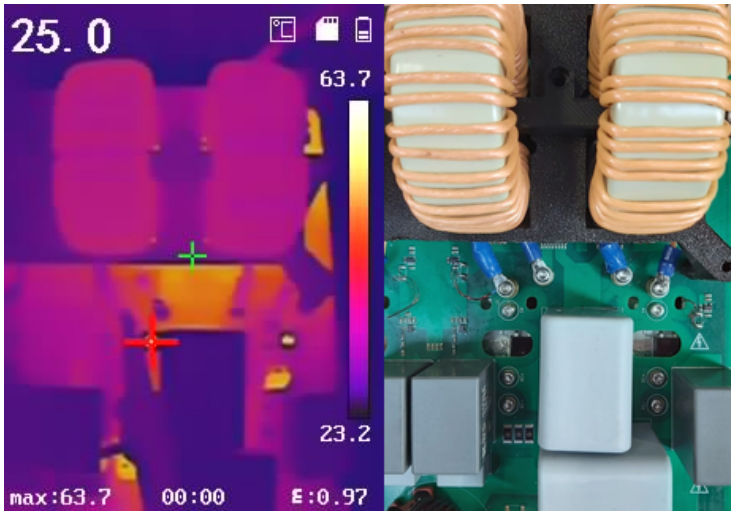

Figure 4.9: Thermal image of the converter at maximum current with a heat-sink (left) alongside the converter area pictured as reference (right).

4.3.3 Low Voltage-High Current Test

Lastly, the results of a low voltage and high current test for the positive sub-circuit are presented. The previous high voltage-high current test proved that the thermal management of the designed MPPT converter is adequate during high power conditions, and better than estimated with the thermal simulations performed. However, testing at the highest power ratings requires high input voltages, which in turn results in low duty cycles. Since the GaN HEMTs are the components more susceptible to reaching the highest temperatures, an additional high current test that produces higher duty cycles is required in order to confidently assess the efficacy of the thermal dissipation measures taken during the design of the MPPT converter. In order for the micro-controller to return higher duty cycles, a comparatively lower maximum power point input voltage is set to 200 V. Firstly, Figure 4.10 and Figure 4.11 display the measured parameters under which this test was carried out.

As presented in Figure 4.10 and Figure 4.11, this test was performed with a comparatively lower PV input voltage, which results in high duty cycle values. Similarly as done with the previous high current test, the current delivered by the PV simulator supply is raised gradually to the maximum specified rating of 10 A. It is to be noted that in this case, the control of the MPPT is not sufficiently robust and there is a transient decrease in current after 7 minutes of testing time while the control adjusts to the optimal current and voltage values. Under this higher duty cycle test, the captured thermal image of the positive side of the converter during the highest input current period is shown in Figure 4.12.

As evidenced by Figure 4.12, the highest measured temperature point, once again situated at the GaN HEMTs, is equal to 73 °C. This value is only approximately 10 °C higher than the value measured at the lower duty cycles of the high power test, and still lower than the simulated junction temperature value expected under the same input voltage conditions of around 200 V.

As an additional verification of the results obtained, Figure 4.13 displays a comparison between the PLECS simulated transistor drain-to-source voltage and the measured value for similar duty cycles.

In light of these results, it can be observed that the positive sub-circuit of the converter functions properly, reliably, and reacts in accordance to expectations when facing different external conditions. The control algorithm adjusts the duty cycle of the GaN FETs in consequence to the voltage values measured. Moreover, the thermal management implemented during the design phase in the form of aluminium PCBs and an appropriate aluminium heat-sink is more than sufficient to guarantee that the temperature of the semiconductors remains within safe values.

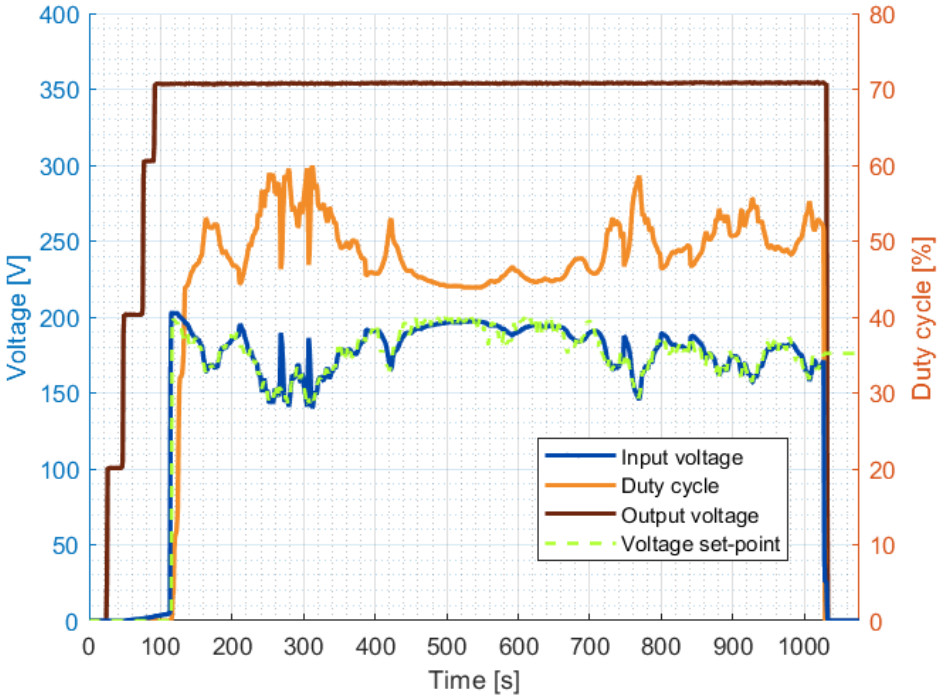

Figure 4.10: PV simulator input, output and set-point voltage alongside duty cycle for the positive pole maximum current test with a heat-sink and at a high duty cycle.

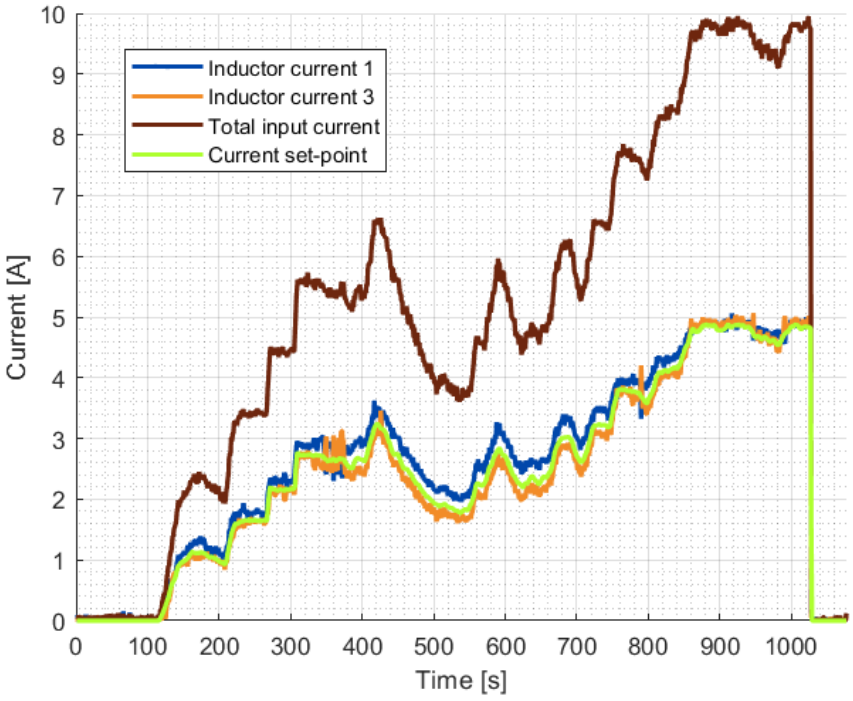

Figure 4.11: PV simulator input current, inductor currents and current set-point for the positive pole maximum current test with a heat-sink and at a high duty cycle.

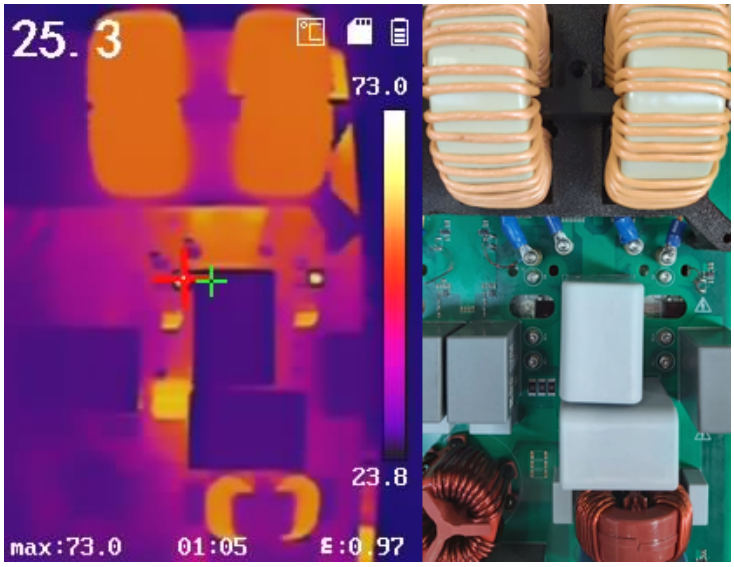

Figure 4.12: Thermal image of the converter at maximum current with a heat-sink and at a high duty cycle (left) alongside the converter area pictured as reference (right).

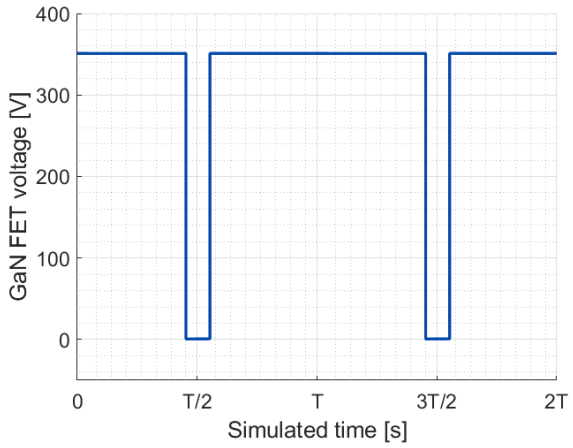

(a) Simulated GaN FET drain-to-source voltage.

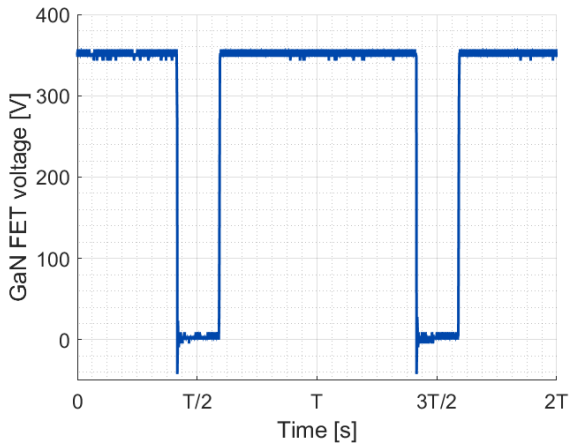

(b) Measured GaN FET drain-to-source voltage.

Figure 4.13: Comparison between the PLECs simulated and measured GaN FET drain-to-source voltage at high power conditions for similar duty cycles.

4.4 Negative Circuit Testing

Multiple tests were performed for the negative sub-circuit, leading to similar results and conclusions as for the positive sub-circuit, as expected.

However, a reliability issue was found only for the negative sub-circuit, and only under specific circumstances, that would cause one of the GaN HEMTs in the low half-bridges to breakdown. Unfortunately, this problem delayed the overall timeline of the project, since identifying and resolving the issue required a sizeable time investment. This made it unfeasible to test the converter with a real PV installation within schedule, as originally planned. In this section, the conditions under which the problem was found will be described, and the most probable cause for the effect that led to these drawbacks, as well as what can be done in order to prevent it from happening, will be explained.

The following Figure 4.14 presents the voltage and duty cycle data for one of the tests performed for the negative sub-circuit. In this test, the current per inductor is kept low at 2 A. The input voltage supplied by the PV simulator, as well as the grid output voltage set by the second power supply, are increased gradually and at a similar pace.

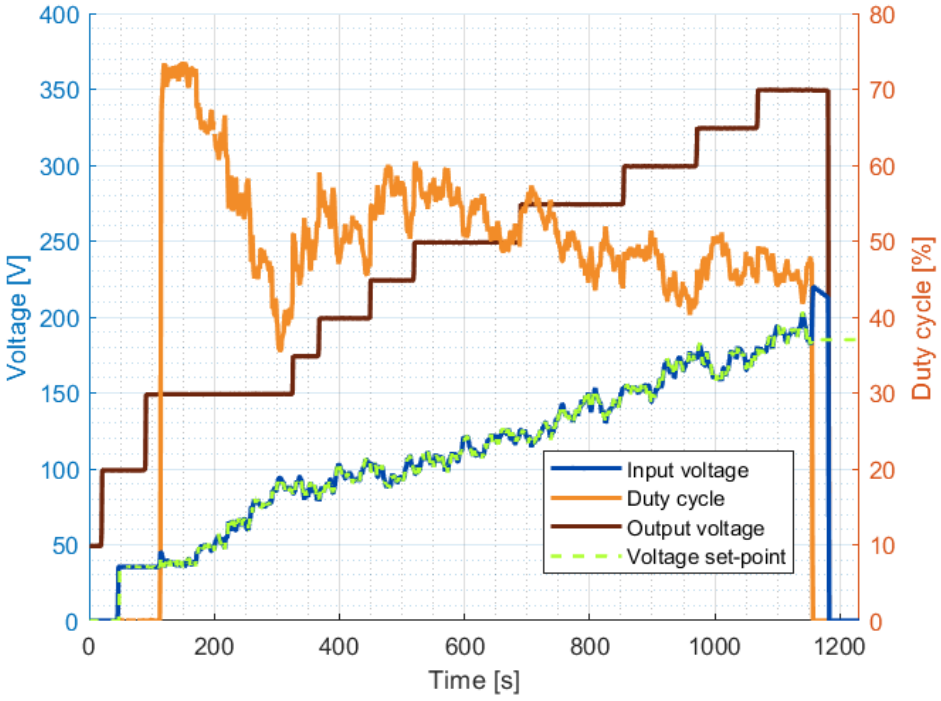

Figure 4.14: PV simulator input, output and set-point voltage alongside duty cycle for the negative pole test.

From Figure 4.14, it can be observed that the MPPT operation is normal throughout most of the test duration. However, towards the end of the test, when the output voltage reaches 350 V, there is one point at which the measured duty cycle is seen to suddenly collapse. At this point during testing, damage is caused to only one of the GaN HEMTs connected to the negative sub-circuit, and the control algorithm prevents further operation on the basis of detecting an over-current through one of the inductors. This occurs within a time frame too short for the Wi-Fi module to be fast enough to send any data on specific values measured at the precise moment. After visual inspection of the low half-bridge, it is clear that the GaN HEMT experiences a drastic energy spike that causes the transistor to blow up. Figure 4.15 showcases this half-bridge board, where it can be seen that the GaN HEMT (circled in orange) presents a crater on the surface of its encapsulation.

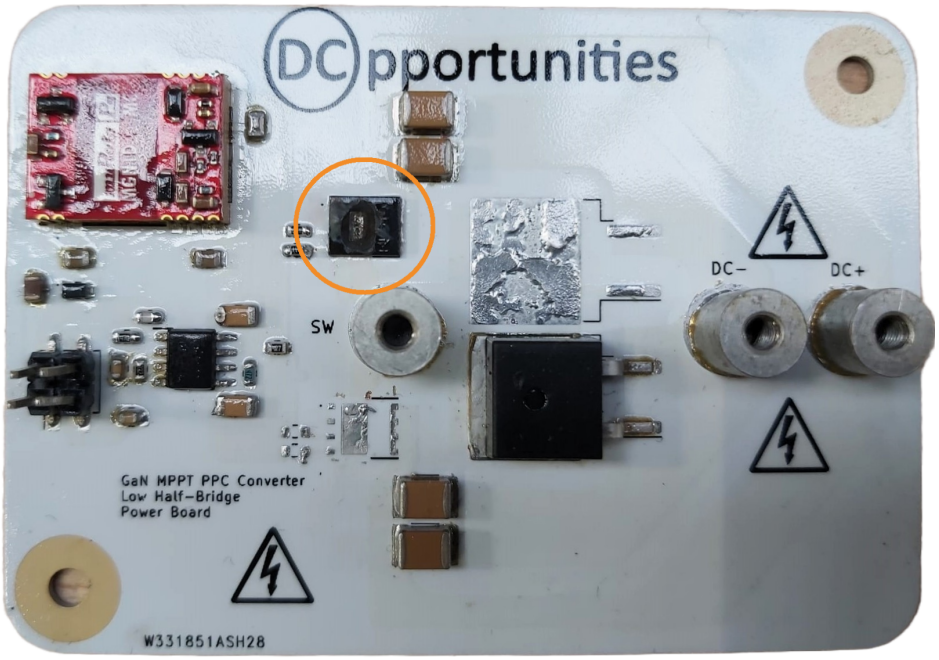

Figure 4.15: Damaged GaN HEMT in a low half-bridge after high voltage testing.

After careful inspection of each of the components in the aluminium low half-bridge, it is confirmed that only the GaN FET is damaged, and the rest of the components have not been affected during the destructive test.

After multiple tests, various suspected possible sources of this issue were discarded, such as possible violations of voltage clearances or problems caused by excessive noise, since the switching node of the low half-bridges is situated at the source of the FETs. The control algorithm was also suspected to be causing this issue, since repeating a hardware test with all parameters equal would sometimes result in damage, while others it would not, suggesting inconsistencies in MPPT control. Exhaustive testing eventually led to a proposed hypothesis behind the origin of the issue, which pertains to the inherent operation of the topology, rather than to the design of the converter.

In a boost converter, as described in section 3.1, the inductor is charged during on-operation and discharged across the load during the time that the transistor is switched off. Figure 4.16 displays the boost configuration during both of these states, with Figure 4.16a representing the circuit during on-state and Figure 4.16b depicting the same during off-state. The polarity of the voltages across the input source, inductor, diode and output is depicted accordingly in both diagrams.

It is to be noted from Figure 4.16 that the polarity of the inductor is reversed when transitioning from on to off-state, since the accumulated inductor charge is then discharged across the output, with the inductor behaving as a voltage source in series with the input supply. When an arbitrary load is connected to the output of the circuit, the output voltage is regulated through the relationship between duty cycle (d), input voltage (V_{in}) and output voltage (V_{out}), as presented in Equation 4.1.

$$V_{out} = \frac{V_{in}}{1 - d} \tag{4.1}$$

When a simple resistive load is present at the output, the converter will function normally at any duty cycle save from values very close to 100%. However, the testing carried out is not done through the use of resistive loads. Instead, a bidirectional DC power supply is connected to the output, which simulates

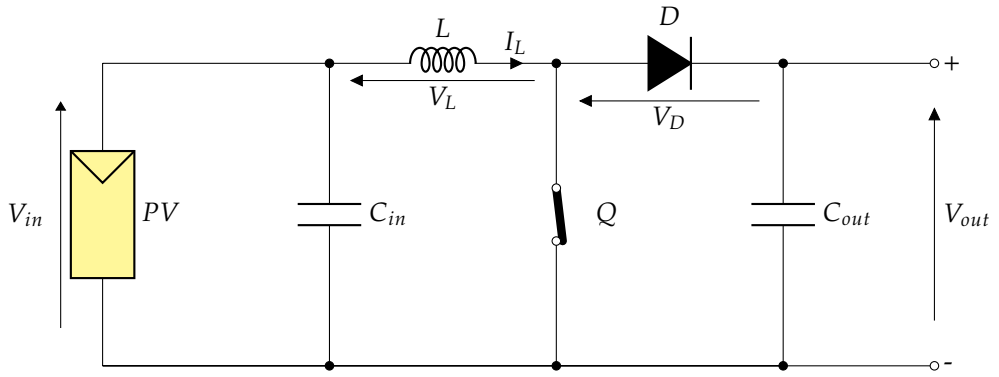

(a) Boost converter voltages during on-state.

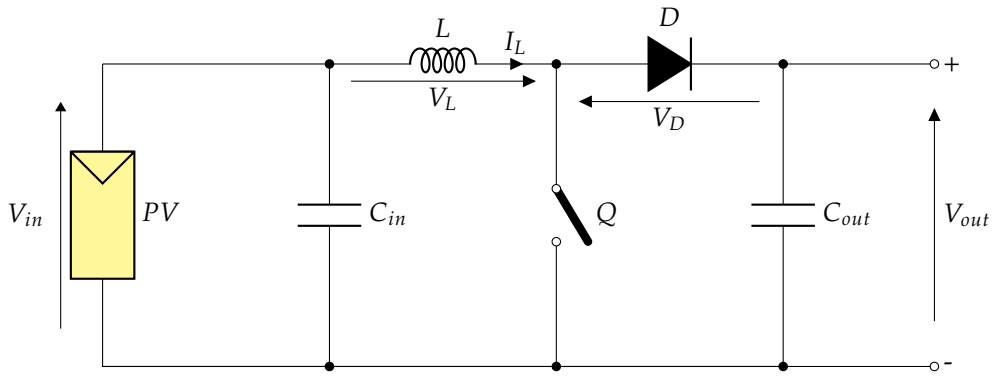

(b) Boost converter voltages during off-state.

Figure 4.16: Boost converter voltage polarities during on and off operation.

a constant DC grid voltage and behaves as a load in order to accept current delivered by the input PV source. This makes it so that, during testing, V_{out} has a set value. This is not an issue by itself: the converter operates normally by adjusting its duty cycle in accordance to this set output voltage value and the given input value provided by the PV simulator source.

Nevertheless, counting with a set output voltage at a high value can cause issues due to the turn-on requirements of the diode. In order for the diode to conduct, the voltage present at its anode must be higher than the voltage at the cathode. Hence, the anode-to-cathode voltage (V_D) must be positive for the diode to be forward biased. This voltage is always negative during on-state, as it should be, since the set output voltage forces the diode to be reverse biased. During off-state, the diode should always conduct current to guarantee normal step-up operation. However, if the output voltage V_{out} is at a high value, then a sufficiently low duty cycle during on-state could cause the inductor to not charge up to a voltage high enough so that the sum of input and inductor voltage during off-state surpasses the output voltage in magnitude. This prevents the diode from being forward biased, since in order for V_D to be positive during off-state, the following Equation 4.2 must be fulfilled.

$$V_{in} + V_L > V_{out} \tag{4.2}$$

If this condition is fulfilled during off-state, the inductor current (I_L) will flow through the diode and energy is therefore delivered at the output. However, should this condition not be fulfilled upon transitioning from on-state to off-state, then the inductor current will have no path to follow. Therefore, I_L is suddenly forced to go to zero from a non-zero value. In accordance to the definition of inductance, a change in inductor current in a very short period of time will result in an excessively large instantaneous voltage drop across the inductor, as stated in Equation 4.3.

$$V_L = L \cdot \frac{di}{dt} \tag{4.3}$$

The transistor is connected in parallel with both the input source and the inductor at all times. This means that the combination of input voltage and the extraordinarily high inductor voltage will be equal to the drain-to-source voltage of the FET. The GaN devices employed can sustain a maximum voltage of 650 V, which is easily surpassed by the sudden voltage spike. This leads to FET breakdown, which in turn causes the drain current to drastically increase during a short time frame, resulting in the detected over-current. Only the transistor in one of the interleaved phases is damaged when this occurs, since the breakdown of a transistor causes a short-circuit in parallel with the one in the other interleaved phase, preventing any harm to it.

It is to be noted that this phenomenon only occurs under very specific conditions, namely when the control algorithm produces a low enough duty cycle when a high voltage is present at the output. The fact that this issue only occurs in the negative sub-circuit could be explained if the negative side of the MPPT converter presents bigger resistive losses than the positive one. These resistive losses would create higher voltage drops, that contribute to the likelihood of this effect taking place at higher duty cycles than normal.

All in all, the issue found is suspected to be inherent to the operation of the boost topology under the testing conditions specified. However, it can be prevented by adapting the control algorithm. If the control logic were to be modified to limit the minimum duty cycle to a safe value that would be high enough in accordance to the measured input and output voltages, this incident would be avoided entirely. Additionally, the fact that the same testing parameters would sometimes result in a successful test and other times in GaN FET damage has now an explanation in the lack of robustness of the control logic employed, since the issue does not occur when the duty cycle fluctuations do not reach any low value that could prove troublesome.

Chapter 5

Performance and System-Level Implications of GaN vs. SiC FETs

The aim of this chapter is to display the strengths and benefits that employing GaN FETs has in the designed MPPT converter. To do this, a comparison between GaN and its closest competitive power semiconductor technology, SiC, is performed. This comparison starts by evaluating the differences based on performance characteristics, using simulations to support the analysis. Following this, a comparison on a system-level perspective is studied. Lastly, the advantages of employing GaN switching for the specific MPPT converter designed are considered.

5.1 Comparison Methodology

It is an established fact that, over the recent years, Si-based power semiconductor technology has reached its performance limits. As a result, new emerging technologies based on wide band-gap semiconductors are experimenting remarkable development. Both GaN and SiC, which have proven to be capable of surpassing traditional silicon, can be found among these state-of-the-art materials. However, these two materials are clearly distinct, and their differences make them better suited for different power applications.

In order to analyze the suitability of each semiconductor material for a variety of applications, and highlight the benefits of employing GaN FETs for the designed MPPT converter, a comparison must be carried out. The contrast between these two devices can be observed from various perspectives. Focusing on the electrical characteristics of each device showcases their differences in performance, and thus provide valuable insight into their strengths and weaknesses. Hence, two similar FETs based on each of these technologies are selected so as to compare the parameters of each device. Additionally, a comparison based on the application that is the focus of this work is carried out through simulations. This simulation validates the conclusions reached by way of comparing electrical characteristics.

Moreover, GaN and SiC can also be compared considering a system-wide approach, taking into account factors unrelated to electrical performance. Consequently, the same selected FETs are also analyzed from this perspective, so as to provide additional relevant context to the overall comparison.

5.2 Performance Analysis

Even though both are wide-bandgap semiconductor materials, GaN and SiC are materials with very different physical characteristics, as it was established in section 2.3. These properties are translated into different electrical parameters when it comes to power semiconductors built out of these materials.

In this section, the extent to which these materials behave differently from an electrical and thermal performance point-of-view is explored.

The following Table 5.1 displays a parametric performance comparison between a pair of GaN and SiC FETs of identical blocking voltage and comparable rated drain current. On one hand, the GaN HEMT selected is the GS-065-011-1-L, manufactured by GaN Systems. This is the same GaN FET employed for the designed MPPT converter. On the other hand, the chosen SiC MOSFET is the C3M0120065L, by Wolfspeed. Both of these FETs are encased in SMD packaging, in order for this comparison to be more equitable. The parameters presented were gathered from the corresponding datasheet of each component.

Table 5.1: Performance comparison between GaN GS-065-011-1-L vs. SiC C3M0120065L.

Parameter	Symbol	GaN HEMT	SiC MOSFET
Drain-to-Source Voltage	V_{ds}	650 V	650 V
Rated Current	I_d	11 A	21 A
On-resistance at 25 °C	$R_{ds(on)}$	150 mΩ	120 mΩ
On-resistance at 150 °C	$R_{ds(on)}$	380 mΩ	168 mΩ
Gate Charge	Q_g	2.2 nC	26 nC
Input Capacitance	C_{iss}	70 pF	640 pF
Output Capacitance	C_{oss}	20 pF	45 pF
Output Capacitance Stored Energy	E_{oss}	2.4 µJ	9 µJ
Turn-on Switching Energy	E_{on}	20 µJ	27 µJ
Turn-off Switching Energy	E_{off}	5.8 µJ	7 µJ
Thermal Resistance Junction-to-Case	$R_{\theta JC}$	1.4 °C/W	1.38 °C/W

The data depicted in Table 5.1 yields clear conclusions as to what the difference in performance between GaN and SiC is. First of all, it can be seen that the SiC MOSFET is rated for a higher current, and although the $R_{ds(on)}$ of both devices is relatively similar, the on-resistance of SiC quickly outclasses the one presented by GaN at very high temperatures. This is testament to how SiC is able to maintain homogeneous conduction losses despite changes in temperature, due to its thermal conductivity.

Nevertheless, GaN gains the upper hand when it comes to switching losses. The switching behaviour of a FET greatly relies on the value of its gate charge, as well as the input and output capacitance. Firstly, the gate charge value represents the amount of charge that needs to be fed to the FET to activate it. The lower it is, the less energy is required for switching. Secondly, the input capacitance is charged during turn-on through the gate current received. Thus, the smaller this value, the faster the switching speed. Lastly, the output capacitance will release current after the gate is turn-off. Hence, the time it takes for the FET to completely turn-off is longer the bigger this capacitance value. The output capacitance stored energy is the amount of energy that will be released, and therefore wasted, during this process. It is also worth noting that these capacitance values remain fairly impervious to temperature variation [35]. It can be seen that all of these values are considerably lower for GaN. Thereby, the switching losses of the GaN HEMT will be substantially lower. This also allows GaN devices to work at considerably higher switching speeds compared to SiC. GaN is therefore ideally suited for applications at high frequency-low load applications where conduction losses are not dominant.

All in all, it can be concluded that the switching efficiency of GaN is superior to SiC, yielding lower losses. On the other hand, losses caused by conduction are reduced through the use of SiC. Therefore, it can be said that GaN is the best option for applications with high frequencies of operation, since switching losses will be minimized, while SiC is preferable for thermally intensive power applications, where high temperatures and currents are a major concern.

However, the drawbacks that employing GaN technology yields can be circumvented through paralleling. In applications where conduction losses are dominant due to high current levels, paralleling two identical FETs makes it so that the current flowing through each device is split in two. Since conduction

loss is dependent on the square of the current, the overall conduction losses decrease. Additionally, paralleling reduces the temperature increase of the FET. This can be very beneficial to GaN, since, as stated earlier, the $R_{ds(on)}$ for GaN has a higher dependency on temperature. Even though the disadvantages of GaN can be dealt with, SiC, on the other hand, has no reliable way to decrease switching losses in hard-switching applications, since paralleling devices does not result in less switching loss.

Therefore, from a performance point-of-view, parallel GaN design offers the best that both technologies have to offer, although design complexity can increase from a top-level view. To summarize this comparison in component performance:

- The switching operation of GaN is faster and more efficient.
- Rises in conduction losses as a function of temperature are smoother for SiC.
- Paralleling GaN devices decreases conduction losses, while SiC has no way to reduce switching losses without decreasing operational frequency.

In order to get a complete picture of the differences between GaN and SiC for the specific application of the designed MPPT converter, the use of both technologies for the interleaved configuration was simulated in PLECS, maintaining all other parameters equal. Therefore, all specifications from Table 3.1 remain the same for these simulations. The selected FETs simulated are the same as the ones compared in Table 5.1. An accurate thermal description of both FETs was downloaded directly from the website of the corresponding manufacturer. The comparison was carried out under steady-state conditions and high power operation (3.2 kW of power conversion per pole), considering an ambient temperature of 50 °C. The generated FET losses data that resulted from these simulations is displayed in Table 5.2.

Table 5.2: Steady-state simulated performance of GaN GS-065-011-1-L and SiC C3M0120065L FETs for the designed interleaved MPPT converter application at high power operation.

Parameter (per device)	GaN HEMT	SiC MOSFET
Conduction Losses	0.5357 W	0.3076 W
Switching Losses	1.3877 W	2.3755 W
Total Losses	1.9266 W	2.6831 W
Junction Temperature	73.31 °C	78.47 °C

The previous conclusions have been verified through these simulations. As expected, the conduction losses of the SiC MOSFET are lower than for the GaN HEMT, but the switching losses of SiC are substantially higher than the ones presented by GaN. However, for this application, the conduction losses of SiC are only 0.228 W less than for GaN. Meanwhile, the switching loss produced by the GaN device are 0.988 W lower than those originating from the SiC MOSFET. This results in a lower junction temperature over the GaN HEMTs selected, which is 5 °C lower than the temperature of the SiC devices.

Hence, under the simulated conditions, and for the given application, GaN FETs can preferable, despite the fact that both technologies showcase acceptable performances.

5.3 System-Level Comparison

An in-depth comparison between GaN and SiC must not be limited to a contrast in performance characteristics of these devices. In order to take all decision variables into account, a system-level comparison must also be considered. Employing GaN or SiC can have a significant and decisive impact on the overall design of a system, going beyond differences in performance. Hence, the criteria that can influence design on a system-wide scale will be explored.

One of the practical limitations that engineers face when developing new design has to do with budget constraints. When comparing GaN-based FETs to SiC ones, a significant difference can be found in

component cost. GaN devices are inherently cheaper than SiC. As an example, the price per unit for orders bigger than a thousand components of the devices compared in Table 5.1 is €2.09 for the GaN HEMT and €4.18 for the SiC MOSFET shown. Even though both FETs are rated for similar applications, the SiC FET is twice the price of the GaN one. A price difference of this caliber extends to most comparable GaN and SiC devices that exist currently in the market. Furthermore, as established by the analysis presented in section 5.2, the drawbacks that using GaN FETs presents can be circumvented through the use of parallel switches. Under these conditions, GaN outperforms SiC, regardless of whether the SiC switch is paralleled or not. Naturally, paralleling devices doubles the amount of switches needed, and hence FET costs are also doubled. Although this may seem like a major downside, the low price of GaN when compared to SiC allows for the use of parallel GaN configurations, and all the advantages that this provides, at no extra cost when compared to a SiC solution. Thus, a GaN-based design can be scaled up for high power applications and higher rated currents with a relatively low impact on overall system cost.

Another relevant factor that warrants careful consideration during electrical system design is power density. Power density is defined as the ratio of power processed by an electric device compared to its volume or weight. Often times, the application for which the system is designed sets specific constraints to size and weight that must be complied with. Furthermore, even if these constraints are not rigorous, size and weight will always impact overall cost. Thus, an optimal design must prioritize high power density.

From this point-of-view, the influence on overall size caused by the semiconductor material chosen for FET devices can be substantial in various ways. The first and most direct of these concerns the size of the FET devices themselves. GaN HEMTs are generally confined in smaller packages than equivalent SiC MOSFETs. This is due to the lateral structure of GaN FETs presenting shorter distances between source and drain [36]. Figure 5.1 illustrates the typical structure diagram of a GaN HEMT compared to that of a SiC MOSFET.

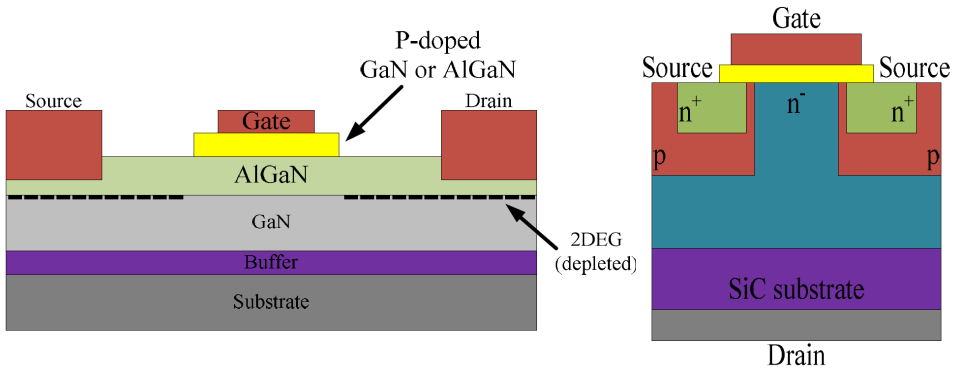

Figure 5.1: Structure diagrams of a lateral GaN HEMT (left) and a vertical SiC MOSFET (right) [37].

As previously stated, the lateral internal layout of a GaN HEMT is more advantageous from an overall size perspective compared to the vertical structure of a SiC MOSFET, where current travels from source to drain through longer paths. To further illustrate this, the package dimensions of the previously compared FETs can be contrasted with each other. On the one hand, the GaN HEMT is encapsulated in a 5 mm × 6 mm × 0.85 mm SMD case. Figure 5.2 illustrates the size of this device by taking a euro coin as reference. On the other hand, the SiC MOSFET is integrated within a 9.9 mm × 10 mm × 2.3 mm SMD package. It can be noted that the height of the SiC MOSFET is almost three times larger than the height of the GaN HEMT, further demonstrating the depicted difference in structure of the two devices. Moreover, the GaN transistor is smaller in both length and width too. Overall, the volume of the selected SiC FET is close to nine times bigger than that of the comparable GaN FET. This significant difference in volume can cause substantial impact in a design, be it due to PCB area constraints or due to increased costs derived from overall converter size.

The second way in which the selection of a semiconductor material for transistors can affect power density

Figure 5.2: Size comparison between a GaN HEMT and a euro coin.

relates to the switching frequencies at which a given device can operate. Employing high switching frequencies directly results in smaller passive components. When operating at high frequencies, the inductor current ripple and capacitor voltage ripple are reduced, since the charging and discharging stages of these components will be shorter at high frequencies. This means that, for the same ripple values, smaller inductances and capacitances can be used at higher frequencies. The inductor current ripple expressions calculated for the designed MPPT converter shown in Equation 3.1 and Equation 3.2 serve as an example of this phenomenon. Therefore, an increase of frequency by a factor k allows for a decrease in inductance or capacitance value by a factor $\frac{1}{k}$. Thus, the size and cost of all passive components present in the design is significantly reduced. From a system-level perspective, it can be concluded that employing transistors that allow higher switching frequencies of operation results in devices with high power densities and superior cost-effectiveness. As presented in section 5.2 through parametric and simulated analysis, GaN-based FETs can be used at much higher frequencies without compromising efficiency, due to the fact that this semiconductor material counts with a high electron mobility and low parasitic capacitances.

5.4 Benefits of GaN for the Designed MPPT Converter

In light of the comparison between FETs based on gallium nitride as opposed to silicon carbide, the benefits of using gallium nitride for the designed MPPT converter can be further explored.

First of all, the use of GaN HEMTs allows for a higher frequency of operation that would greatly impact efficiency with a SiC-based design. This frequency rise results in smaller passive components, and therefore, the inductors used do not need to be bigger than the chosen size in order to maintain current ripple at a similar value. The same applies to capacitors, that can preserve an equally small voltage ripple at reduced sizes. This is outstandingly relevant for the designed converter, since a substantial area in the main board is occupied by the three EMI filters integrated, which are composed of capacitors and inductor chokes, in addition to the inductors required for boost converter operation. This increases the power density of the converter over a design that relies on silicon carbide without sacrificing overall efficiency in the process. Moreover, total converter cost is reduced since the chosen capacitors and chokes are cheaper than those that would be required at lower frequencies of operation.

Secondly, GaN FETs are less expensive than their SiC-based counterparts. Not only is this a clear advantage on its own, but the reduced component cost also offsets the monetary drawbacks of interleaving, which increases the number of devices used in exchange for better converter performance. Additionally, interleaving GaN devices for the selected application is comparatively more beneficial than doing so with SiC. This is due to the fact that paralleling power semiconductor devices yields diminishing returns in designs where the switching losses are a main concern due to high operational frequencies, such as the one proposed in this project. Total conduction losses can be halved through interleaving, but if SiC FETs were to be used, the switching losses would quickly become the dominant loss mechanism, and interleaving would therefore be less effective in increasing efficiency as compared to GaN.

Lastly, the compact size of the selected GaN HEMTs allows the aluminium PCBs that contain them

to present reduced dimensions, which not only decreases cost, but also enables the placement of all aluminium PCBs below the main board in a non-obstructive position that fits within the boundaries set by the proportions of the selected heat-sink and the main PCB itself. This is of the utmost relevancy, since the size of the aluminium PCBs needed to be as small as possible in order to accomplish this, while at the same time all voltage clearances and minimum track widths required during the design phase of the aluminium PCBs needed to be respected.

Chapter 6

Conclusion

The goal of this chapter is to provide a summary of the conclusions reached throughout the work performed. In order to do so, an answer is given to the research questions posed in Chapter 1. Lastly, recommendations are given for improvement in future designs, as well as a number of suggestions on future research opportunities related to the topics explored in this thesis.

6.1 Answering the Research Questions

1. How can a DC-DC MPPT converter based on gallium nitride switching be designed in a way that is suitable for bipolar DC grids?

In this thesis, a design for an MPPT DC-DC converter for bipolar DC grids based on gallium nitride switching is presented. This design is validated through the manufacture and testing of the proposed converter. The converter topology is divided into two distinct and independent sub-circuits that, when combined, interface naturally with a bipolar DC grid through the combination of both individual output poles.

By designing the converter in a topology with two sub-divisions, not only is bipolar grid integration simpler, but also two different PV arrays can be connected at once with only one MPPT DC-DC converter. The independent operation of both sub-circuit makes it so that two different MPPT algorithms could be implemented in the case that the system parameters of both PV arrays used were substantially different.

In order to guarantee safe and efficient operation of the proposed converter, thermal losses are managed through the use of a heat-sink in combination with single-layer aluminium PCBs that dissipate the heat generated by the GaN HEMTs and the diodes that comprise the half-bridges that carry out MPPT operation. Multiple aluminium boards are employed for this purpose, in order to increase the modularity of the design.

2. How do gallium nitride switches compare to other alternative solutions?

Both gallium nitride and silicon carbide stand out among the wide-band gap semiconductor technologies currently available for electronic switching applications. Silicon carbide transistors outperform gallium nitride ones when it comes to conduction losses. However, gallium nitride switches display substantially lower switching losses, which allows for higher frequencies of operation, reducing the size and cost of the passive components required.

For a topology that operates on hard switching conditions at high frequency, such as the one proposed in this thesis, employing GaN transistor devices that minimize switching loss can be more beneficial than using SiC. This is especially relevant when considering that fact that the lower price of GaN HEMTs

compared to SiC MOSFETs allows for paralleling or interleaving GaN devices while keeping the cost of semiconductors equal, which brings the overall FET conduction losses to a level that is on par with SiC. Additionally, the compact volume of GaN HEMTs provides another advantage in applications where size constraints play a critical role in converter design. This is the case with the aluminium boards designed for the proposed MPPT converter, since these PCBs needed to be as small as possible in order to fit below the main board of the converter.

However it must be noted that GaN switching is not without limitations. For applications that deal with very high power ratings, where large currents circulate through FETs, the low on-resistances of SiC could prove more advantageous than the benefits that GaN enables. This is especially relevant in soft-switching circuits, where switching losses can be almost neglected due to zero-voltage switching techniques [38]. Additionally, paralleling multiple GaN semiconductors could prove cumbersome in some converter designs, since special care needs to be given to symmetry in copper traces and component placement in order to evenly split the current that flows through parallel devices [39]. Lastly, in some specific cases, GaN implementation could be hindered by an increment in resonant frequency due to the reduction in capacitance and inductance that GaN enables. Nonetheless, this is not likely to cause issues, since the operational frequency of the converter is typically high enough in GaN-based designs to surpass the increment in resonant frequency.

3. What are the factors that affect the operation of this converter, and how does the operation range impact efficiency?

The efficiency of the proposed converter is affected mainly by two factors: the input voltage for which the PV arrays are sized, and the irradiance that these are exposed to.

A higher irradiance over the PV systems results in higher input currents. At higher input currents, the efficiency of the converter slightly decreases due to the effect of conduction losses increasing exponentially with inductor current, although the difference in performance in negligible for input currents below the rated 10 A. At very low input currents however, the efficiency of the converter can be reduced significantly, due to the effect of inductor core losses remaining constant even at low power conditions. Hence, at low power, the inductor losses represent a larger percentage of total losses when compared to high power conditions.

Despite this, the most impactful parameter affecting converter efficiency is the input voltage provided by the PV arrays, and to a lesser extent, the voltage present across the poles of the bipolar grid. These measured voltage values have a direct effect on the duty cycle of the GaN HEMTs, with higher duty cycles leading overall higher losses, despite diode conduction losses decreasing at higher duty cycles. The output voltage does not drastically affect the duty cycle of operation since the range of operation assumes that the potential difference between conductors of the bipolar DC grid will remain within 320 V to 380 V per pole. The set specifications of the converter limit the minimum input voltage to a value of 100 V in order to prevent operation at very high duty cycles that could result in excessive losses and low processed power. It must be noted that changes in environmental temperature would affect the overall efficiency of the converter too, since high temperatures would cause the PV systems to operate at lower voltages.

6.2 Recommendations and Future Work

There are multiple improvements that could be made in future iterations of the presented MPPT design, as well as more steps that could be taken to expand on the conclusions reached. In addition, more research can be carried out regarding different topics surrounding this work. This section lists some of these recommendations and future research opportunities:

1. Testing with a real PV installation and DC grid.

Due to lack of time, it was not possible to test the proposed converter with a real PV system and bipolar DC grid. Performing outdoors testing would provide more insight on the response of the MPPT

operation over a wide range of environmental conditions.

2. Resolve reliability issue in negative sub-circuit.

A probable cause behind the issue found during testing of the negative sub-circuit is given in Chapter 4. The explanation presented is based on multiple experiments carried out, but the specific reason why this effect only occurs on the negative sub-circuit has not been proved, although a possible one is suggested earlier in this work. Further testing is required to prove this, and once the issue is identified with certainty, it can be resolved. At the current moment, preventing the control algorithm from returning very low duty cycles at high output voltages seems to bypass the problem entirely, supporting the hypothesis presented in Chapter 4. However other issues could be causing this effect, such as inconsistencies with the control algorithm.

3. Empirical efficiency measurement.

The efficiency analysis carried out was effectuated through simulations. Due to time constraints, an empirical analysis of measured efficiency for the assembled MPPT converter was not carried out, since counting with a heat-sink is crucial in order to perform such an analysis, which unfortunately was only available towards the end of the project.

4. Iteration on EMI filter design.

As specified in Chapter 3, it is common for EMI filter designs to be iterative, where an initial estimate is made based on basic calculations, since accurately simulating expected EMI is not often feasible. For this reason, measuring the electromagnetic interference caused by the assembled converter is required in order to better adapt future EMI filter designs.

5. Development of a refined control algorithm.

The MPPT control algorithm employed during testing of the proposed converter relied on a basic implementation of a P&O algorithm that lacked proper tuning to better adapt to the hardware of the assembled converter. Moreover, additional safety features are needed, such as one that prevents the negative side from malfunctioning, as described in Chapter 4. More research can be performed in order to develop a more advanced control algorithm that is robust, fast, and adaptable to environmental changes.

6. Integration of zero-voltage switching techniques.

In order to further minimize power conversion losses, zero-voltage switching techniques can be implemented to future designs in order to achieve soft switching conditions. This would significantly improve efficiency by greatly reducing switching losses, which would also allow for even higher frequencies of operation.

7. Exploration of alternative topologies.

Additional research can be done regarding circuit topology as an alternative to the one proposed. Different topologies could present other advantages compared to the topology employed, including the possibility of enabling zero-voltage switching, as previously stated.

8. Research on GaN diodes.

Currently GaN is a widely used semiconductor material for power electronic switching, but despite its use in the manufacturing of transistors, this material is not typically employed in other power electronic components, such as diodes. Research on GaN diodes is currently ongoing [40], and a breakthrough in the development of this technology could open up the possibility for extensive new research regarding this topic.

Bibliography

[1] IEA, "World Energy Outlook 2022," 2022. [Online]. Available: https://www.iea.org/reports/world-energy-outlook-2022.

[2] IEA, "Electricity Market Report 2023," 2023. [Online]. Available: https://www.iea.org/reports/electricity-market-report-2023.

[3] W. Hemetsberger, M. Schmela, G. Chianetta and R. Sauaia, *Global Market Outlook for Solar Power 2022-2026*. SolarPower Europe, 2022. [Online]. Available: https://www.solarpowereurope.org/insights/market-outlooks/global-market-outlook-for-solar-power-2022.

[4] V. Benda and L. Černá, "PV cells and modules – State of the art, limits and trends," *Heliyon*, vol. 6, no. 12, e05666, 2020, ISSN: 2405-8440. DOI: https://doi.org/10.1016/j.heliyon.2020.e05666. [Online]. Available: https://www.sciencedirect.com/science/article/pii/S2405844020325093.

[5] International Energy Agency. "Solar PV." (2022), [Online]. Available: https://www.iea.org/reports/solar-pv (visited on 17/11/2022).

[6] Fraunhofer Institute for Solar Energy Systems, ISE. "Photovoltaics Report." (2022), [Online]. Available: https://www.ise.fraunhofer.de/content/dam/ise/de/documents/publications/studies/Photovoltaics-Report.pdf (visited on 17/11/2022).

[7] C. Balasubrahmanyam and O. Gupta, "Detailed Study of Solar Energy Conversion System using Boost Converter—a New MPPT Technique," *Journal of The Institution of Engineers (India): Series B*, vol. 101, pp. 631–639, Aug. 2020. DOI: 10.1007/s40031-020-00478-1.

[8] N. Mohan, T. Undeland and W. Robbins, *Power Electronics: Converters, Applications, and Design* (Power Electronics: Converters, Applications, and Design). John Wiley & Sons, 2003, ISBN: 9788126510900.

[9] V. Kumar and M. Singh, "Derated Mode of Power Generation in PV System Using Modified Perturb and Observe MPPT Algorithm," *Journal of Modern Power Systems and Clean Energy*, vol. 9, pp. 1183–1192, Sep. 2021. DOI: 10.35833/MPCE.2019.000258.

[10] G. Meneghesso, M. Meneghini and E. Zanoni, *Gallium Nitride-enabled High Frequency and High Efficiency Power Conversion*, A. P. Chandrakasan, Ed. Springer International Publishing AG, Jan. 2018, ISBN: 978-3-319-77993-5. DOI: 10.1007/978-3-319-77994-2.

[11] J. Xu, "Analysis of GaN Selection and Discomfort for LLC Resonant Converter," in *2020 IEEE 3rd International Conference on Information Systems and Computer Aided Education (ICISCAE)*, 2020, pp. 619–621. DOI: 10.1109/ICISCAE51034.2020.9236803.

[12] A. Lidow, M. de Rooij, J. Strydom, D. Reusch and J. Glaser, *GaN Transistors for Efficient Power Conversion*. John Wiley & Sons Ltd, 2015, ISBN: 9781118844779. DOI: 10.1002/9781119594406.

[13] Y. S. Park, *SiC Materials and Devices*, R. K. Willardson and E. Weber, Eds. Academic Press, 1998, ISBN: 9780080864501.

[14] S. Oliver and D. Kinzer, "The GaN Revolution in Fast Charging & Power Conversion," Jan. 2021. [Online]. Available: https://navitassemi.com/the-gan-revolution-in-fast-charging-power-conversion/ (visited on 18/11/2022).

[15] P. Murugapandiyan, V. R. Lakshmi, N. Ramkumar, P. Eswaran and M. Wasim, "GaN-Based High-Electron Mobility Transistors for High-Power and High-Frequency Application: A Review," in *Innovations in Electronics and Communication Engineering*, H. S. Saini, R. K. Singh, M. Tariq Beg and J. S. Sahambi, Eds., Singapore: Springer Singapore, 2020, pp. 339–348, ISBN: 978-981-15-3172-9. DOI: 10.1007/978-981-15-3172-9.

[16] K. Shenai, "High-frequency switching limitations in Gallium Nitride (GaN) and Silicon Carbide (SiC) power devices for boost converter applications," in *2013 IEEE Energytech*, 2013, pp. 1–4. DOI: 10.1109/EnergyTech.2013.6645319.

[17] A. Taylor, J. Lu, L. Zhu, K. Bai, M. McAmmond and A. Brown, "Comparison of SiC MOSFET-based and GaN HEMT-based high-efficiency high-power-density 7.2 kW EV battery chargers," *IET Power Electronics*, vol. 11, no. 11, pp. 1849–1857, 2018. DOI: https://doi.org/10.1049/iet-pel.2017.0467.

[18] Navitas Semiconductor. "Gallium nitride: The next generation of power." (2022), [Online]. Available: https://navitassemi.com/gallium-nitride-the-next-generation-of-power/ (visited on 23/02/2023).

[19] S. Dimitrijev, J. Han, D. Haasmann, H. Amini Moghadam and A. Aminbeidokhti, "Power-Switching Applications Beyond Silicon: The Status and Future Prospects of SiC and GaN Devices," in *2014 29th International Conference on Microelectronics Proceedings - MIEL 2014*, vol. 40, May 2014, pp. 43–46, ISBN: 978-1-4799-5296-0. DOI: 10.1109/MIEL.2014.6842083.

[20] D.-K. Jeong, H.-S. Kim, J.-W. Baek, H.-J. Kim and J.-H. Jung, "Autonomous Control Strategy of DC Microgrid for Islanding Mode Using Power Line Communication," *Energies*, vol. 11, no. 4, 2018, ISSN: 1996-1073. DOI: 10.3390/en11040924. [Online]. Available: https://www.mdpi.com/1996-1073/11/4/924.

[21] A. T. Elsayed, A. A. Mohamed and O. A. Mohammed, "DC microgrids and distribution systems: An overview," *Electric Power Systems Research*, vol. 119, pp. 407–417, 2015, ISSN: 0378-7796. DOI: https://doi.org/10.1016/j.epsr.2014.10.017. [Online]. Available: https://www.sciencedirect.com/science/article/pii/S0378779614003885.

[22] Z. W. Khan, H. Minxiao, C. Kai, L. Yang and A. u. Rehman, "State of the Art DC-DC Converter Topologies for the Multi-Terminal DC Grid Applications: A Review," in *2020 IEEE International Conference on Power Electronics, Smart Grid and Renewable Energy (PESGRE2020)*, 2020, pp. 1–7. DOI: 10.1109/PESGRE45664.2020.9070529.

[23] L. Mackay, T. G. Hailu, G. C. Mouli, L. Ramírez-Elizondo, J. Ferreira and P. Bauer, "From DC nano- and microgrids towards the universal DC distribution system - a plea to think further into the future," in *2015 IEEE Power & Energy Society General Meeting*, 2015, pp. 1–5. DOI: 10.1109/PESGM.2015.7286469.

[24] D. Kumar, F. Zare and A. Ghosh, "DC Microgrid Technology: System Architectures, AC Grid Interfaces, Grounding Schemes, Power Quality, Communication Networks, Applications, and Standardization Aspects," *IEEE Access*, vol. 5, pp. 12 230–12 256, 2017. DOI: 10.1109/ACCESS.2017.2705914.

[25] L. Mackay, R. Guarnotta, A. Dimou, G. Morales-España, L. Ramirez-Elizondo and P. Bauer, "Optimal Power Flow for Unbalanced Bipolar DC Distribution Grids," *IEEE Access*, vol. 6, pp. 5199–5207, 2018. DOI: 10.1109/ACCESS.2018.2789522.

[26] GaN Systems. "GaN Systems Plecs Device Models." (2023), [Online]. Available: https://gansystems.com/plecs-device-models/ (visited on 30/01/2023).

[27] S. Bee Law, A. Permal and M. Devarajan, "Effective heat dissipation of high power LEDs mounted on MCPCBs with different thickness of aluminium substrates," in *2012 10th IEEE International Conference on Semiconductor Electronics (ICSE)*, 2012, pp. 707–710. DOI: 10.1109/SMElec.2012.6417241.

[28] F. J. Taylor and A. Williams, *Electronic Filter Design Handbook, Fourth Edition*. McGraw-Hill Education, Jul. 2006, ISBN: 0-07-147171-5.

[29] M. Adamowicz, S. Giziewski, J. Pietryka and Z. Krzeminski, "Performance comparison of SiC Schottky diodes and silicon ultra fast recovery diodes," in *2011 7th International Conference-Workshop Compatibility and Power Electronics (CPE)*, 2011, pp. 144–149. DOI: 10.1109/CPE.2011.5942222.

[30] S. Sapre, "Isolated Gate Drivers — What, Why, and How?" *Analog Dialogue*, vol. 52, Jun. 2018. [Online]. Available: https://www.analog.com/en/analog-dialogue/articles/isolated-gate-drivers-what-why-and-how.html (visited on 12/04/2023).

[31] E. A. Jones, Z. Zhang and F. Wang, "Analysis of the dv/dt transient of enhancement-mode GaN FETs," in *2017 IEEE Applied Power Electronics Conference and Exposition (APEC)*, 2017, pp. 2692–2699. DOI: 10.1109/APEC.2017.7931079.

[32] A. K. Gupta and R. Saxena, "Review on widely-used MPPT techniques for PV applications," in *2016 International Conference on Innovation and Challenges in Cyber Security (ICICCS-INBUSH)*, IEEE, 2016, pp. 270–273. DOI: 10.1109/ICICCS.2016.7542321.

[33] M. Hlaili and M. Hfaiedh, "Comparison of Different MPPT Algorithms with a Proposed One Using a Power Estimator for Grid Connected PV Systems," *International Journal of Photoenergy*, vol. 2016, pp. 1–10, Jan. 2016. DOI: 10.1155/2016/1728398.

[34] A. Ramyar, H. Iman-Eini and S. Farhangi, "Global Maximum Power Point Tracking Method for Photovoltaic Arrays Under Partial Shading Conditions," *IEEE Transactions on Industrial Electronics*, vol. 64, no. 4, pp. 2855–2864, 2017. DOI: 10.1109/TIE.2016.2632679.

[35] *Electrical Characteristics: Power MOSFET Application Notes*, Toshiba Electronic Devices & Storage Corporation, Jan. 2023. [Online]. Available: https://toshiba.semicon-storage.com/eu/semiconductor/design-development/application-note.html.

[36] K. Bernard, "Advantages of Using Gallium Nitride FETs in Satellite Applications," Renesas, Tech. Rep., Feb. 2018. [Online]. Available: https://www.renesas.com/us/en/document/whp/advantages-using-gallium-nitridefets-satellite-applications.

[37] C.-T. Ma and Z.-H. Gu, "Review on Driving Circuits for Wide-Bandgap Semiconductor Switching Devices for Mid- to High-Power Applications," *Micromachines*, vol. 12, p. 65, Jan. 2021. DOI: 10.3390/mi12010065.

[38] S.-J. Chen, S.-P. Yang, C.-M. Huang and S.-L. Syu, "Interleaved Zero-Voltage Switching High Step-Up DC-DC Converter Using a Single Auxiliary Switch," in *2021 IEEE 30th International Symposium on Industrial Electronics (ISIE)*, 2021, pp. 1–6. DOI: 10.1109/ISIE45552.2021.9576421.

[39] J. L. Lu and D. Chen, "Paralleling GaN E-HEMTs in 10kW–100kW systems," in *2017 IEEE Applied Power Electronics Conference and Exposition (APEC)*, 2017, pp. 3049–3056. DOI: 10.1109/APEC.2017.7931131.

[40] T. Pu, U. Younis, H.-C. Chiu, K. Xu, H.-C. Kuo and X. Liu, "Review of Recent Progress on Vertical GaN-Based PN Diodes," *Nanoscale Research Letters*, vol. 16, no. 101, 2021. DOI: 10.1186/s11671-021-03554-7.

Appendices

Appendix A

Supplementary Converter Pictures

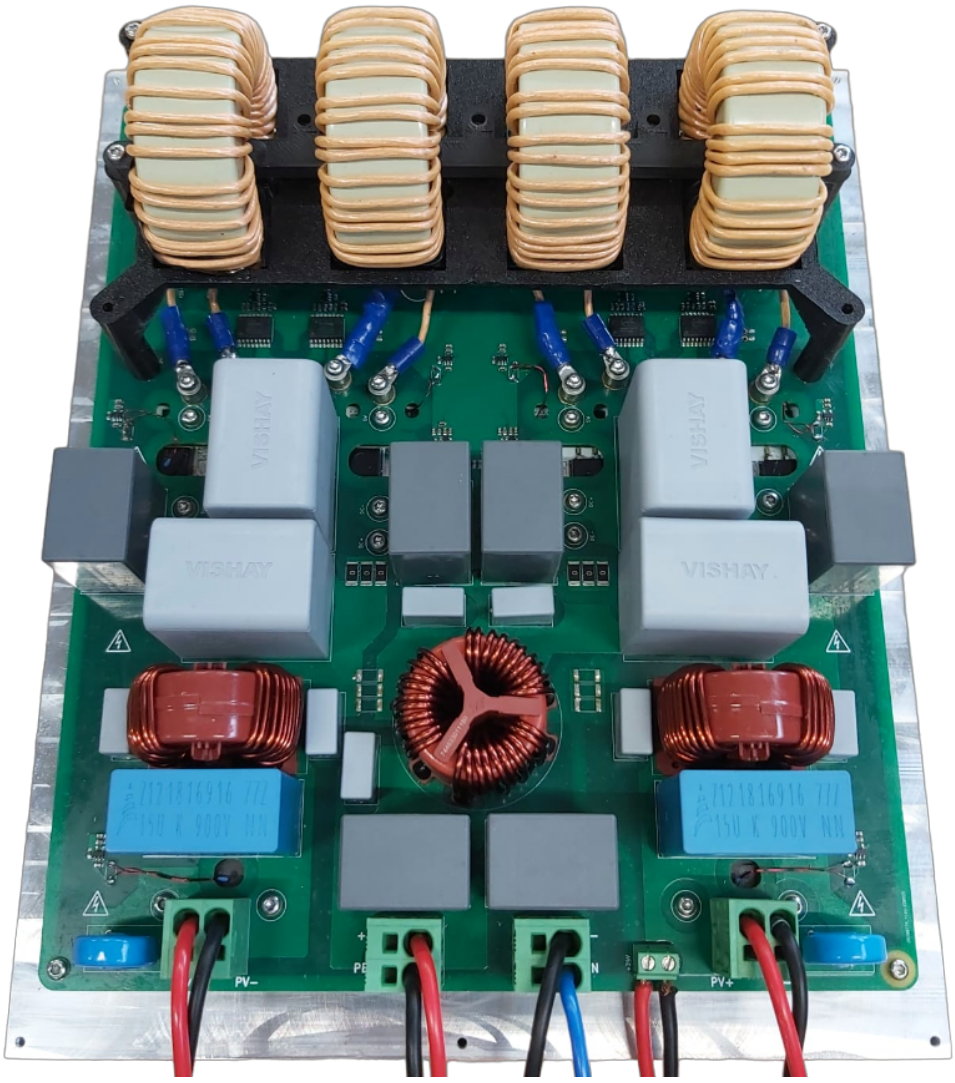

Figure A.1: Top view of the MPPT converter.

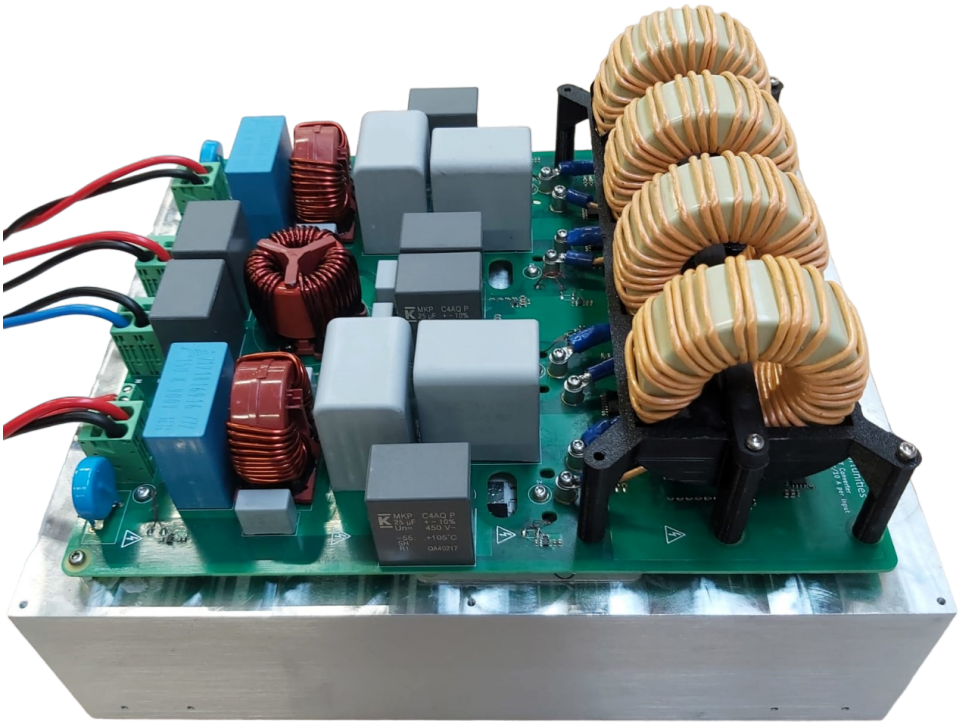

Figure A.2: Side view of the MPPT converter.

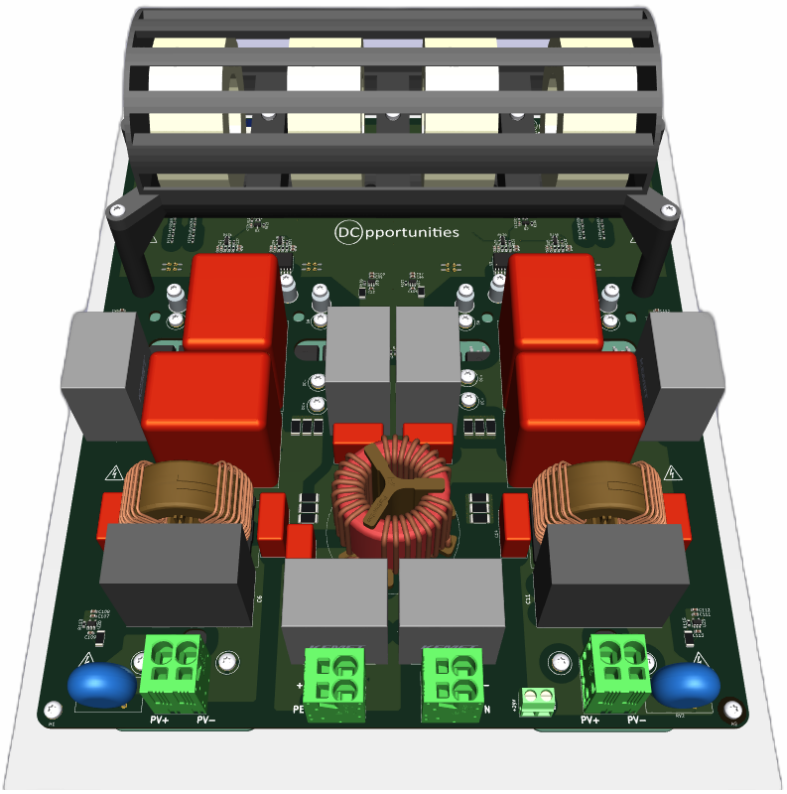

Figure A.3: Main board 3D model designed in KiCad.

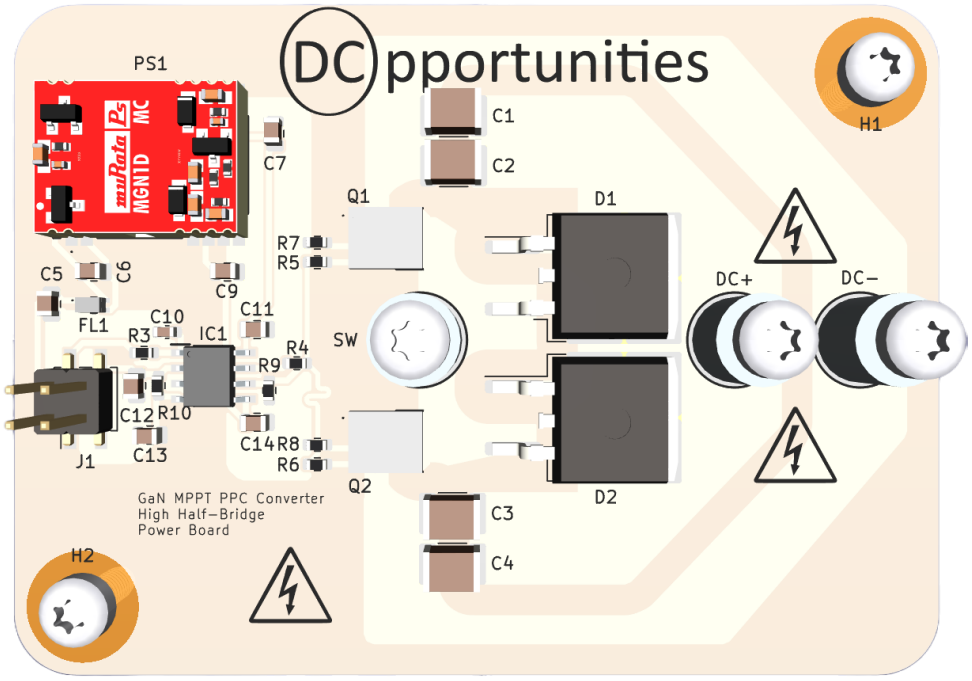

Figure A.4: Single-layer aluminium high half-bridge board 3D model designed in KiCad.

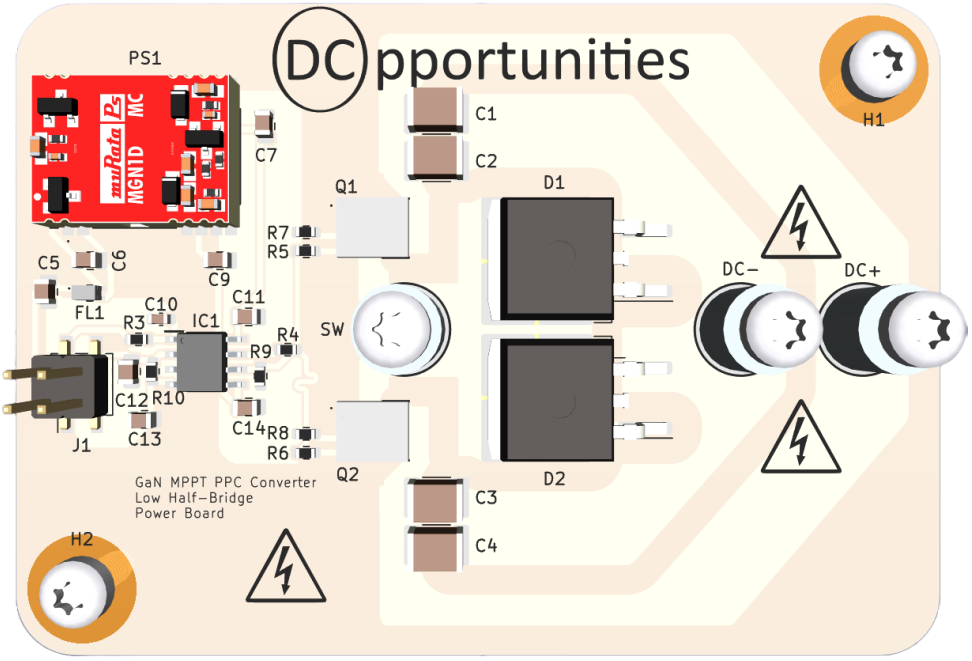

Figure A.5: Single-layer aluminium low half-bridge board 3D model designed in KiCad.